

Assessment of Tork

CALIFORNIA INSTITUTE OF TECHNOLOGY

MECHANICAL ENGINEERING LABORATORY

PX. 3

THEORETICAL AND EXPERIMENTAL INVESTIGATIONS


OF AXIAL FLOW COMPRESSORS

PART 3

Progress Report on Loss Measurements
In Vortex Blading

A REPORT ON RESEARCH CONDUCTED UNDER
CONTRACT WITH THE OFFICE OF NAVAL RESEARCH

July 1951



THEORETICAL AND EXPERIMENTAL INVESTIGATIONS OF AXIAL FLOW COMPRESSORS

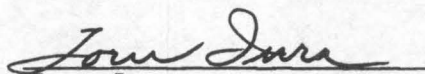
Under Navy Contract N6 - ORI - 102 Task Order IV

PART 3

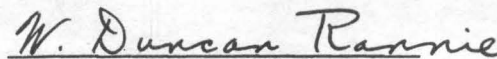
Progress Report on Loss Measurements
In Vortex Blading

Prepared by:


Charles C. Alsworth


Toru Iura

Approved by:


W. Duncan Rannie

Mechanical Engineering Laboratory
California Institute of Technology
Pasadena, California, July, 1951

ACKNOWLEDGEMENT

The authors wish to acknowledge the untiring cooperation and efforts of the project staff, Mr. T. Linton and Mr. T. Taniguchi. They also express their sincere appreciation to Dr. R. H. Sabersky for his many helpful suggestions and advice.

SUMMARY

This report gives the results of extensive and detailed measurements of the flow pattern in a single stage axial flow compressor with free vortex blading. Considerable information is given on the location and magnitude of losses through the various blade rows. Some of the measurements are repetitions of those given in an earlier report, but the new data is more detailed and presumably more accurate.

Preliminary results are presented on the investigation of the radial distribution of work input by measuring the rise of stagnation temperature along a stream line.

CONTENTS

- I Introduction
- II Test Compressor and Instrumentation
- III Flow Through "Free Vortex" Blading
 - 3:1 Pre-Rotation Vanes
 - 3:2 Rotor
 - 3:3 Stator
- IV Temperature Measurements

ILLUSTRATIONS

<u>FIGURE NO.</u>	<u>TITLE</u>
1	Photograph of Test Installation
2	Compressor - Single Stage Blading
3	Photograph of Total Head Rake
4	Photograph of Speed Controller Panel
5	Pressure Pickup Circuit
6	Statham Gage Calibration Curve
7a	Speed Control Circuit
7b	Speed Control - Relay Circuit
8	Photograph of Potentiometer Panel
9	Photograph of Galvanometer Suspension
10	Potentiometer Circuit Diagram
11	Total Temperature Probe
12	Calibration Nozzle
13	Leaving Angle for Pre-rotation Vanes
14	Average Axial Velocity Behind Pre-rotation Vanes
15	Comparison of Measured and Calculated Axial Velocities Behind Pre-Rotation Vanes
16	Average Total Pressure Behind Pre-rotation Vanes
17	Losses through Pre-rotation Vanes
18	Rotor Leaving Angle
19	Average Axial Velocity through Rotor
20	Comparison of Measured and Calculated Axial Velocity behing Rotor
21	Torque Curve for Expanded Single Stage Compressor

FIGURE NO.TITLE

- 22 Total Pressure Rise through Rotor, $\Delta p_t / \frac{1}{2} \rho w_1^2$
- 23 Change in Angular Momentum through Rotor
(based on entering velocity relative to rotor)
- 24a Total Pressure Rise through Rotor, $\Delta p_t / \frac{1}{2} \rho u_0^2$
- 24b Change in Angular Momentum through Rotor
- 25 Rotor Loss Coefficient
- 26 Comparison of Rotor Loss at Midsection with Two
Dimensional Cascade
- 27 Rotor Loss Curve, $\bar{\Phi}_0 = 0.370$
- 28 Rotor Loss Curve, $\bar{\Phi}_0 = 0.400$
- 29 Rotor Loss Curve, $\bar{\Phi}_0 = 0.430$
- 30 Rotor Loss Curve, $\bar{\Phi}_0 = 0.460$
- 31 Rotor Loss Curve, $\bar{\Phi}_0 = 0.490$
- 32a Boundary Layer Data Behind Rotor - Displacement and
Momentum Thickness
- 32b Boundary Layer Data Behind Rotor - Shape Parameter
- 33a Boundary Layer Data Behind Stator - Displacement and
Momentum Thickness
- 33b Boundary Layer Data Behind Stator - Shape Parameter
- 34 Comparison of Stator Loss at Mid-section with Two
Dimensional Cascade
- 35 Stator Loss Coefficient
- 36 Stator Total Pressure Loss Coefficient
- 37 Stator Loss Curve, $\bar{\Phi}_0 = 0.370$
- 38 Stator Loss Curve, $\bar{\Phi}_0 = 0.400$

<u>FIGURE NO.</u>	<u>TITLE</u>
39	Stator Loss Curve, $\bar{\Phi}_0 = 0.430$
40	Stator Loss Curve, $\bar{\Phi}_0 = 0.460$
41	Stator Loss Curve, $\bar{\Phi}_0 = 0.490$
42	Incidence Angles to Stator
43	Stator Leaving Angles vs Radius
44	Stator Leaving Angles vs Incidence Angles
45	Air Turning Angle Through Stator
46	Axial Velocity Behind Stator
47	Comparison of Measured and Calculated Axial Velocity Behind Stator
48	Average Total Pressure Behind Stator
49	Overall Performance Curves
50	Average Total Pressure (at each section)
51	Recovery Factor of Total Temperature Probe
52	Rotor Work Input
53	Total Pressure Contours Downstream of Entrance Vanes
54	Total Pressure Contours Downstream of Rotor
55	Total Pressure Contours Downstream of Stator

I. INTRODUCTION

This report is the third on the research on axial flow compressors, conducted under Navy Contract N6-ORI-102, Task Order IV. In the first report a simplified perfect fluid theory for the design of axial flow compressors was presented, the test equipment for the experimental program was described, and some preliminary test results were given. In the second report test results for two different blade sets were presented. The overall performance agreed well with that predicted by the theory and even the detailed flow pattern was in excellent agreement with the computed one, except of course near the boundaries where viscosity effects are important. These experimental results were, therefore, taken as proof of the validity of the proposed theory. The above tests concluded the first phase of the research program, the phase during which attention was concentrated on the main body of the flow which was little influenced by the effects of viscosity. The second phase of research was then initiated during which attention is to be focused on the effects of viscosity, in particular on friction losses and on the deviations of the velocity and pressure profiles from those predicted by the perfect fluid theory. Some preliminary experiments on friction losses were presented in the second report.

The experimental work on the effects of viscosity was continued in the period described in the present report.

Since the deviations from the perfect fluid flow pattern as well as the losses are extremely small, very complete and accurate measurements are necessary for this investigation. To obtain the required accuracy and to improve the rate at which measurements can be taken, certain changes in the instrumentation were made. The time required for a complete survey of one stage is of course still long because of the large number (about 6000) of individual measurements needed. The first set of data is now complete and a detailed discussion of these measurements as well as of the instrumentation is given in the following sections.

II. TEST COMPRESSOR AND INSTRUMENTATION

2.1. Description of Compressor Arrangement

The compressor used for the present series of tests is the same one described in Ref. 1. The arrangement has been modified slightly, however, by reversing the rotor hub so that different axial spacing of blades could be obtained. The pre-rotation vanes were located in the blade holes provided for the first stator and the stator blades were located in the holes provided for the third stator, the rotor being midway between the two. The manner in which the setup differs from the normal arrangement is illustrated in Fig. 2. With this arrangement it was possible to make detailed surveys behind each set of blades, with all blade rows in place. With the use of the total head rake described below in Section 2 and 3, it was also possible to make total head surveys in front of the pre-rotation vanes. In this manner the location and nature of the losses in a single stage compressor could be determined completely and accurately.

Several items of new equipment have been added and are described in the following paragraphs. These include the thermocouple total temperature probes and the potentiometer and galvanometer necessary to measure changes in the stream total temperature. This technique is described in section IV of this report.

2.2 Experimental Procedure

To obtain the data described in this report, detailed surveys of flow direction, total pressure, and dynamic pressure were made behind each set of blades. As stated above, total pressure surveys were made in front of the pre-rotation vanes as well. All directional surveys were made with the claw type probe described in paragraph 3:3(h), Reference 1. For most purposes this type of yaw probe has been found to be more sensitive and more accurate than the cylindrical type of yaw probe previously used. To obtain data required for orientation of the total head and pitot-static probes, directional surveys were made at all points where it was anticipated that total pressure and velocity pressure readings would be required. This entailed surveys at seventeen radii and a minimum of fifteen survey points at each radius. Behind the pre-rotation vanes and the stator blades, where strong wakes exist, the number of survey points at each radius was between twenty and twenty five, depending on the size of the wake. At all radii except the two nearest the hub and case both total pressure and velocity pressure surveys were made with the pitot-static probe described in paragraph 3:3(f), Reference 1. At the two radii nearest the walls, one near the hub and one near the outer case, the special total head probes described in paragraph 3:3(i) and illustrated in figure 31, Reference 1, were used.

After the surveys were made, the average total head, flow coefficient, and angular momentum of the air were computed for each radius, and these were then integrated over the annulus. In the case of the pre-rotation vanes and the stator, the difference of total head from in front to behind the row was taken as the loss in the blade row. In the case of the rotor, the difference between the increase of angular momentum and the increase of total head through the row was taken as the loss. The work input obtained from measurements of increase of total temperature over the rotor is compared with that obtained from the increase of angular momentum.

2:3 Total Head Rake

For detailed surveys downstream of each blade row, it was possible to probe a representative section of the compressor annulus by means of a traversing instrument carriage set in a survey port. However, no provisions were made for such a port in front of the entrance vanes. Hence, it was necessary to conduct an annular survey by means of a total head rake that covered the desired area.

Figure 3 shows a picture of the total head rake that was constructed for this purpose. It consists of 34 pressure tubes which are accurately located and held together by a

support tube. Each pressure tube is made of 0.020" I.D. stainless steel hypodermic tubing. The support tube is secured to the compressor through a radial blade hole. By moving the support tube in a radial direction, it was possible to obtain total head readings throughout a representative section of the compressor annulus.

The rake was made by the Astro-Physics machine shop on the California Institute campus.

2:4 Pressure Pickup System

The pressure detecting system used heretofore consisted of a Wheatstone Bridge galvanometer arrangement which was used to detect changes in the resistance of the Statham strain gage pickup. This arrangement was quite satisfactory for yaw angle surveys, but it proved to have many disadvantages for determining total head or velocity head. Considerable time was consumed in obtaining a pressure reading because this involved balancing the galvanometer by means of the helipot potentiometer. This necessitated an approximate knowledge of the pressure in advance in order to reduce the galvanometer deflection. Furthermore, continuous watching of the galvanometer resulted in considerable eye strain.

In order to obtain a more rapid and direct method of recording pressure data and also to minimize operating fatigue, the pressure pickup circuit described in Ref. 1 was modified

by installing a Brown "Electronik" precision indicator in the bridge circuit. This was done by replacing the galvanometer with the Brown amplifier system and the helipot potentiometer with the Brown slide wire. Fig. 5 shows the modified pressure pickup circuit. The Brown indicator was manufactured by the Brown Instrument Co., Philadelphia, Pa.

Since the Brown indicator is a continuous balance system, it was possible to obtain rapid and direct reading without the necessity of manual balance. Further the large illuminated dial on the instrument made it considerably easier to read the data.

The new arrangement has ranges from 1/2" to 5" of water, and the pressure may be read to 0.001" of water in the 1/2" range. Typical calibration curves are shown in Fig. 6.

2:5 Speed Controller

One of the time consuming factors in making a survey run in the compressor is the maintenance of a constant rotational speed during any recording interval. During a run, the speed was found to vary in a random manner due to changes in the line voltage, heating of a motor component, or other causes. It was observed that a deviation of about 2 rpm at a rotational speed of 1100 rpm caused the entrance duct wall pressure to vary slightly over 0.001 in. of water. This is equivalent to a change of about 0.25 percent in the flow rate at design conditions.

In order to reset the speed, it was necessary to adjust either the dynamometer armature voltage or field current, and this required careful manipulation of the rheostats to obtain a speed to within one rpm of the desired value. The manual readjustment and the consequent checking of the speed with the revolution counter, consumed much time during each survey.

A speed controller has been installed in the hope of eliminating this time factor and assuring a constant speed during a survey run. This is a model D.C.T. 2 direct current potentiometer type speed controller designed and manufactured by the Thiele-Wright Co. of Los Angeles, Calif. Circuit diagrams of the speed controller are shown in Figs. 7a and 7b. Fig. 4 shows a photograph of the speed controller operating panel.

Briefly, the operation of the potentiometer speed controller is as follows. A General Electric D.C. tachometer generator is driven from the compressor shaft by means of a chain drive. Any variation in the compressor rotational speed causes a corresponding change in the tachometer generator output. Since the potentiometer has an upper range of 11.11 volts, the General Radio 510-E decade resistance divides the generator voltage output so that less than 11 volts are fed into the potentiometer circuit. A ten-step tap switch in series with the decade (R_1) regulates the sensitivity of the speed con-

troller. A three-way switch (S_3) brings the standard cell into the circuit to oppose the potentiometer current going through the Weston galvanometer. The decades (R_2) in the potentiometer current have a constant resistance and the dial settings merely shift the resistances above or below the potentiometer leg. These decade resistances determine the desired speed settings of the instrument. The 200 ohm helipot resistance (R_3) adjusts the potentiometer current to balance that of the standard cell. When the system is set for a certain speed, the entire circuit is in balance. Any change in speed will cause a change in the tachometer generator output. This throws the system out of balance and causes the 2420C galvanometer to deflect. The deflected light beam of the galvanometer strikes one or the other of the two photocells placed at its end-deflection points and triggers a relay circuit. The relay circuit actuates a motor which in turn drives the dynamometer field rheostat regulating the speed. Once the speed has been adjusted, the potentiometer is in balance again. Three pilot lights are installed on the speed controller operation panel. One, R in Fig. 7b, indicates that the power supply is on. The other two, A & W in Fig. 7b, are in the rheostat motor relay circuit and indicate the direction of the speed change.

Specifications called for a regulation of ± 2 rpm at 1100 rpm; however, the circuit is designed to give a regulation

of $\pm 1/2$ rpm at the maximum sensitivity.

2:6 Potentiometer

The potentiometer used for measuring thermocouple emf's is shown in Figure 8 and the circuit is shown in Figure 10. The circuit was designed by Mr. John Harris of the Calibration Laboratory operated by the Physics and Electrical Engineering Departments of the California Institute of Technology, and the instrument was constructed on the campus. It utilizes a Weston Model 280 milliammeter to measure the flow of current through a calibrated resistance. This resistance has taps to give 0.05, 0.1, or 0.2 ohms resistance; thus, the full scale deflection of the milliammeter (1 milliampere) is 50, 100, or 200 microvolts, respectively, for the three ranges. A D'Arsonval galvanometer made by Leeds and Northrup is used to indicate a null. In order to eliminate as completely as possible spurious voltages and changes in resistance of the circuit, gold contact keys were used in the galvanometer circuit both for closing the thermocouple circuit and the damping resistance circuit. In addition, a silver contact switch was used in the milliammeter circuit.

2:7 Galvanometer Suspension

Because the galvanometer was to be used in the laboratory in conjunction with running machinery, it had to be isolated by the construction of a special suspension as shown in Figure 9.

This suspension is essentially that described on page 328, Reference 5. Certain modifications were made, however. A four point rather than a three point suspension is used, and the pans of oil for damping are on shelves suspended below the galvanometer. One pan contains mercury in order to give the suspension the proper period. The entire galvanometer and suspension is enclosed in a cabinet to protect it from air currents stirred up by the compressor. This arrangement has performed very satisfactorily.

2:8 Thermocouple Probes

The probes used for measuring total temperature thus far are half-shielded, cylindrical probes developed at the Pratt and Whitney Aircraft Experimental Test Laboratory at East Hartford, Connecticut, and manufactured by the Whitney Instrument Company at East Longmeadow, Massachusetts. The probes are described in Reference 4.

These probes are extremely convenient, since, because of the cylindrical construction, they can be inserted or removed from the compressor with ease. Further comment on the performance of these probes is made in another section of this report.

III. FLOW THROUGH FREE VORTEX BLADING

3:1 Pre-rotation Vanes

The pre-rotation vanes for the "free vortex" blading are described in Ref. 1. They were designed to produce a simple vortex for the distribution of whirl component of velocity. The entering velocity is always axial and fairly uniform, although the struts of the front bearing support produce slight wakes. With a vortex whirl distribution the axial velocity component behind the vanes should be uniform over the annulus. Detailed surveys of the flow distribution in front of and behind the vanes were made to determine leaving angle and losses.

The leaving angle for the pre-rotation vanes as measured with small yaw probes is shown in Fig. 13. The angles check the design values quite well except near the inner and outer walls of the duct. The large local deviations result from the wake behind the blade and since the yaw probe may not read correctly in a velocity gradient, the angles measured in the wake may not be true angles. In the regions of the inner and outer walls, the boundary layer at the wall combines with the boundary layers of the blades to produce a strong wake and probably secondary flow.

The axial velocity component behind the pre-rotation vanes was deduced from measurements of the velocity and the

angle of flow. The average values of the axial velocity component are plotted against radial position in Figs. 14 and 15. Except at the walls, where the boundary layers reduce the flow rate, the axial velocity is uniform and close to design. In Fig. 15 the axial velocity computed from the measured leaving angles is plotted for comparison with the measurements. The lack of agreement at the walls is not surprising; the calculations are based on the perfect fluid theory as described in Ref. 1 and the real fluid effects (viscosity and turbulence) must have strong influence in the regions of high shear close to the walls. In addition, secondary flow exists in the blade passages near the walls. Although this secondary flow is a perfect, rather than real fluid effect, it is so closely involved with the wall layer growth that attempts to separate it by measurement and analysis were not very successful.

The average total pressure behind the pre-rotation vanes is plotted in Fig. 16. The zero ordinate refers to atmospheric pressure, so the points plotted give the total loss through the entrance duct and pre-rotation vanes. The screen on the front of the entrance duct contributes a fair amount to the losses. The total pressure is quite uniform over most of the compressor annulus and 50% or so of the losses are concentrated near the walls. In Fig. 17 the losses through the pre-rotation vanes alone are plotted. These losses are quite small except near the blade extremities; this is to be expected because the

vanes resemble turbine blades and have a favorable pressure gradient. The dashed lines near the wall regions do not represent actual physical conditions. The boundary layer growth along the wall and through the blade row makes it almost impossible to follow a stream line through the blade row. Further, mixing processes occur in the regions of high shear and confuse the results.

3:2 Rotor

The measurements on the flow through the rotor of the free vortex blading are repetitions of those reported in Ref. 1. These new measurements are more accurate and detailed than given previously. The compressor was rearranged so the blade rows could be separated for more convenient access in front of and behind the rotor.

The leaving angles from the rotor, as measured with yaw probes, are shown in Fig. 18. The incidence angle is calculated from the flow measurements behind the pre-rotation vanes. Originally the blades were designed from the rule of Constant (see Ref. 1) but measurement showed that the design angles were not quite attained. Hence the blades were turned to produce the design leaving angles over the middle part of the channel. As can be seen from Fig. 18 the leaving angles are relatively independent of incidence angle, even near the blade tips where the solidity is low. Near the roots, the relatively strong real fluid effects are probably quite important in determining the leaving angles. At the higher incidence angles,

part of the rotor is stalled but even this does not cause a very large deviation of the exit angle. Neither the rule of Constant nor the thin airfoil cascade theory is quite satisfactory for the prediction of leaving angle, although the deviations are not very large.

The axial component of velocity leaving the rotor should be uniform at the design flow rate for "free vortex" blades. The measured distributions for five flow rates are shown in Fig. 19. The design flow rate is $\phi = C_a/u_o = 0.45$ and it can be seen from the figure that at this flow rate the axial velocity is about uniform except near the walls where the boundary layer influence predominates. The three-dimensional character of the flow at off-design flow rates is indicated by the slope of the ϕ curves. With the measured exit angles, the axial velocity distribution was calculated by the theory described in Ref. 1 and the comparison with the measurements is made in Fig. 20. Again the agreement is poor at the walls, particularly at the inner radius where the real fluid effects are strong, but the theory appears quite satisfactory outside the wall regions.

Measurements of the torque as a function of flow rate are shown in dimensionless form in Fig. 21. From the detailed surveys, the angular momentum in front of and behind the rotor row was calculated and weighted with respect to the axial velocity. The difference, when integrated over the annulus, should be identical with the torque since both correspond

to work done by the rotor on the air. As can be seen from Fig. 21, the agreement is excellent. This comparison is an indirect way of determining the accuracy of the measurements.

Measurements of total pressure difference across the rotor row are given in Fig. 22. These are plotted against incidence angles for various radii, because this seems to be the most significant parameter. If there were no losses, the rise in total pressure through the rotor would be equal to the total pressure calculated from the momentum change. The latter was measured and is plotted in Fig. 23. These two quantities are also plotted in Figs. 24a and 24b as functions of radius. The difference between these two represents the losses, and these are plotted in Fig. 25. The differences are small and hence there is more scatter in evidence. The loss in total pressure as measured near the blade ends represents more than profile losses because the mixing processes near the wall and the secondary flow are important, but difficult to separate from the mean flow conditions. The losses rise sharply at the higher incidence angles, corresponding to the "stall".

A comparison is made in Fig. 26 between the rotor losses and the measurements made on a two-dimensional cascade (Ref. 3) with somewhat similar blade profile. The losses in the two cases are not much different at moderate incidence angles but the compressor blade section stalls at a lower angle than the cascade section. The reason for this is not known; the Reynolds

numbers are not too different. The earlier stalling of blades in a compressor as compared with cascades seems to be characteristic, and is, of course, very important for design. It may be a result of some form of "contamination" from neighboring blade sections of different shape and flow conditions, whereas in the cascade the blade sections are the same along the blade length.

The rotor blade losses are cross-plotted in Figs. 27 to 31 against radius. The losses at the blade ends are shown with dashed lines because their physical significance is not apparent, again a result of boundary layer flow. The boundary layer thicknesses behind the rotor are shown in Figs. 32a and b. The displacement and momentum thicknesses at the inner and outer walls are shown as functions of flow rate, as well as the shape parameter $H = \delta^*/\theta$. The reason for the waviness of the thickness lines is not known; under any circumstances it is not large and as a first approximation one can say that the thicknesses are little affected by flow rate. The shape parameter H is smaller than for pipe flow or flow in a turbulent boundary layer along a flat plate.

The conclusions that can be drawn from the measurements on the flow through the rotor are

- (a) The perfect fluid theory of flow through the rotor as given in Ref. 1 is adequate for determining the overall flow patterns within the middle 80% to 90% of the blade length. The leaving angles, even in

the stalled region, are given fairly adequately by thin airfoil theory or a simple empirical rule.

- (b) The profile losses through the blade row are approximately the same as for a two-dimensional cascade for moderate incidence angles. The compressor cascade, however, stalls at a lower incidence angle than a two-dimensional cascade.

3:3 Stator

The detailed survey behind the stator blade row likewise is a repetition of that reported in Ref. 1. As in the case of the rotor, these new measurements are more accurate and detailed than given previously.

The boundary layer thicknesses behind the stator are shown in Figs. 33a and b. The displacement and momentum thicknesses at the inner and outer walls are shown as a function of flow rate, as well as the shape parameter $H = \delta^*/\theta$. At the outer wall, there is little variation in the thicknesses and shape parameter with flow rate; however, these quantities show a decided increase at the inner wall with the lower flow rates corresponding to the "stalled" region.

The total pressure losses were measured by taking the difference of pressure in front of and behind the blade row. The results for the mid-section averaged over circumferential

angle are plotted in Fig. 34. They are more plausible than the earlier results (see Fig. 67 of Ref. 2). The difference is a result of more extreme care in the measurements. The losses for this blade section are about the same magnitude whether the stator is isolated without a rotor in front of it, or following a rotor. The losses calculated from boundary layer theory, as given in Ref. 2, agree with the isolated stator losses except at the incidence angles where the flow is separated. The stator losses for the expanded single stage setup does not show the stall occurring at such a low incidence angle as was the case for the rotor.

Losses measured on a two-dimensional cascade of somewhat similar blade section (Ref. 3) are shown for comparison. The losses in the compressor are definitely larger, but not to the extent stated in the earlier report. The unstalled region for the actual compressor is much smaller than that of the cascade and stalling does occur slightly earlier. This earlier stalling is much more pronounced at other sections. One of the most important tasks will be to discover the reason for this earlier stalling and to find ways of predicting it for a compressor installation.

In Figs. 35 and 36, the stator loss coefficient and the total pressure loss coefficient are plotted as a function

of incidence angles for various radii. As with the rotor, the losses near the blade ends are greater than that accountable by profile losses because of real fluid effects near the wall. Also the losses rise sharply at the higher incidence angles corresponding to the "stalled" region. The slight inconsistency of the midsection stator loss coefficients given in Figs. 34 and 35 are due to the fact that the values given in Fig. 34 are "faired" values taken from the stator blade losses crossplotted against radius (Figs. 37 to 41).

The stator loss curves are given in Figs. 37 to 41. The overall loss represented by the area under these curves is greatest at the lowest flow rate. Furthermore, at this flow rate, the losses rise sharply at the inner radius due to increased boundary layer effects.

Fig. 42 shows the incidence angles, and Fig. 43 shows the stator leaving angles plotted as a function of radius for various flow rates. From these two curves, it can be seen that the leaving angles are relatively independent of the incidence angles for the design flow rates and above, but marked deviation is apparent for the lower flow rates and in the region near the inner radius. This again is due to the real fluid effects in these regions.

Fig. 44 shows the leaving angles compared with thin

airfoil cascade theory and Constant's rule. At the mid-section, the measured angle falls between the values calculated according to the two methods. At $R/R_0 = 0.9$, the agreement between the measured value and thin airfoil cascade transformation value is very close. Toward the inner radius at design incidence (i.e., $i^* = 0^\circ$), the trend seems to be toward closer agreement between the measured value and that obtained from Constant's rule.

Fig. 45 shows the air turning angle through the stator plotted as a function of radius for various flow rates. The lowest flow rate ("stalled" region) shows a great decrease in turning angle in the inner region of the compressor due to the greater boundary layer effects there.

The axial velocity curves in Fig. 46 show the three-dimensional character of the flow at off-design flow rates. Also, the influence of the larger boundary layer near the inner radius at the lower flow rates can be seen from these curves.

With measured entrance conditions and exit angles, the axial velocity distribution was calculated by the theory presented in Ref. 1, and the comparisons with the measurements is made in Fig. 47. Again, the agreement is poor at the walls, and for the lowest flow rate this is also true away from the walls.

Fig. 48 shows the average total pressure behind the stator; again, the real fluid effects near the inner wall and for the "stalled" region are evident.

An overall performance picture of the expanded single stage compressor is given in Fig. 49. Maximum efficiency of 90 percent is achieved below the design flow rate at $\bar{\Phi}_0 = 0.400$.

Figs. 53, 54, and 55 show a contour plot of total pressure behind the entrance vane, rotor, and stator respectively. Figs. 54 and 55 are similar to Figs. 60a and b of Ref. 1 except that the new plots are made from more detailed survey data. The contours represent lines of constant specific energy in terms of the local pressure coefficient

$\psi' = \frac{P_t - P_a}{\frac{1}{2} \rho u_0^2}$. The regions of large energy defect occur

near the outer and inner boundary (the wall boundary regions), and also directly downstream of an entrance vane or stator blade trailing edge (blade wake). Only the wall boundary regions are detected behind a rotor blade because there the total head measured in a stationary reference system represents an average value. Fig. 55 shows results similar to that given by the total head loss contours in Fig. 124 of Ref. 6, in which the losses away from the walls are accounted for by secondary flow.

IV INVESTIGATIONS OF THE RADIAL DISTRIBUTION OF WORK INPUT

The efficiency of a compressor is usually determined from measurements of the shaft torque input and of the pressure increase and flow rate. If local efficiencies of the blade section are desired, the section work input must be measured as well as the local pressure rise and flow rate. Two methods are available for measuring the work input along a stream line through a rotor blade row. One of these methods consists of measuring the rate of change of angular momentum of the fluid passing through the rotor along a stream line. In principle this is not difficult. If there is no appreciable shift of stream line radius, the work coefficient is given by

$$\psi = 2 \bar{r} (\lambda_2 - \lambda_1)$$

where \bar{r} is the dimensionless radius and λ_1 and λ_2 are the dimensionless whirl components of velocity in front of and behind the rotor respectively. The whirl velocities are averaged over the circumferential direction and their determination involves a detailed survey, particularly if strong wakes from a preceding stator blade row are present. Hence accurate measurement of the local work input by this method is tedious. Another drawback is that the measurements can be made only if no stator blade row intervenes between the measuring stations; it is not possible to determine the work input along a stream line through more than one rotor blade row.

The second method for determining the local work input is

by measuring the rise of stagnation temperature along the stream line. Accurate measurement of temperature in a stream is difficult but in spite of this the method has definite advantages. The influence of wakes is relatively small and hence circumferential surveys can usually be avoided; further, the work done on any stream line filament can be measured irrespective of the presence of stator blades, provided only that the transport of heat to neighboring stream lines is negligible. The method has been used previously chiefly for determining the average work input in multistage compressors but as far as is known it has not been employed for measurement of the radial distribution of work input for a single rotor row. An elaborate apparatus with a resistance thermometer was designed in Germany for this purpose (Reference 7) but there is no evidence that it was put in operation or even completed. On this project considerable time and effort has been devoted to the development of a satisfactory method for measuring temperature distribution because it appears to be quite important. At the time of writing, a method has been tested and appears satisfactory, although only a limited amount of routine data has been taken.

4:2 The Work Input

The energy equation for a stream tube passing through a rotating blade row, is if radial velocity components are neglected,

$$c_p T_1 + \frac{1}{2} (C_{a_1}^2 + C_{u_1}^2 - 2\omega r C_{u_1}) = c_p T_2 + \frac{1}{2} (C_{a_2}^2 + C_{u_2}^2 - 2\omega r C_{u_2})$$

or, rearranging

$$\omega r C_{u_2} - \omega r C_{u_1} = C_p T_2 + \frac{1}{2} (C_{a_2}^2 + C_{u_2}^2) - C_p T_1 - \frac{1}{2} (C_{a_1}^2 + C_{u_1}^2) \quad (1)$$

The left hand side is proportional to the rate of change of angular momentum of the air and is equal to the work done per unit mass on the air. The quantity $T + \frac{1}{2} (C_a^2 + C_u^2) / C_p = T_t$ is the total temperature of the fluid, i.e., the temperature at a stagnation point. Hence the work done on the air per unit mass by the rotor is

$$\omega (r C_{u_2} - r C_{u_1}) = C_p \Delta T_t$$

A dimensionless work coefficient ψ can be defined by dividing through by $u_0^2/2$, i.e.,

$$\psi = \frac{\omega r (C_{u_2} - C_{u_1})}{\frac{1}{2} u_0^2} = 2 \xi (\lambda_2 - \lambda_1) = \frac{2 C_p \Delta T_t}{u_0^2} \quad (2)$$

In the equations above the specific heat is expressed in units of $(ft)^2 / (sec^2 \text{ } ^\circ F)$ obtained by multiplying the usual units by g.

4:3. Determination of the Stream Total Temperature

As can be seen from the foregoing discussion the direct determination of the work input to a stream is dependent on the determination of the total temperature rise in the stream. While simple in theory, this is difficult in practice because temperature indicating devices do not indicate the true total temperature of the stream. Rather, the temperature indicated by a temperature probe is

$$T + k \frac{v^2}{2C_p}$$

where the quantity k is the recovery factor of the probe and is a function of the velocity and possibly of other parameters. The major problem, then, in the measurement of the stream total temperature is the determination of the recovery factor of the probe under the conditions under which it is to be used.

If two probes, identical in construction so that they should have the same recovery factor, are placed at points in a stream at which the velocities are different, the temperature difference indicated by the probes, if no work is done on the fluid and there is no heat transfer to or from the stream between the points, is

$$\Delta T = T_2 + k_2 \frac{v_2^2}{2C_p} - T_1 - k_1 \frac{v_1^2}{2C_p}$$

Or, if the total temperature is substituted for the static temperature,

$$\Delta T = T_{t_2} - \frac{v_2^2}{2C_p} + k_2 \frac{v_2^2}{2C_p} - T_{t_1} + \frac{v_1^2}{2C_p} - k_1 \frac{v_1^2}{2C_p}$$

If no work is done on the fluid and there is no heat transfer between points 1 and 2, the total temperature does not change and the temperature difference indicated is then

$$\Delta T = (k_2 - 1) \frac{v_2^2}{2C_p} - (k_1 - 1) \frac{v_1^2}{2C_p}$$

This relation indicates the method of determining the recovery factor. Two identical probes are inserted into an air stream at points of different velocity and the indicated temperature difference determined. If air from a large reservoir is expanded through an adiabatic nozzle, v_1 can be taken to be zero, and the temperature difference is

$$\Delta T = (1 - k_2) \frac{v_2^2}{2C_p}$$

Rather than use a large reservoir, a nozzle of one inch diameter on the end of an eight-inch tube provided with straightening vanes, as shown in Figure 12, was used. This nozzle was supplied with a steady flow of air by a blower. Actually, apparently insurmountable difficulties have been encountered and the method has been abandoned; temporarily, at least. Even though the tube and nozzle were surrounded with about two inches of rock wool insulation, it was impossible to eliminate temperature gradients within the tube and in the jet. No consistent values for the recovery factor have been obtained in this manner. Surveys made with a bare thermocouple in the area of the jet in which the velocity profile is flat, indicate a fairly flat temperature profile also. However, when experiments are performed in which the depth to which the probe is immersed in the stream is varied, the profile of the indicated temperature is not flat, nor does the maximum occur at the center of the jet (the position of the thermocouple junction), but near the point of maximum immersion, i.e., when the tip of the probe is still just barely within the jet. This indicates that the depth of immersion of the probe in the stream in which the temperature is to be measured is significant. No analysis of this significance has been made but it is planned to perform simple experiments with several types of probes.

Another method that is available is as follows: if a relation between the recovery factor and the velocity is assumed, e.g.,

$$1 - k = a_0 + \frac{a_1}{v} + \frac{a_2}{v^2} + \dots$$

then measurements can be made in the compressor at points at which the velocities are different, say before and behind the stator row, and the constants in the above relation determined. This has been done in the test compressor with free vortex blading. With this type of blading the axial component of velocity is constant and the difference of air velocity is a function only of the turning angle of the blade row. By operating the compressor at a constant throttle setting and varying the rotational speed a range of air velocities is attained, and it should be possible to determine the recovery factor. However, the velocity difference is small and consequently the temperature difference to be measured is small. The output from copper-constantan thermocouples under these conditions is of the order of a few microvolts. While the potentiometer in use is a very good one and thermal emf's in it are held to less than 0.3 microvolt, variations in the thermocouples and other parts of the circuit, or variations in the temperature of the incoming air, prevent the successful determination of the recovery factor by this method.

It should be emphasized in this regard that the difficulty of determining the recovery factor seems to be related directly to the low order of magnitude of velocity. Air velocities in the test compressor range from 50 to 150 feet per second and the dynamic temperature rise for velocities of this magnitude is from about 0.2 to about 1.9 degrees Fahrenheit. Thus the

difference to be measured is of the order of 0.1 to 0.3 degrees Fahrenheit (about 2 to 6 microvolts using copper-constantan thermocouples). This represents a recovery factor of about 50 percent at 50 feet per second and about 85% at 150 feet per second, and these are the differences encountered in the use of the adiabatic nozzle first described. The maximum difference obtained in the use of the test compressor as described above is about 2 microvolts. The probes in use have been calibrated for velocities above 200 feet per second at the Pratt and Whitney Aircraft Experimental Test Laboratory where they were developed (Reference 4). An indication of the scatter experienced in attempts to determine the recovery factor at low velocities is given in Figure 51.

It is anticipated that in the near future probes utilizing very small thermistors developed at the Bell Telephone Laboratories as temperature responsive resistance elements will be tested. The output from these elements will be more easily measured than the output from thermocouples and they have the outstanding advantage that the very small bead has a very high resistance and a low thermal capacity.

4:4 Determination of the Work Input to the Test Compressor

Actually, despite the difficulties described above and the fact that no consistent values for the recovery factor have been obtained, some significant work in the determination of the

distribution of the work input to the test compressor has been possible. In the present series of tests, the blading tested was of the free vortex type and was designed to produce a repeating flow pattern; i.e., velocity and direction of flow repeats point for point behind each stage. In the expanded single stage set-up, the velocity and direction are the same behind the entrance vanes and behind the stator, survey points 1 and 3 (see Figure 2). Thus, the determination of the rise in total temperature along a stream tube is simplified by the elimination of the recovery factor from the calculations.

Determination of the work input by the several sections of the rotor was made in this manner and is compared with the work input as represented by the quantity $2\int(\lambda_2 - \lambda_1)$ in figure 52. The method is far from perfect, however, and the total work input as indicated by the rise in total temperature did not agree with that indicated by the measurement of torque for all flow rates. Torque measurements are quite satisfactory for determining the total rate of work input since windage and friction losses in the test compressor are so small as to be negligible. Also, the torque coefficient agrees very well with the overall work coefficient obtained by integrating the quantity $2\int(\lambda_2 - \lambda_1)$ over the annulus. The total temperature measurements are of interest mainly to determine the radial distribution of work input. Hence, for the flow rates at which the two did not agree, the total temperature measurements were adjusted so that the total rate of work input indicated was the same as that

indicated by the torque input. It is these adjusted values which are shown in Figure 52. These adjustments were necessary on three of the five flow rates, no adjustment being necessary at the design flow rate, $\bar{\Phi} = 0.430$, nor at the next higher flow rate, $\bar{\Phi} = 0.460$. The adjustments necessary at the other flow rates were 3.64 percent of the total rate of work input at a flow rate of $\bar{\Phi} = 0.370$, 3.8 percent at $\bar{\Phi} = 0.400$, and 2.56 percent at $\bar{\Phi} = 0.490$. The rotor losses at these flow rates were 8.9 percent, 5.6, percent, and 6 percent, so that the correction of the data is significant when considered in this connection.

Examination of the curves in Figure 52 shows the feasibility of using the method described to determine the distribution of work input along the radius of the rotor. After the adjustments were made, the local work coefficient as determined by the measurement of total temperature rise differed from that determined by calculation of the change in angular momentum of the air by a maximum of about five percent outside the boundary regions. Within the boundary regions there is mixing and heat transfer to the walls of the compressor. Also, there is some growth of the boundary layer between the points of measurement causing a deviation from a repeating flow pattern. Together, these effects may account for the fact that total temperature measurements indicate a lower work coefficient in the boundary regions than does the change of angular momentum. It should be noted, however, that the calculation of the change in angular momentum in these

regions is also subject to gross inaccuracies. In a region of high shear flow such as near the walls of the compressor, it is extremely difficult to determine either the direction of flow or the velocity.

As far as accuracy of measurement is concerned, in the region outside the boundary layers, the two methods are probably equally as good. From the standpoint of time and labor involved, however, the method of measuring the change in total temperature has many advantages, and it is hoped that with further development, it will prove to be a dependable as well as simple method for the determination of the distribution of work input.

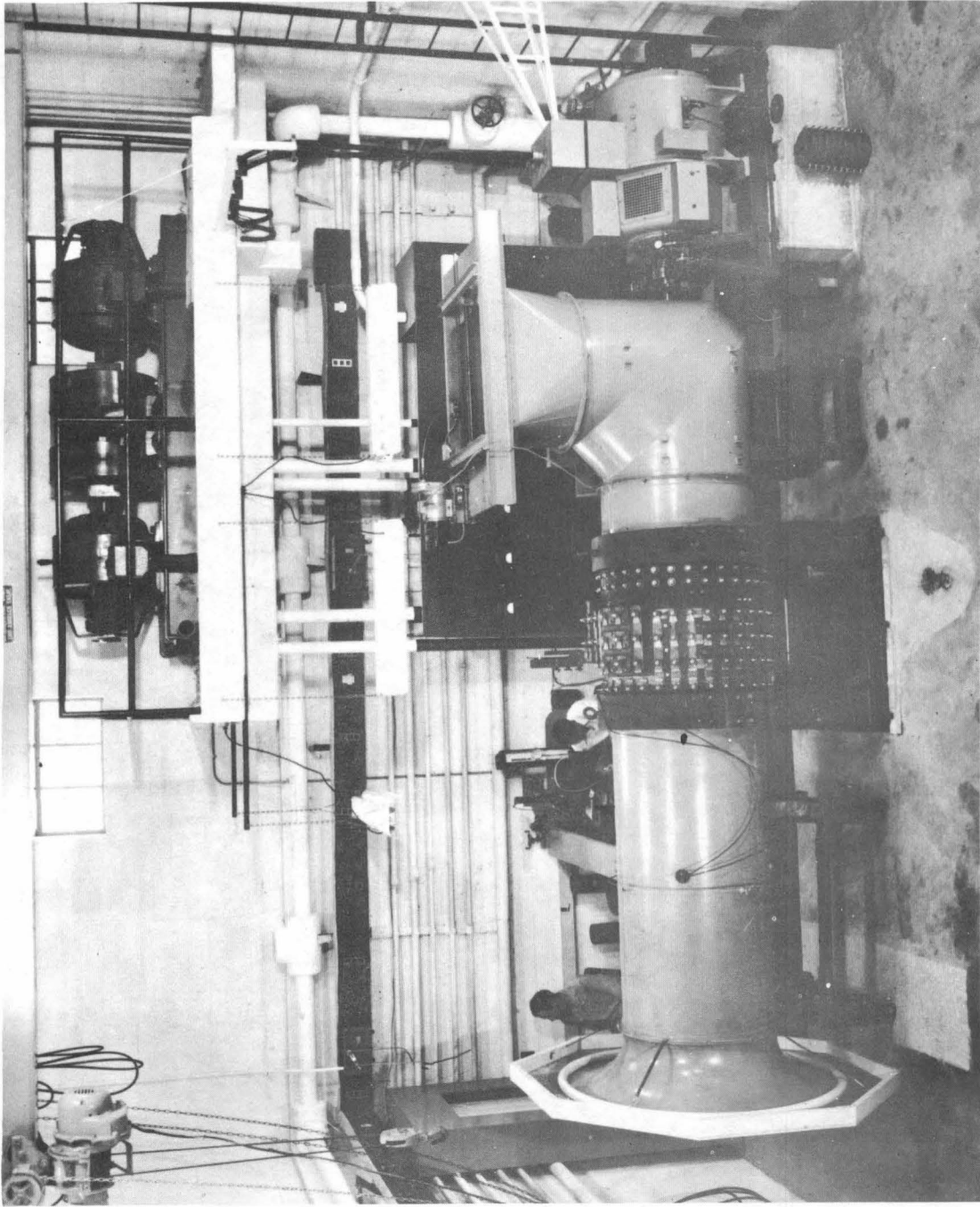
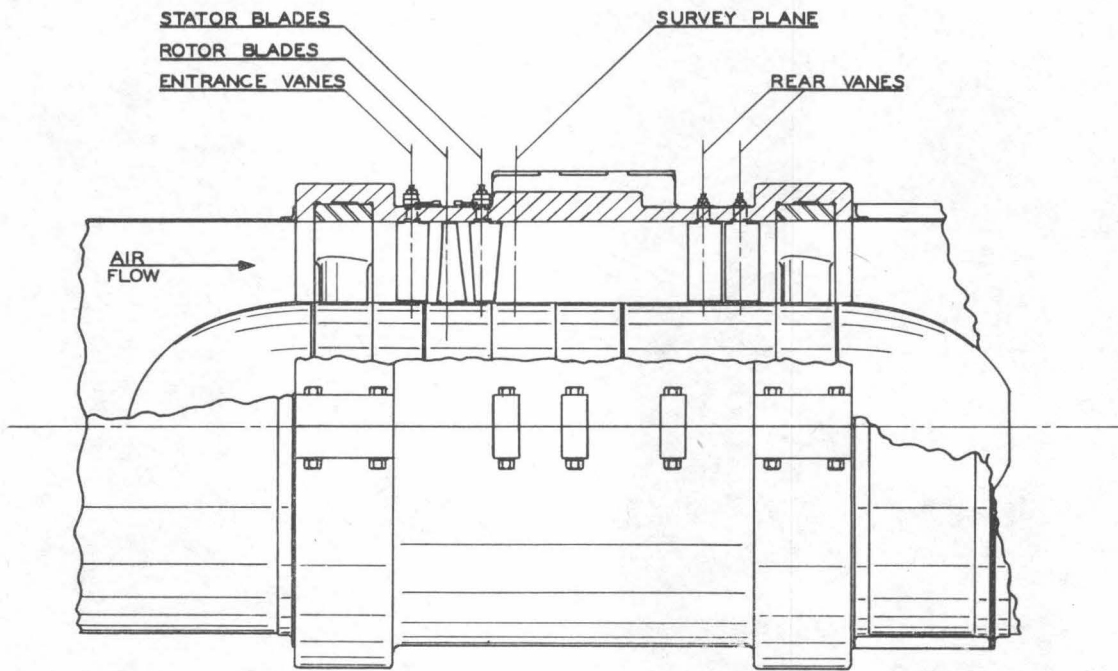
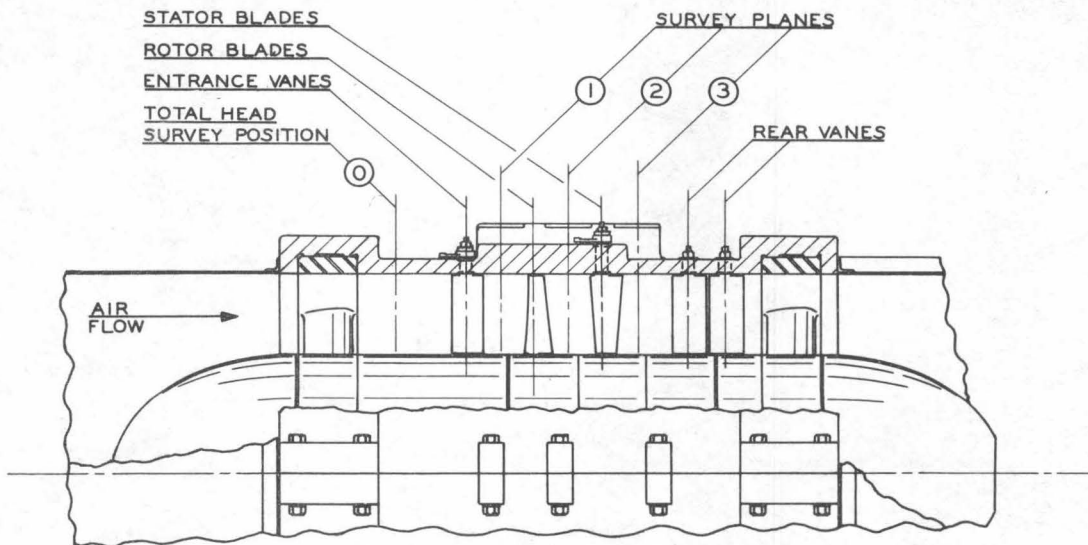


Fig. 1 General View of Test Installation



CONVENTIONAL SINGLE STAGE



EXPANDED SINGLE STAGE

FIG. 2 COMPRESSOR - SINGLE STAGE BLADING

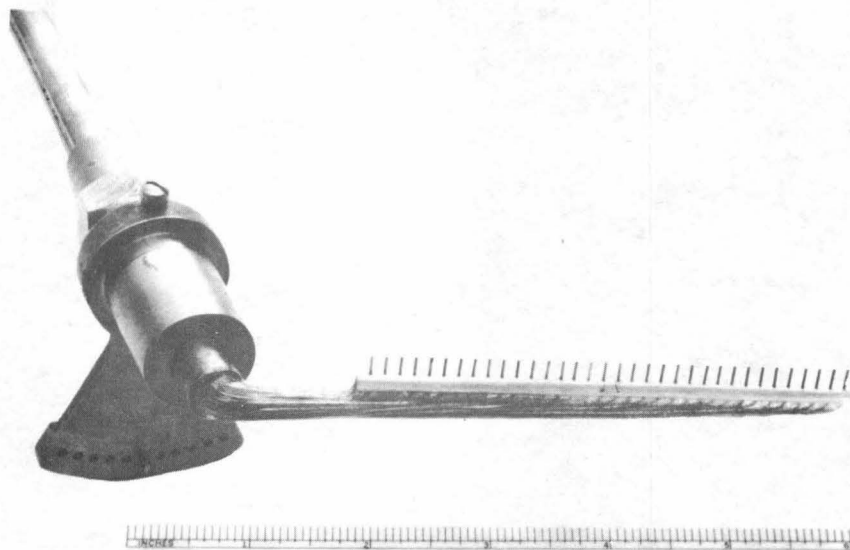


Fig. 3 Total Head Rake

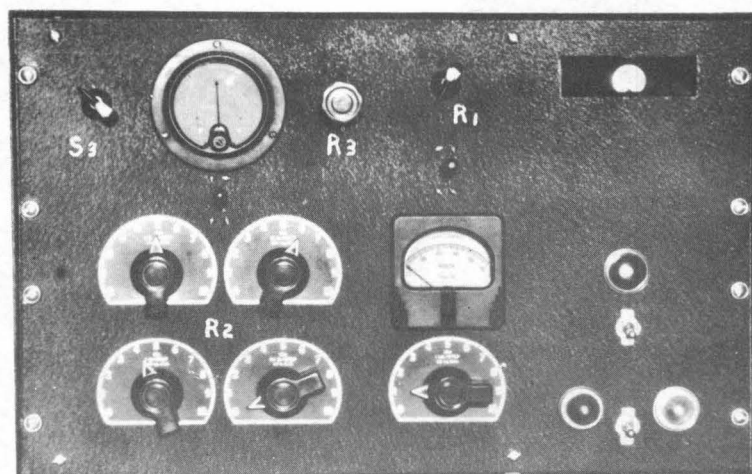
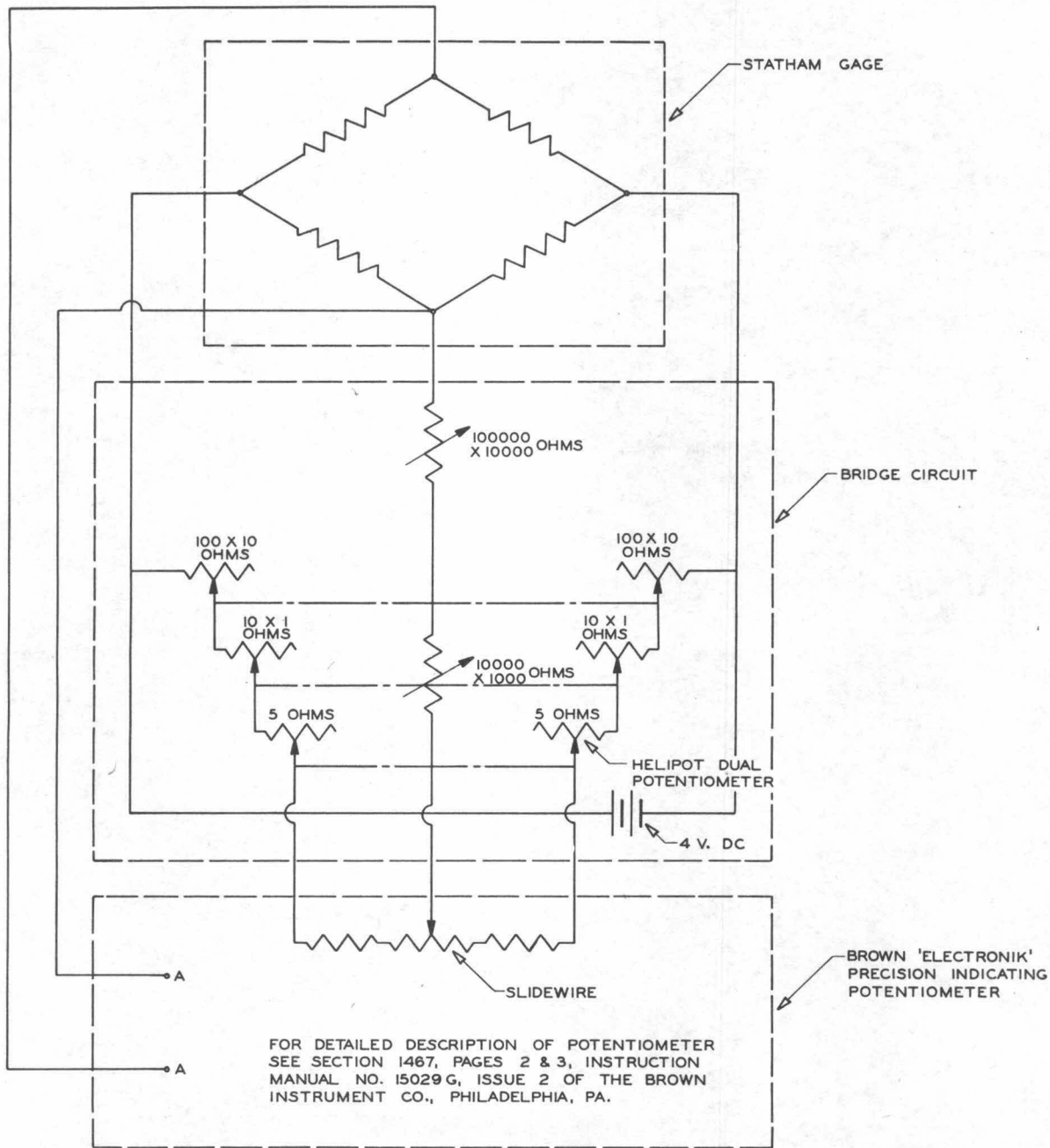


Fig. 4 Speed Controller Panel

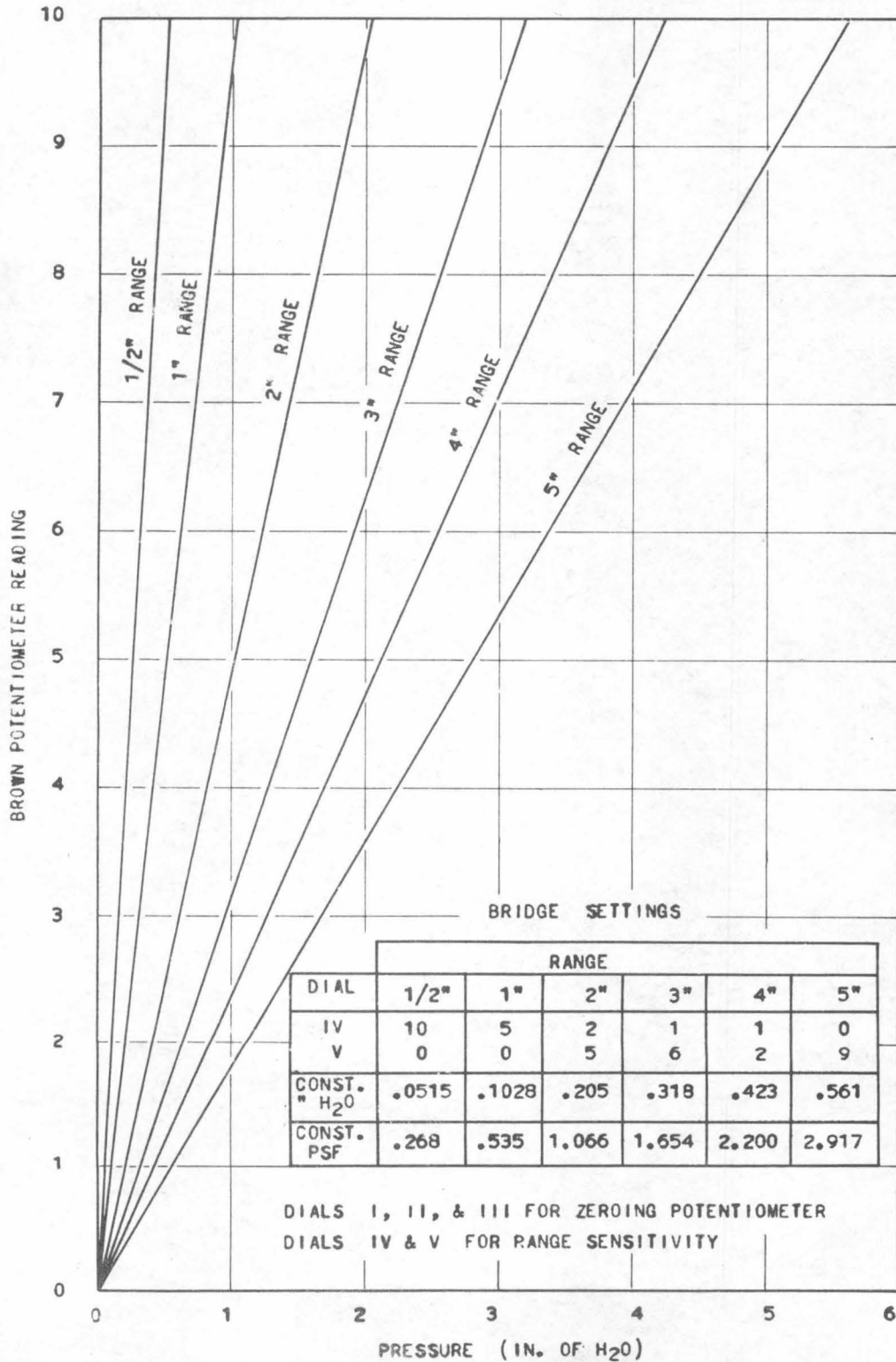


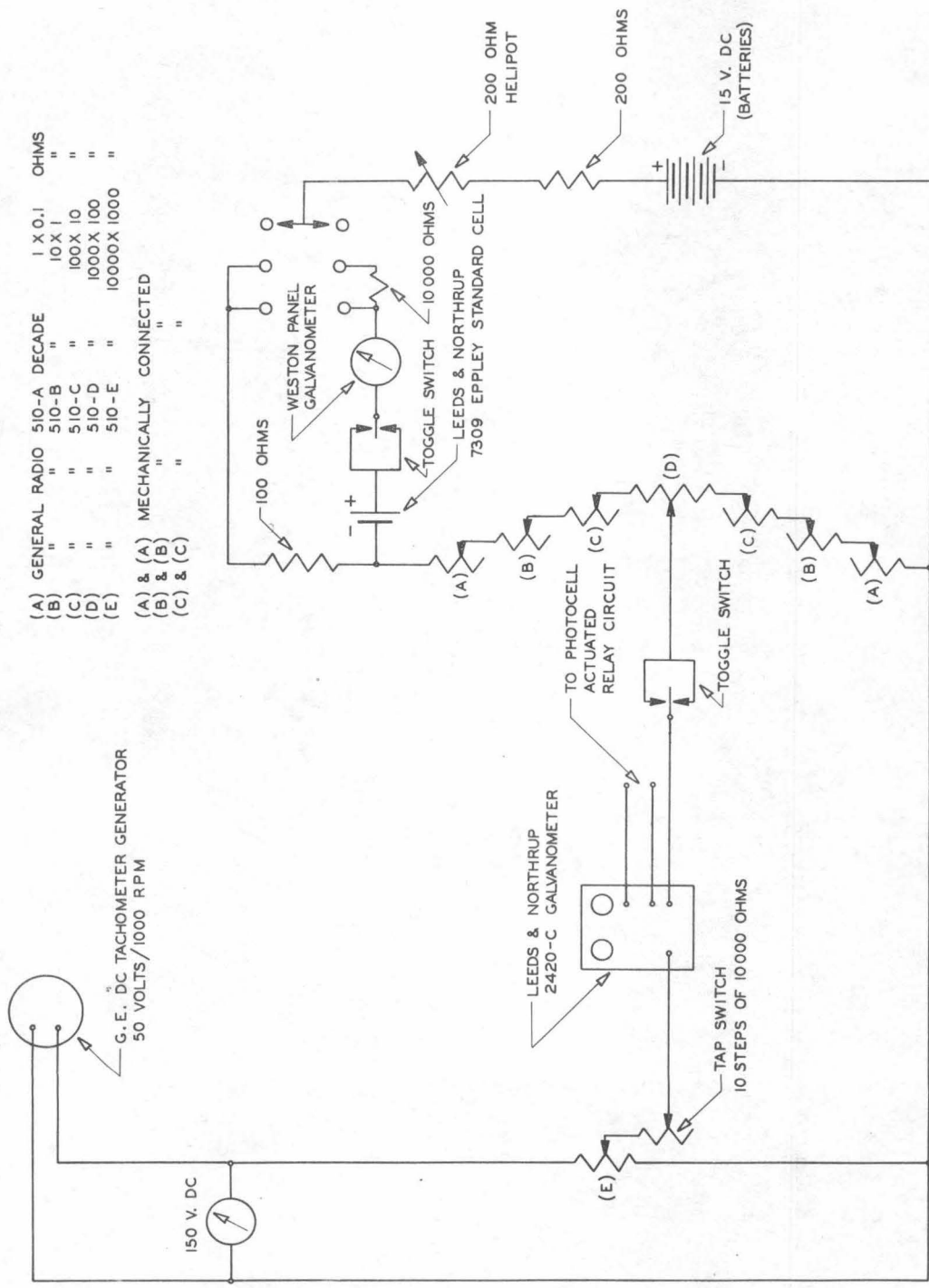
100 X 10 OHMS REPRESENTS 100 OHM RHEOSTAT ADJUSTABLE IN 10 OHM STEPS
MECHANICAL CONNECTION
BRIDGE DESIGNED & MFGD. BY THIELE WRIGHT CO., LOS ANGELES, CALIF.

FIG. 5 PRESSURE PICKUP CIRCUIT DIAGRAM

FIGURE 6

STATHAM GAGE CALIBRATION CURVE
 FOR STATHAM GAGE PRESSURE TRANSMITTER
 WITH BROWN ELECTRONIK PRECISION INDICATING POTENTIOMETER
 STATHAM MODEL P5-0.20 - 250 BROWN MODEL NO. 156 X 15V
 SERIAL NO. 95 SERIAL NO. 536611





DESIGNED & MFGD. BY THIELE WRIGHT CO.

FIG. 7a SPEED CONTROL CIRCUIT

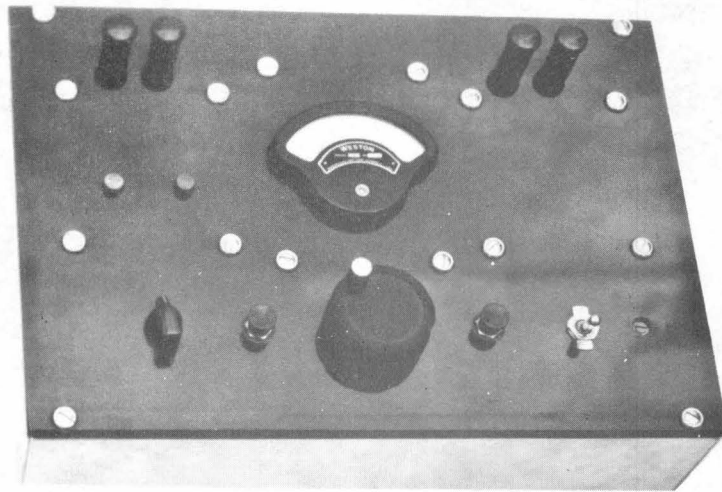


Fig. 8 Potentiometer Panel

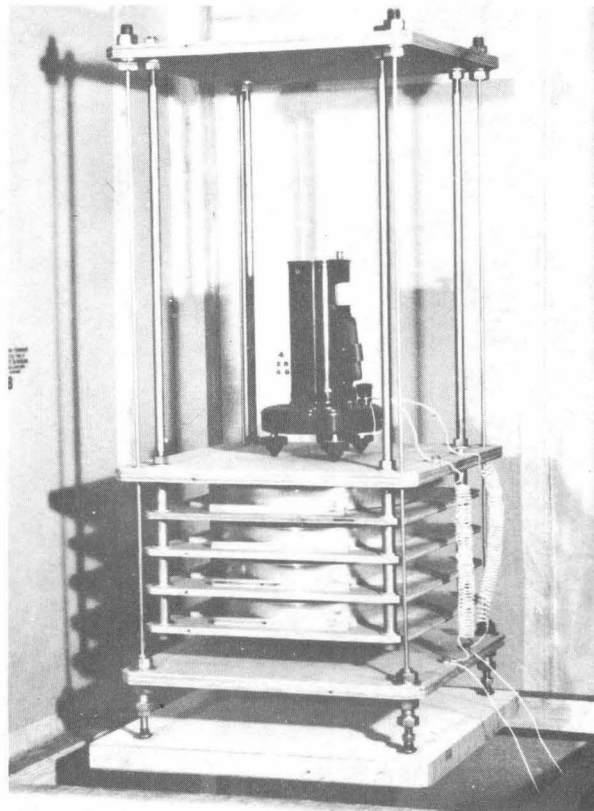


Fig. 9 Galvanometer Suspension

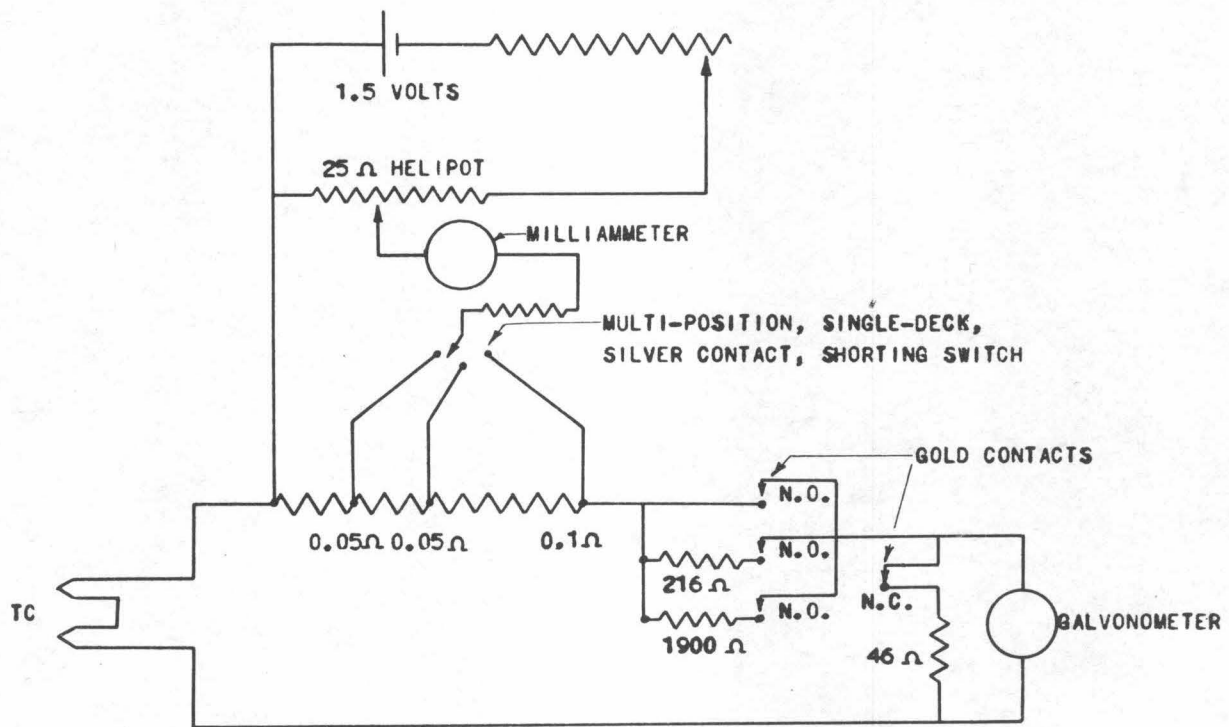


FIGURE 10
 POTENTIOMETER CIRCUIT DIAGRAM

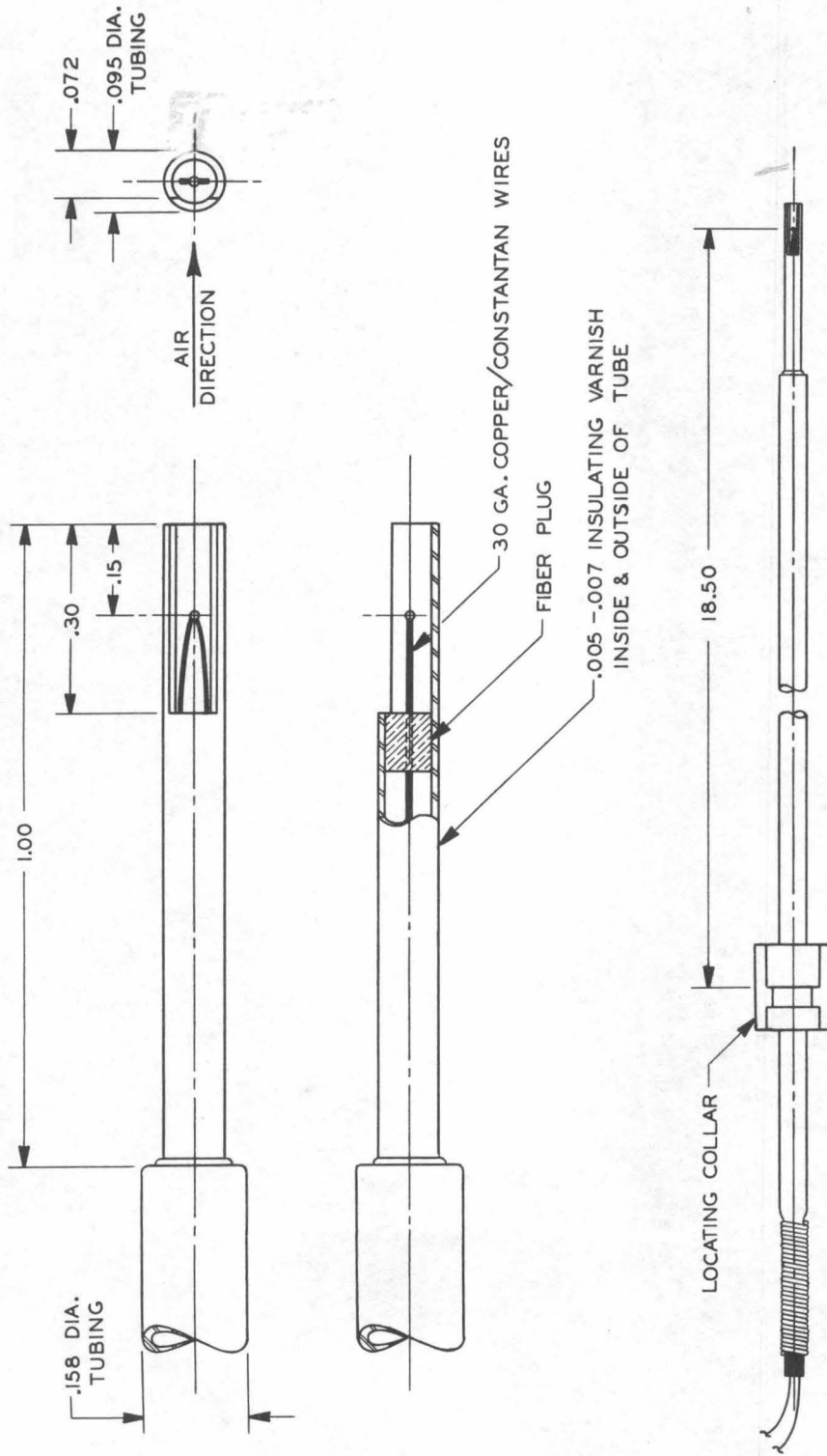


FIG. 11 TOTAL TEMPERATURE PROBE

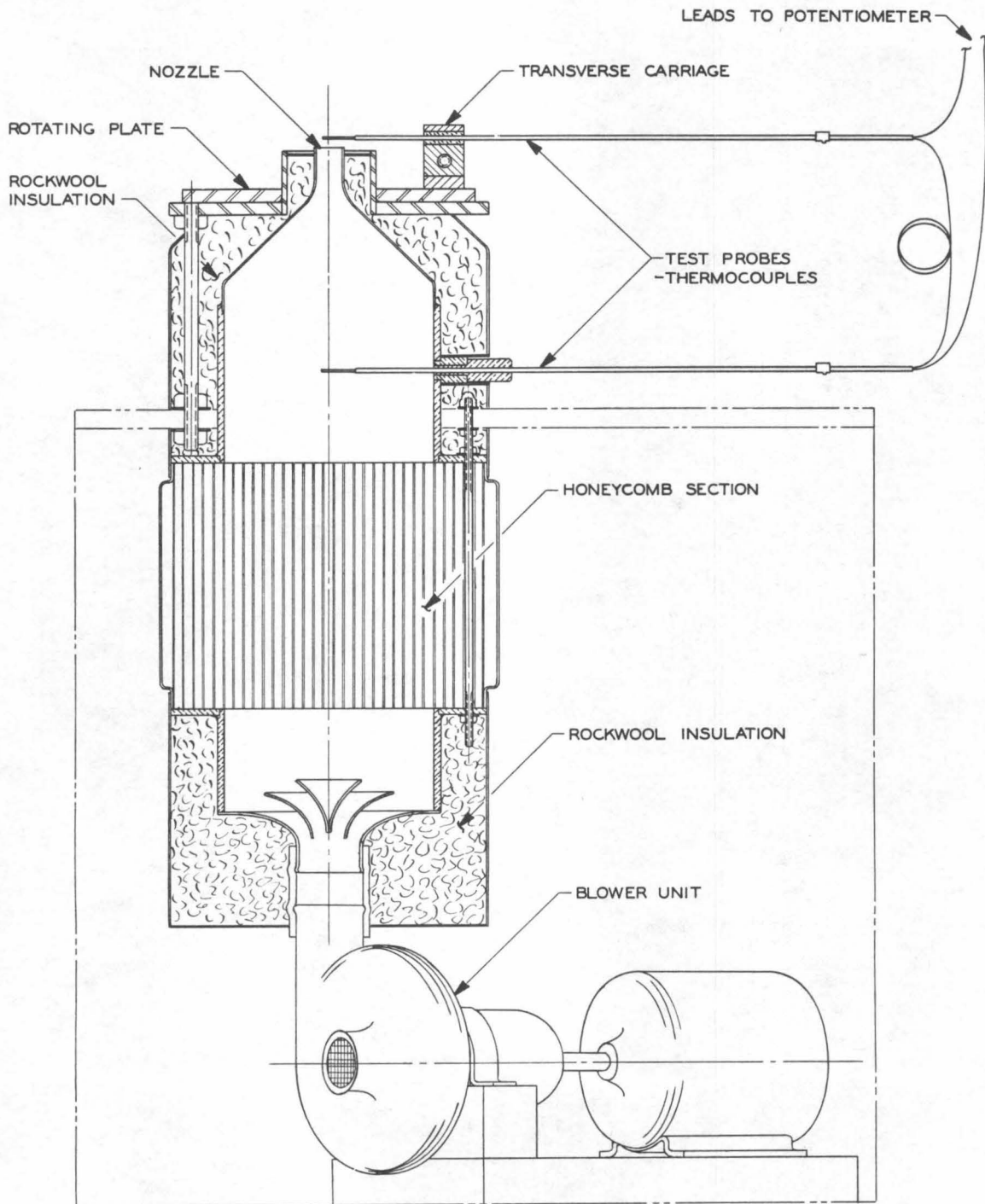


FIG. 12 CALIBRATION NOZZLE

FIGURE 13
LEAVING ANGLE FOR PRE-ROTATION VANES

$$8.75 \times 10^4 < R_E < 11.6 \times 10^4$$

FREE VORTEX BLADING

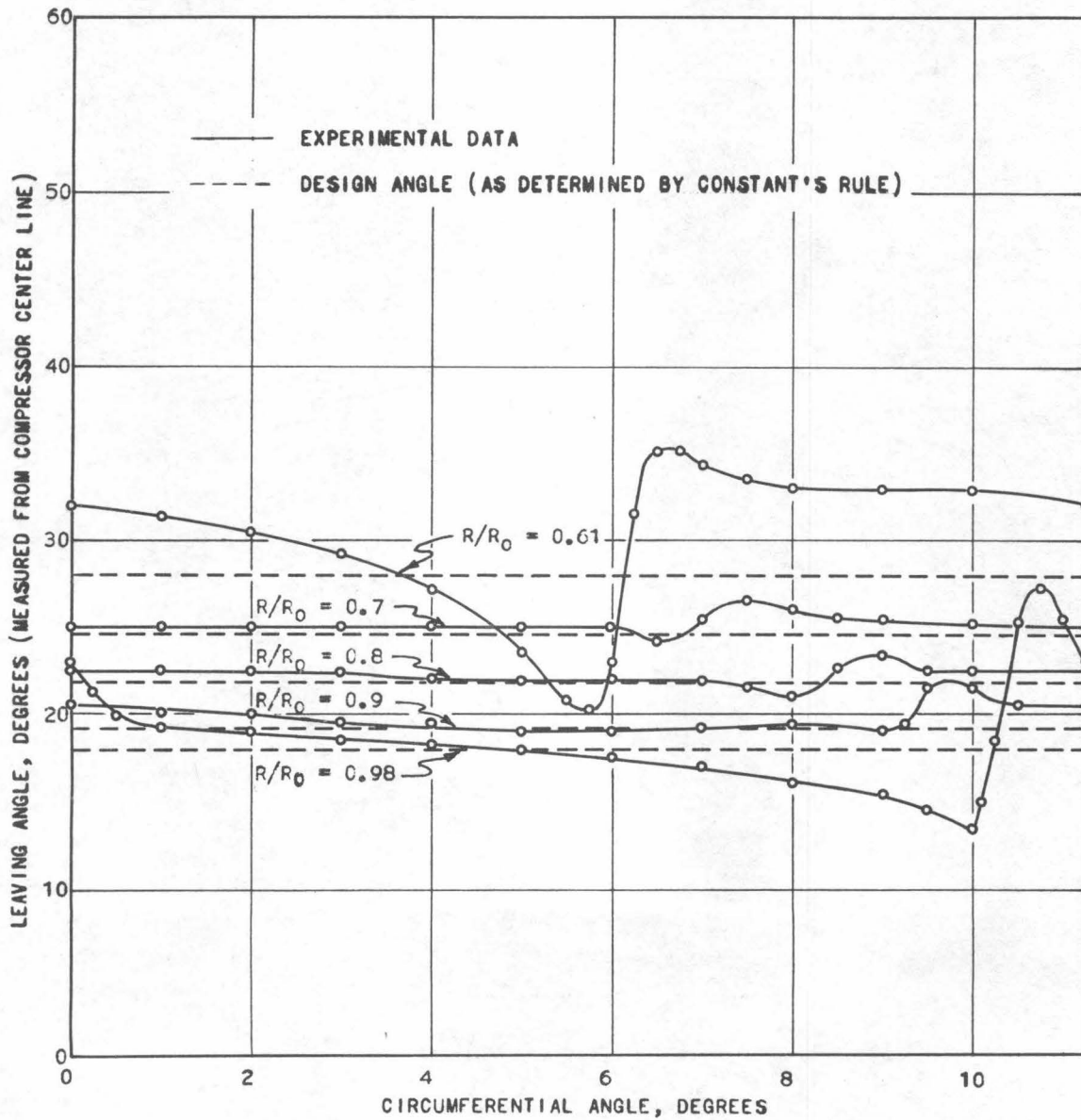


FIGURE 14

FLOW CHARACTERISTICS OF PRE-ROTATION VANES, FREE VORTEX BLADING

FLOW COEFFICIENT, $\bar{\Phi}_0 = 0.431$

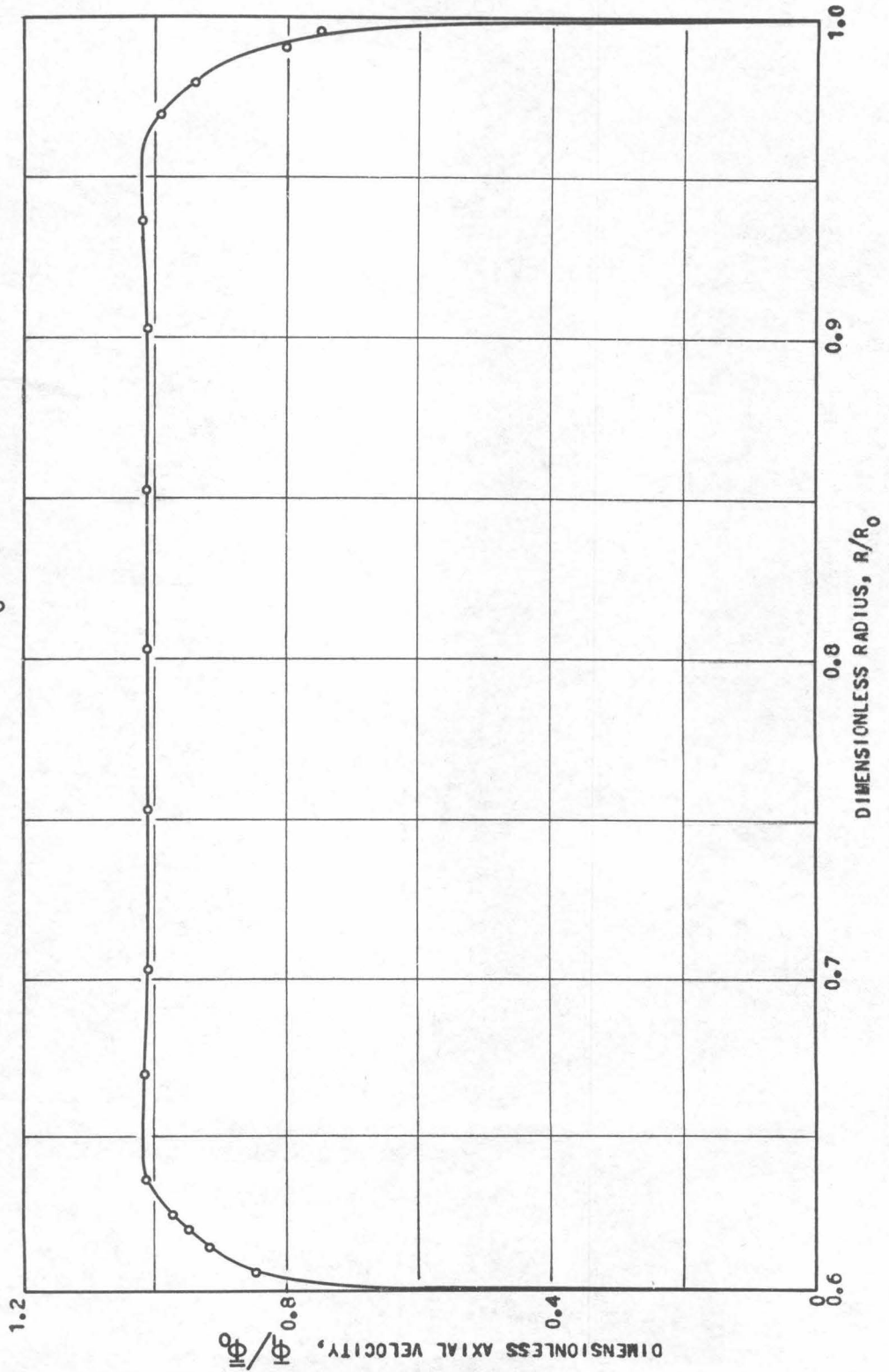


FIGURE 15

FLOW CHARACTERISTICS OF PRE-ROTATION VANES, FREE VORTEX BLADING

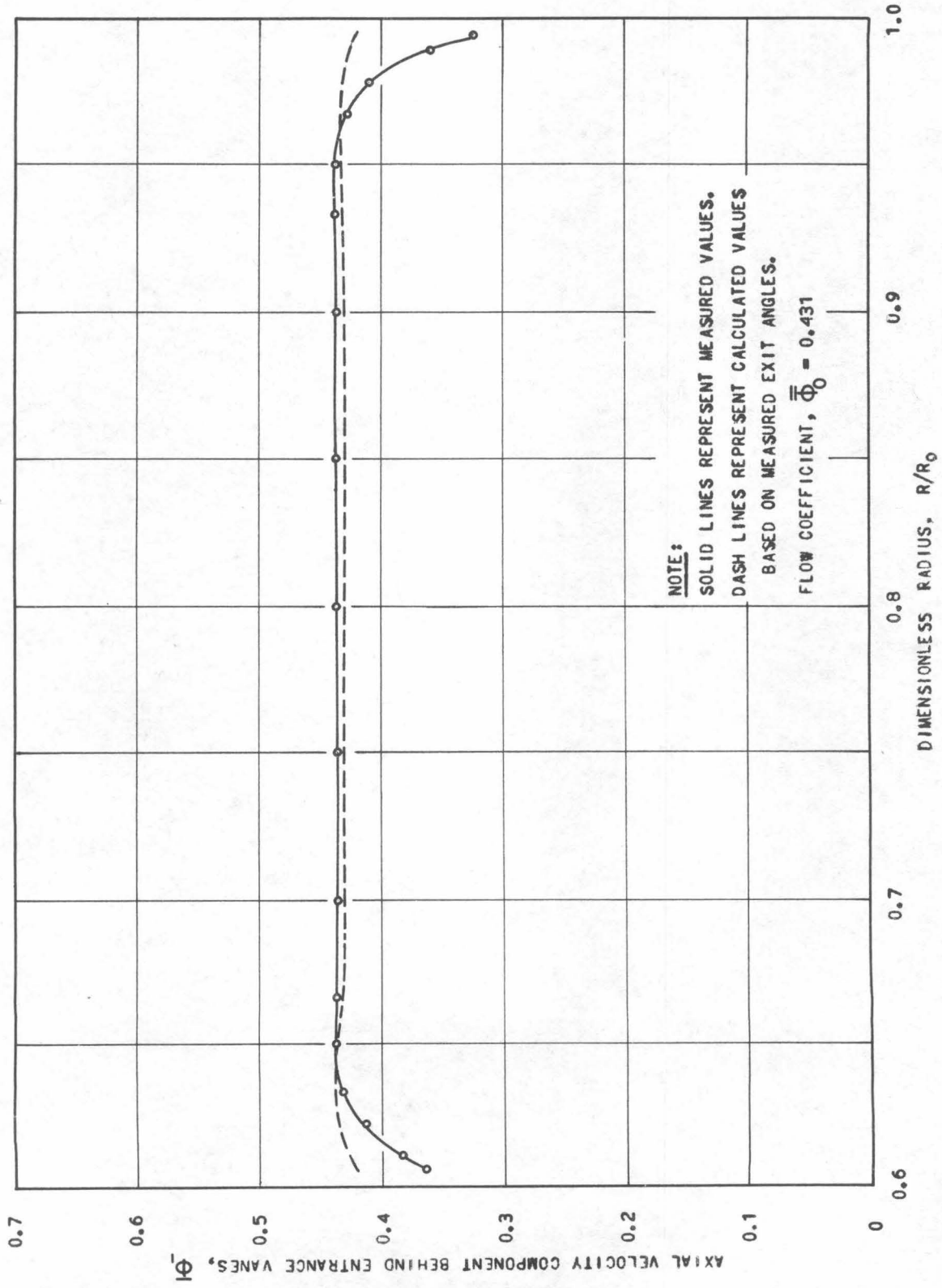


FIGURE 16

FLOW CHARACTERISTICS BEHIND PRE-ROTATION VANES, FREE VORTEX BLADING
AVERAGE TOTAL PRESSURE BEHIND PRE-ROTATION VANES

FLOW COEFFICIENT, $\bar{\Phi}_0 = 0.431$

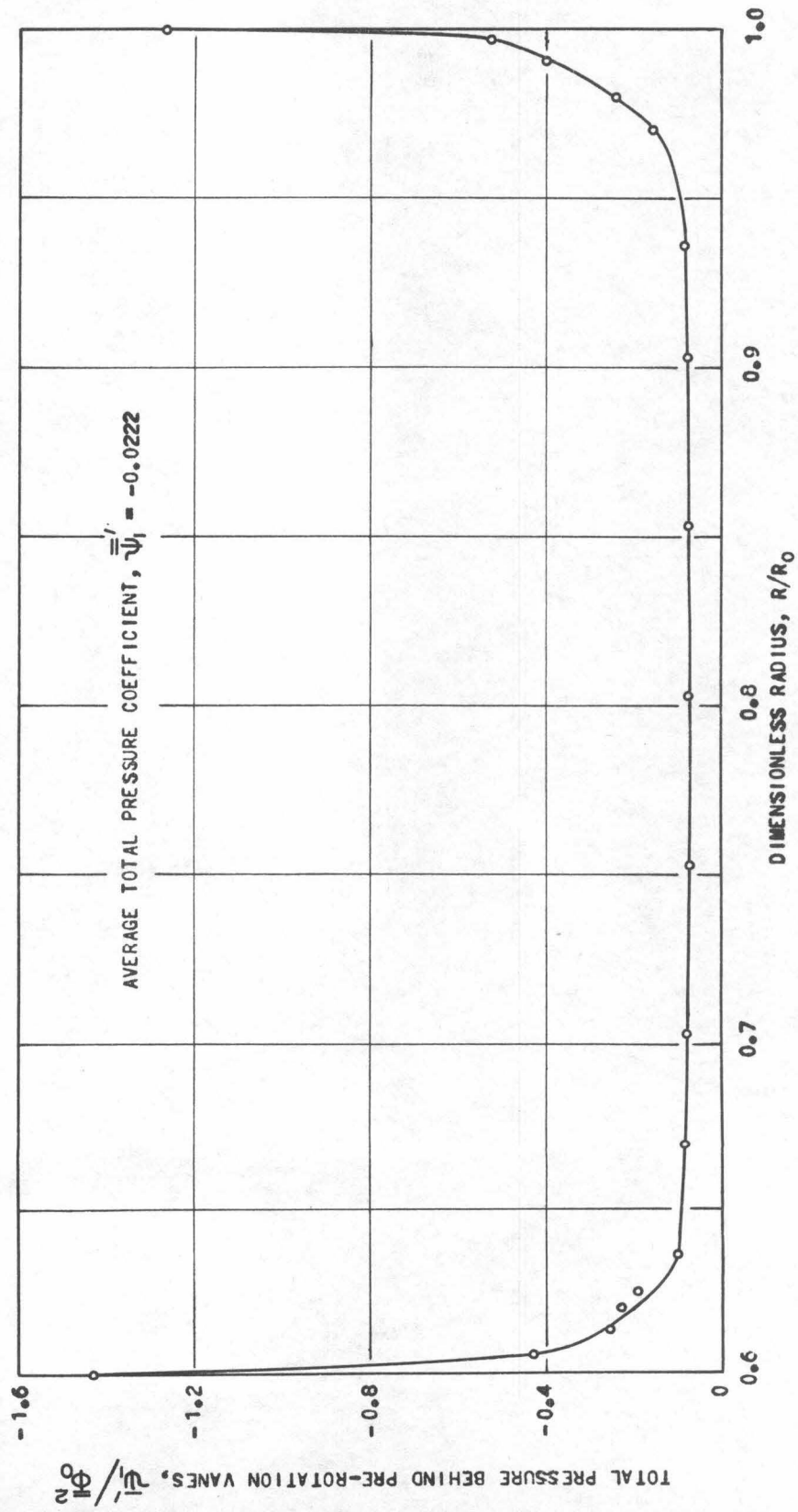
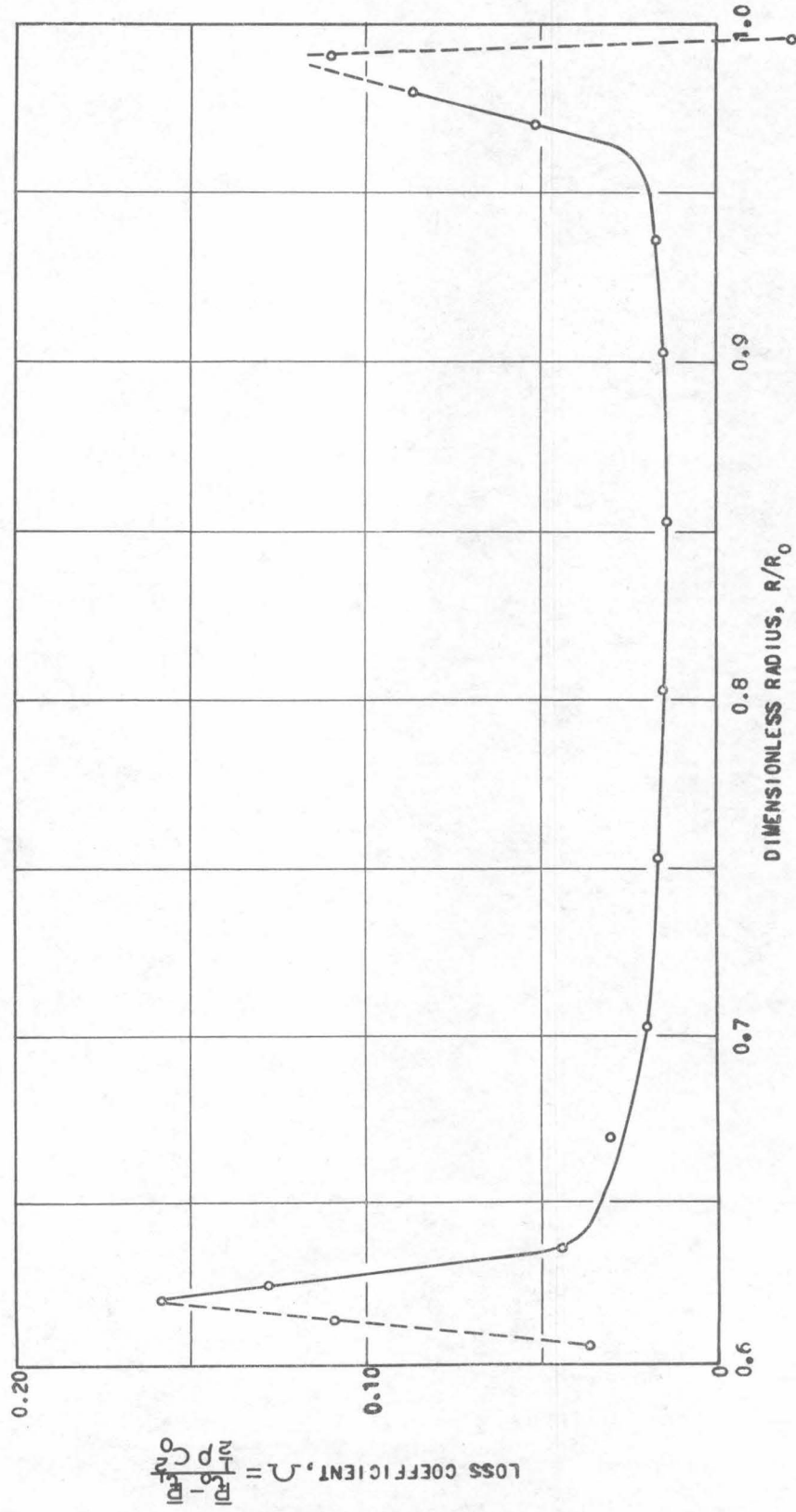


FIGURE 17

FLOW CHARACTERISTICS BEHIND PRE-ROTATION VANES, FREE VORTEX BLADING

LOSS THROUGH PRE-ROTATION VANES

FLOW COEFFICIENT, $\Phi_1 = 0.428$



FLOW CHARACTERISTICS BEHIND ROTOR, FREE VORTEX BLADING

ROTOR LEAVING ANGLE

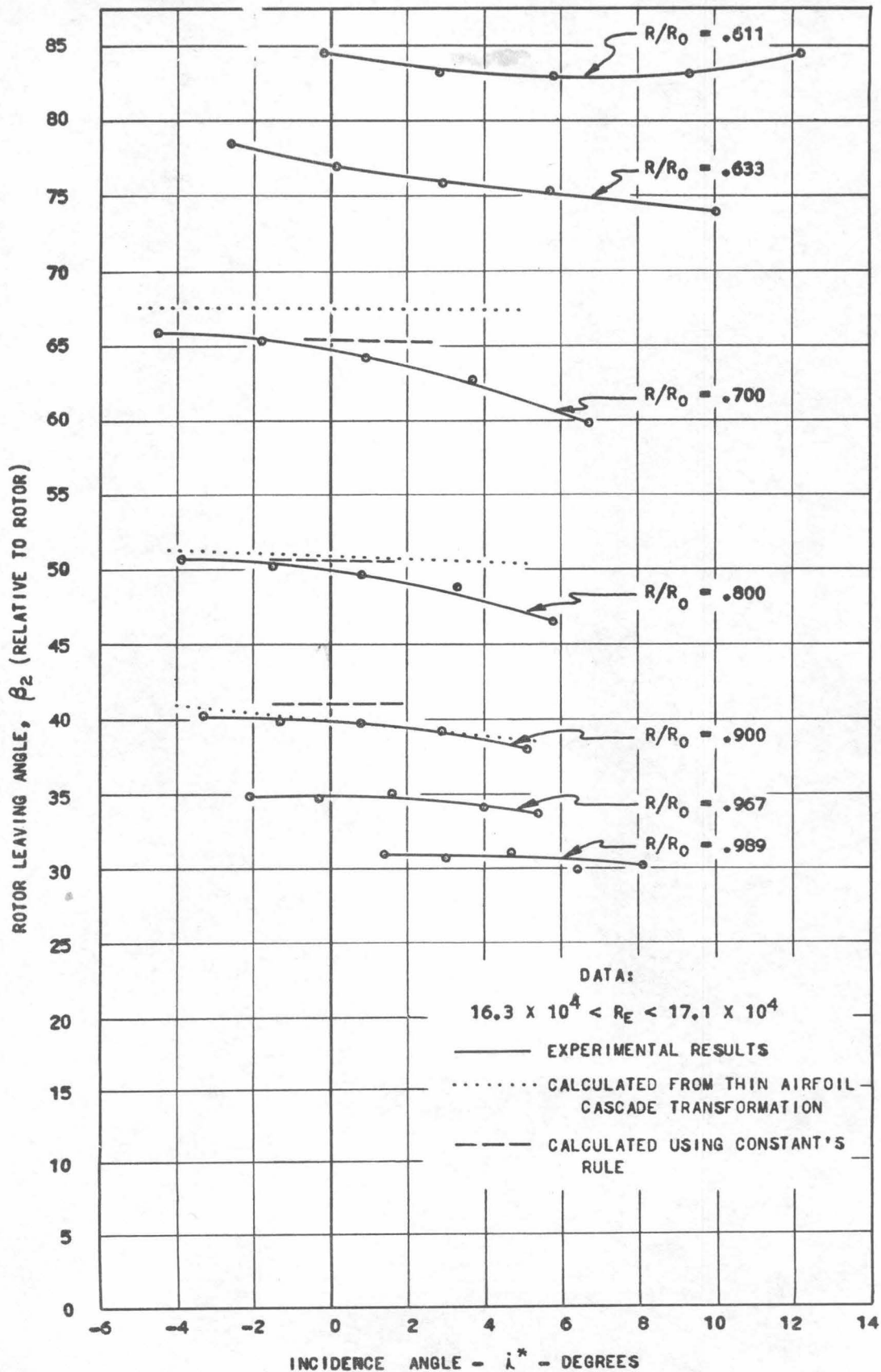


FIGURE 18

FIGURE 19

FLOW CHARACTERISTICS THROUGH ROTOR, FREE VORTEX BLADING
AVERAGE AXIAL VELOCITY THROUGH ROTOR

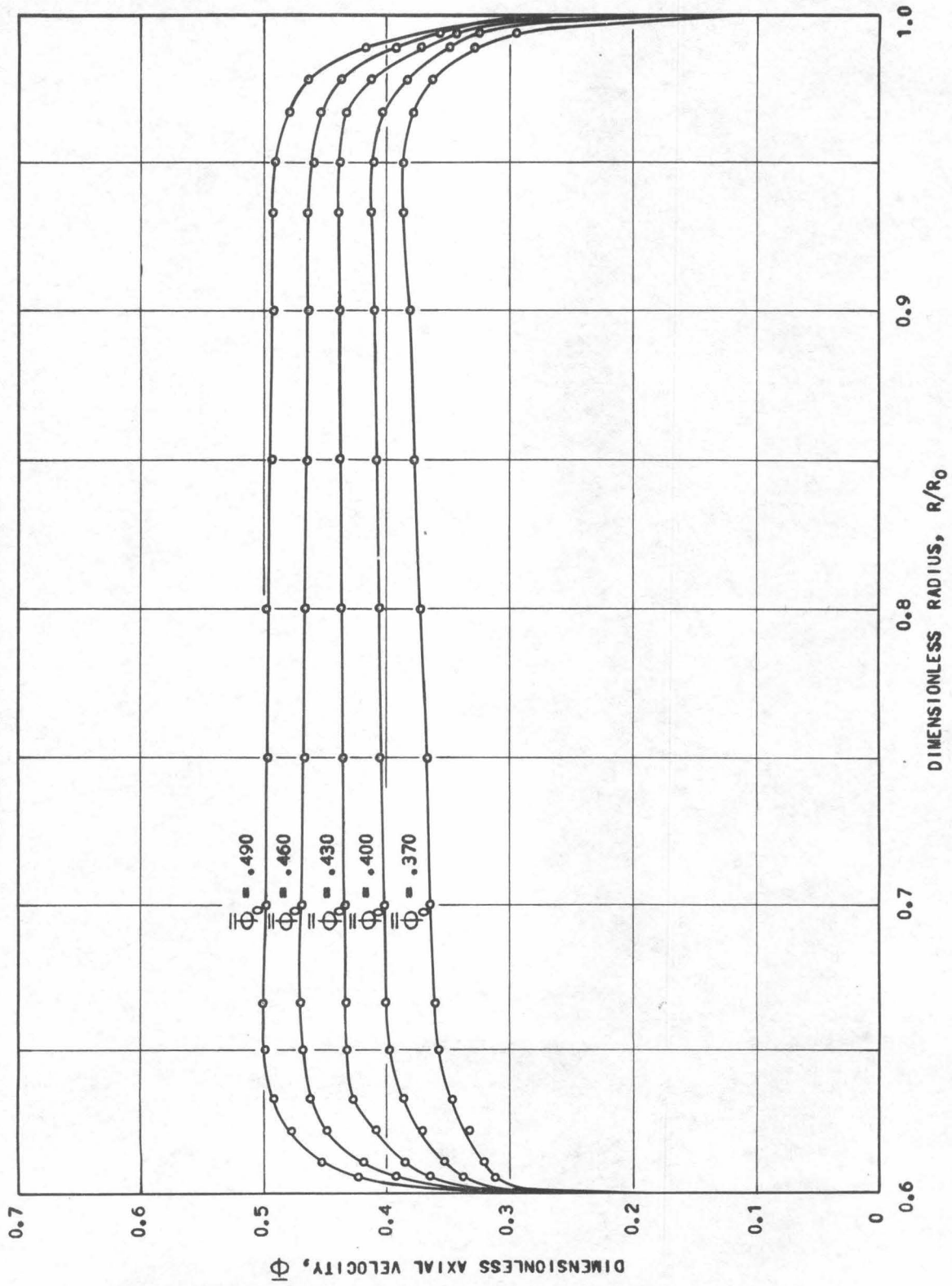


FIGURE 20
 FLOW CHARACTERISTICS BEHIND ROTOR, FREE VORTEX BLADING
 COMPARISON OF MEASURED AND CALCULATED AXIAL VELOCITY BEHIND ROTOR

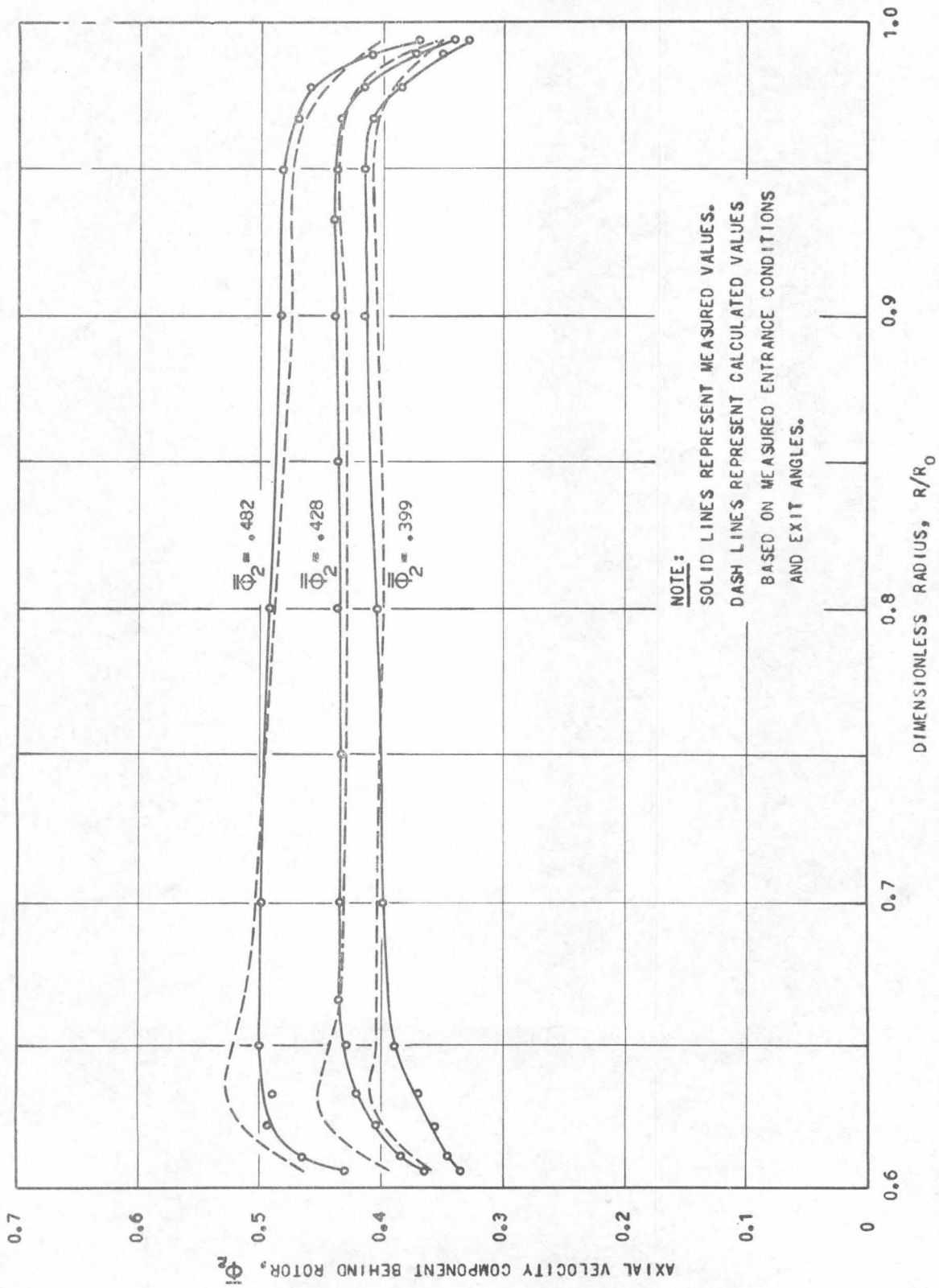


FIGURE 21

TORQUE CURVE FOR EXPANDED SINGLE STAGE COMPRESSOR

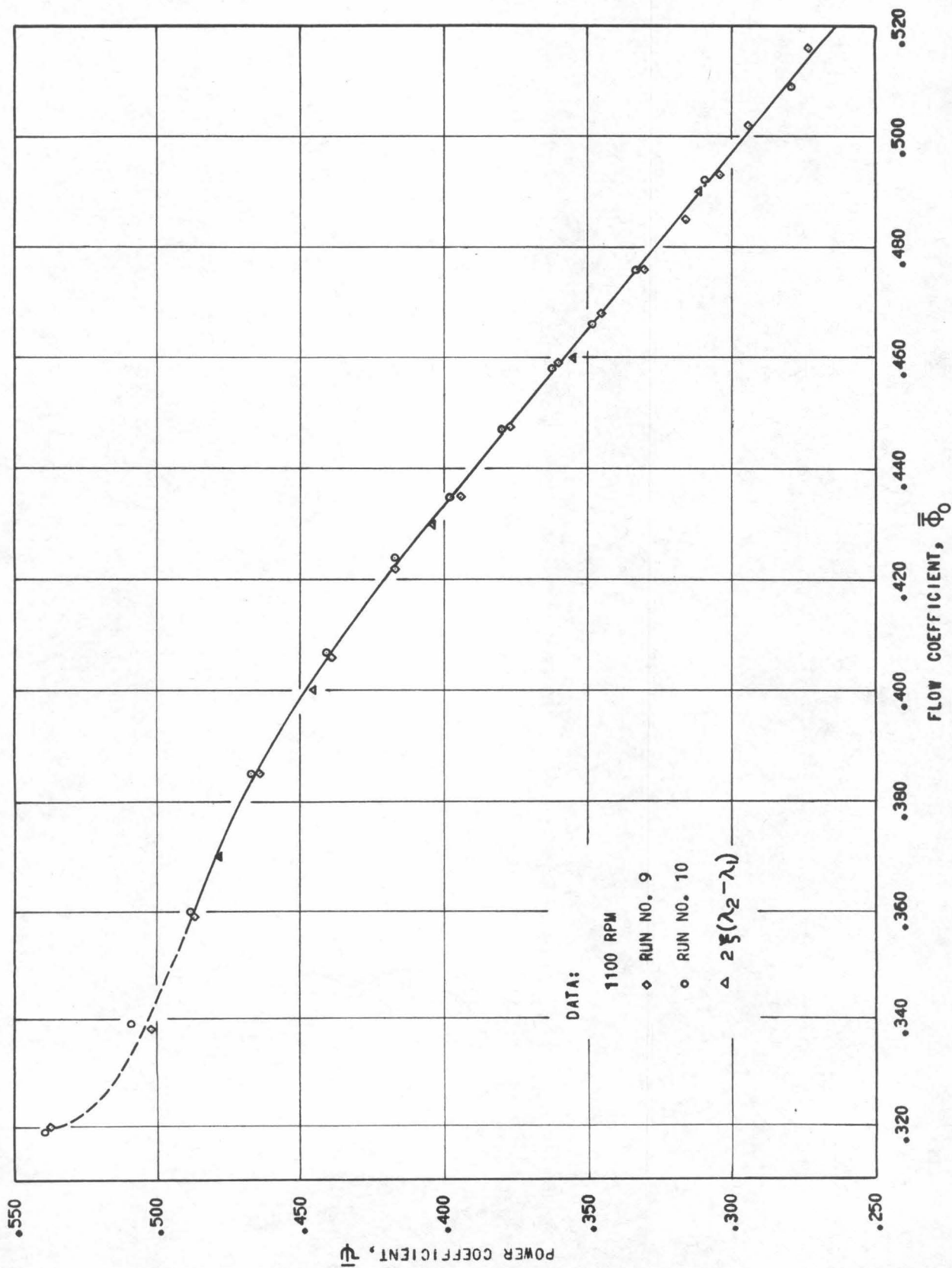


FIGURE 22

FREE VORTEX BLADING - ROTOR
TOTAL PRESSURE RISE THROUGH ROTOR

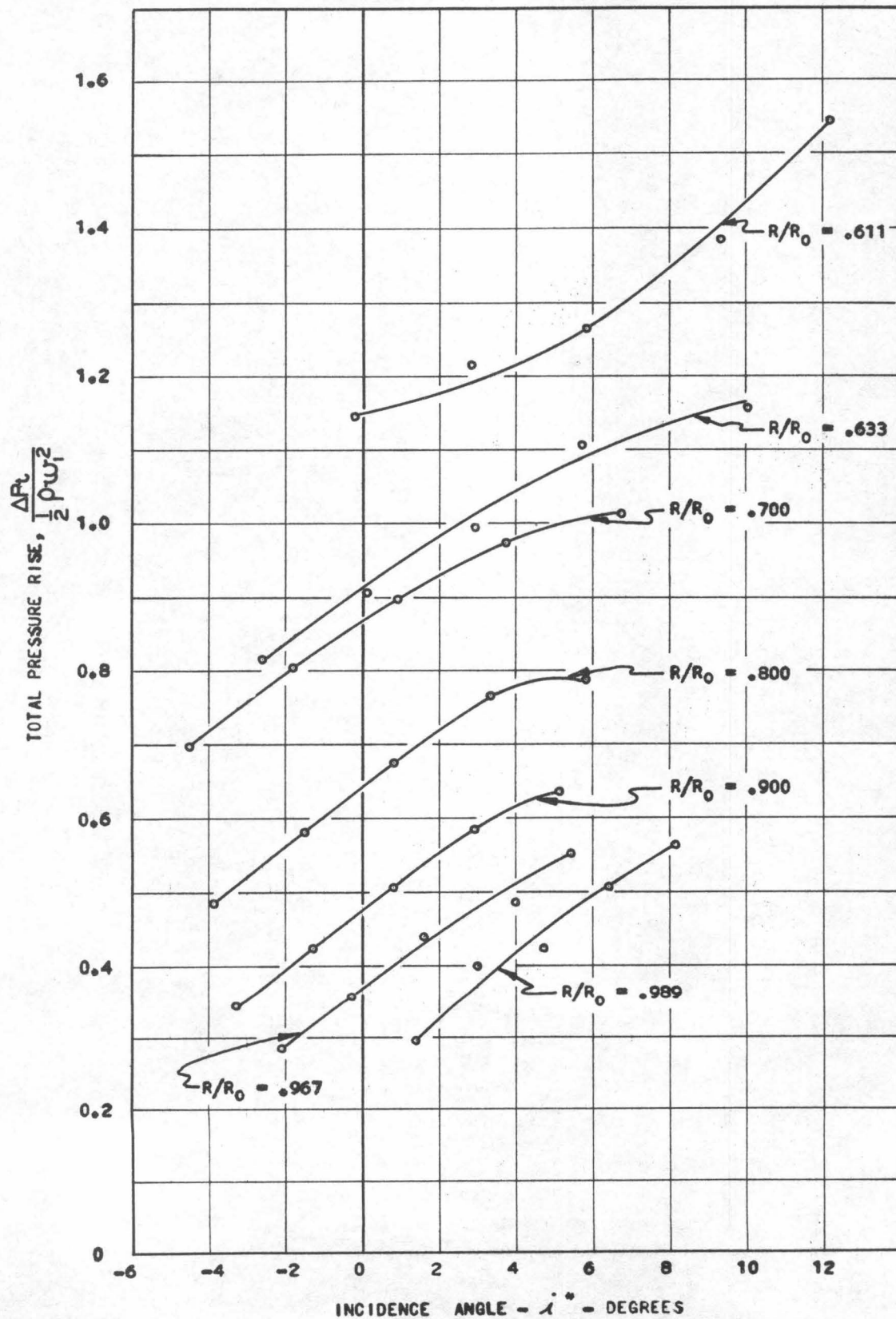


FIGURE 23

FREE VORTEX BLADING - ROTOR

CHANGE IN ANGULAR MOMENTUM THROUGH ROTOR (BASED ON ENTERING VELOCITY RELATIVE TO ROTOR)

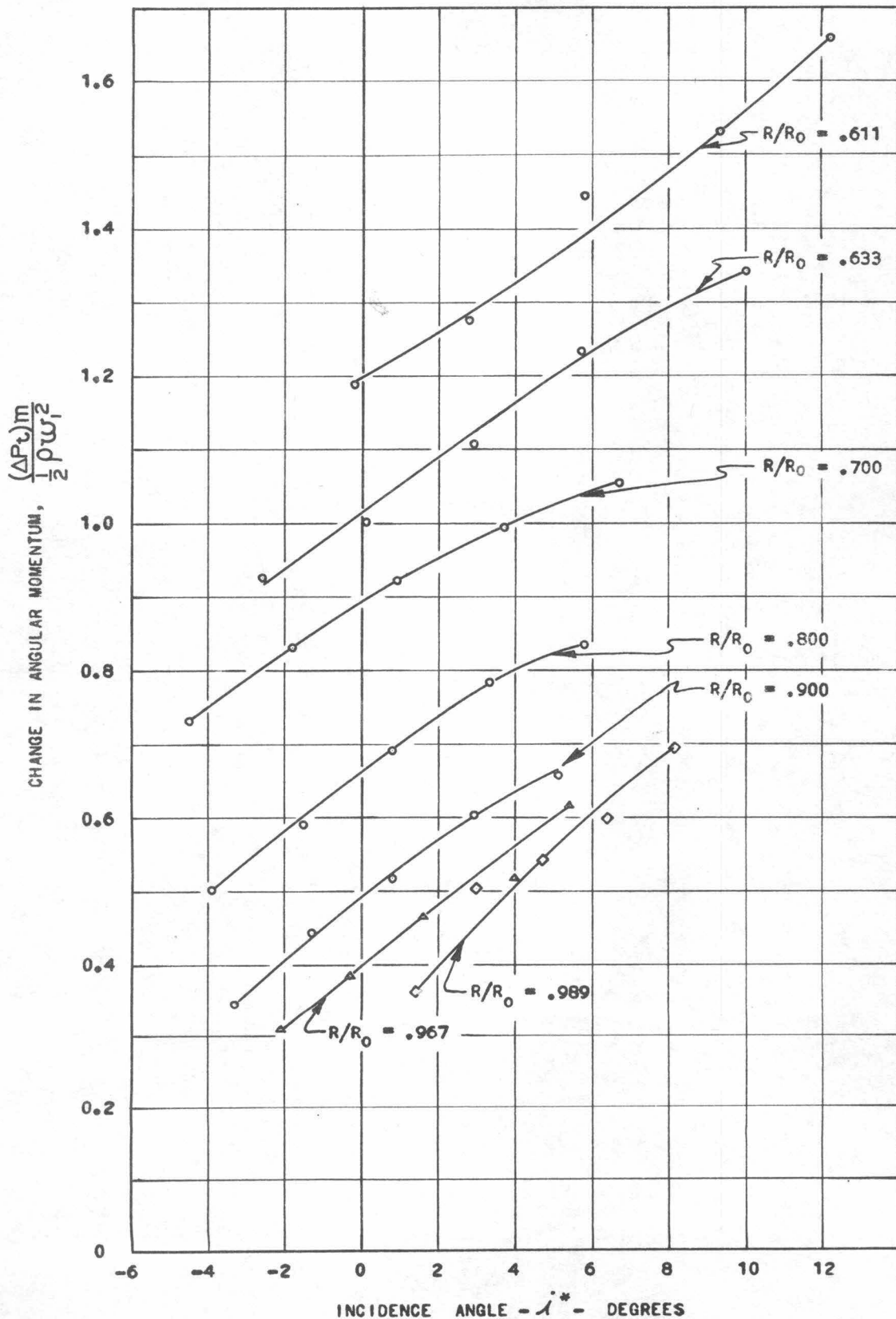


FIGURE 24A

FREE VORTEX BLADING - ROTOR
TOTAL PRESSURE RISE THROUGH ROTOR

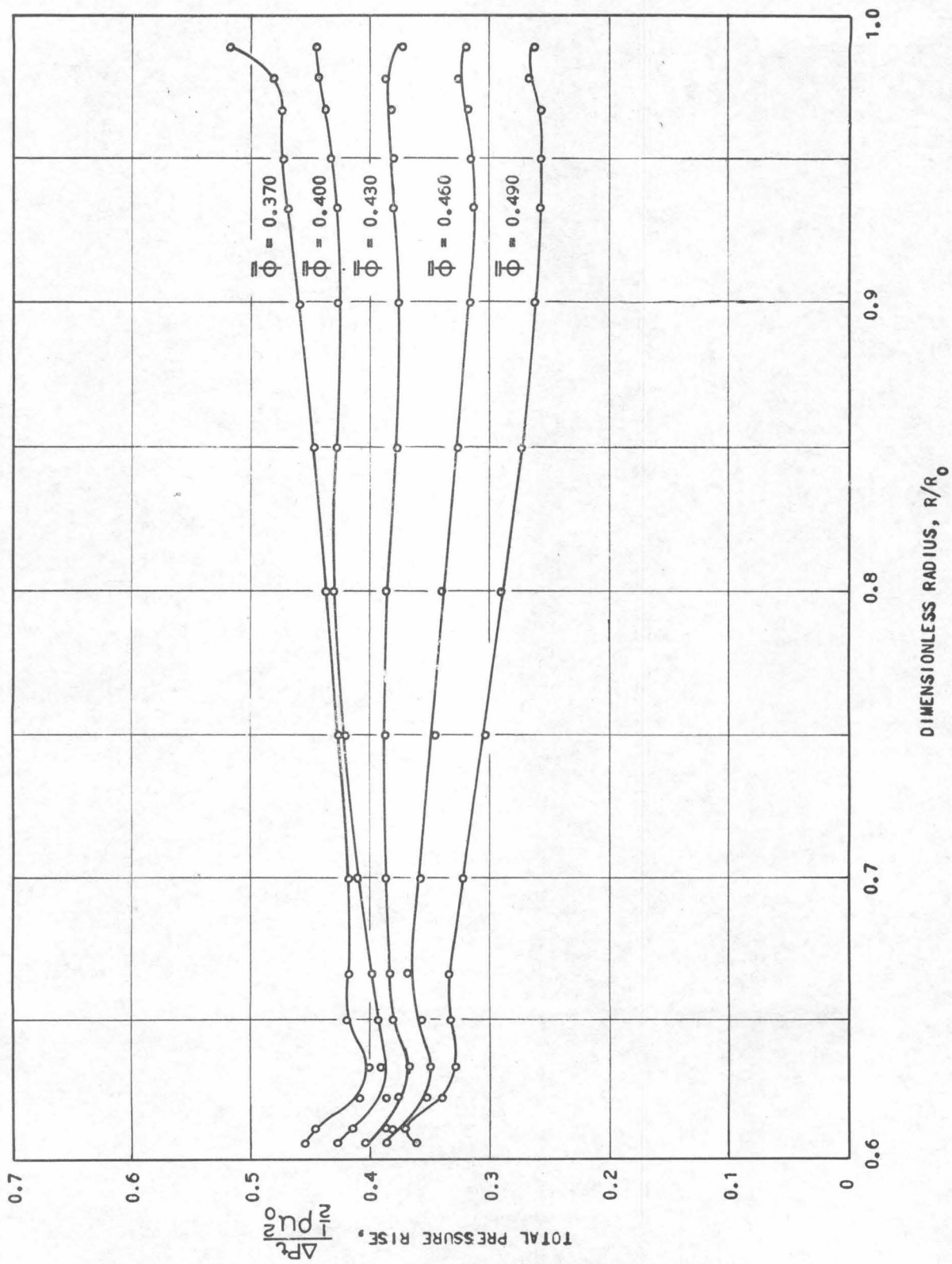
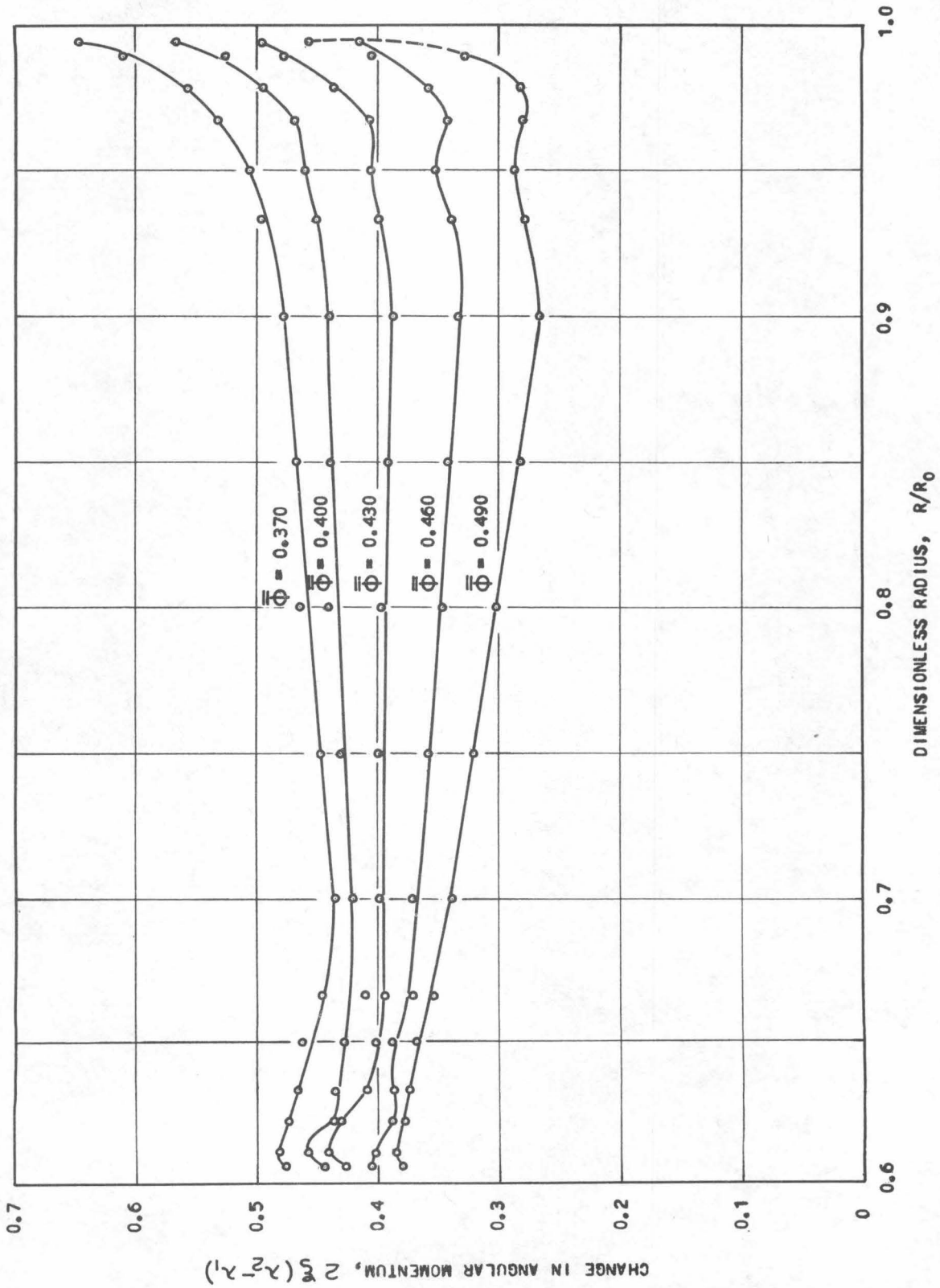


FIGURE 248

FREE VORTEX BLADING - ROTOR
CHANGE IN ANGULAR MOMENTUM THROUGH ROTOR



FREE VORTEX BLADING - ROTOR

ROTOR LOSS COEFFICIENT

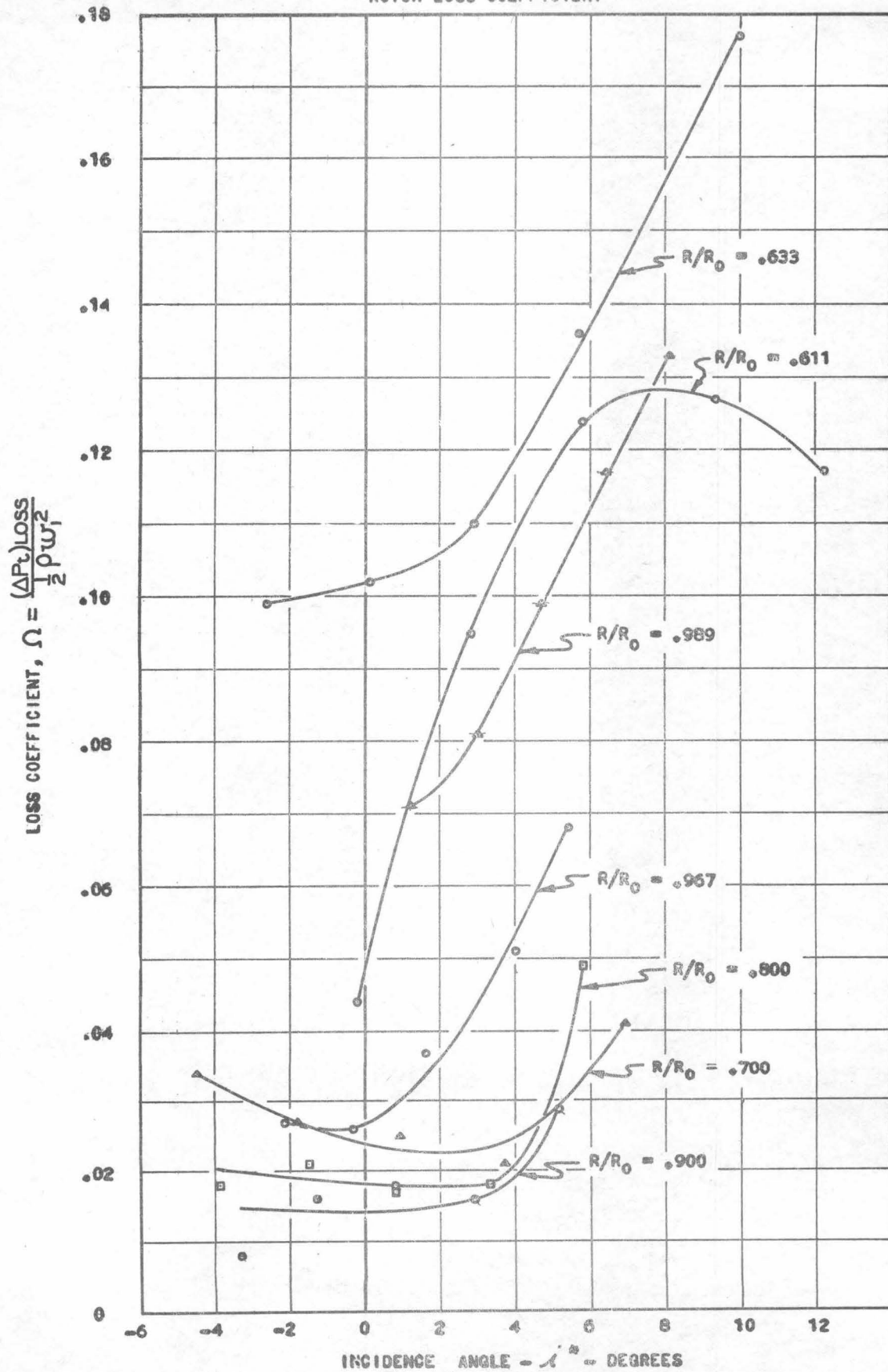


FIGURE 25

COMPARISON OF ROTOR LOSSES AT MID-SECTION WITH TWO-DIMENSIONAL CASCADE

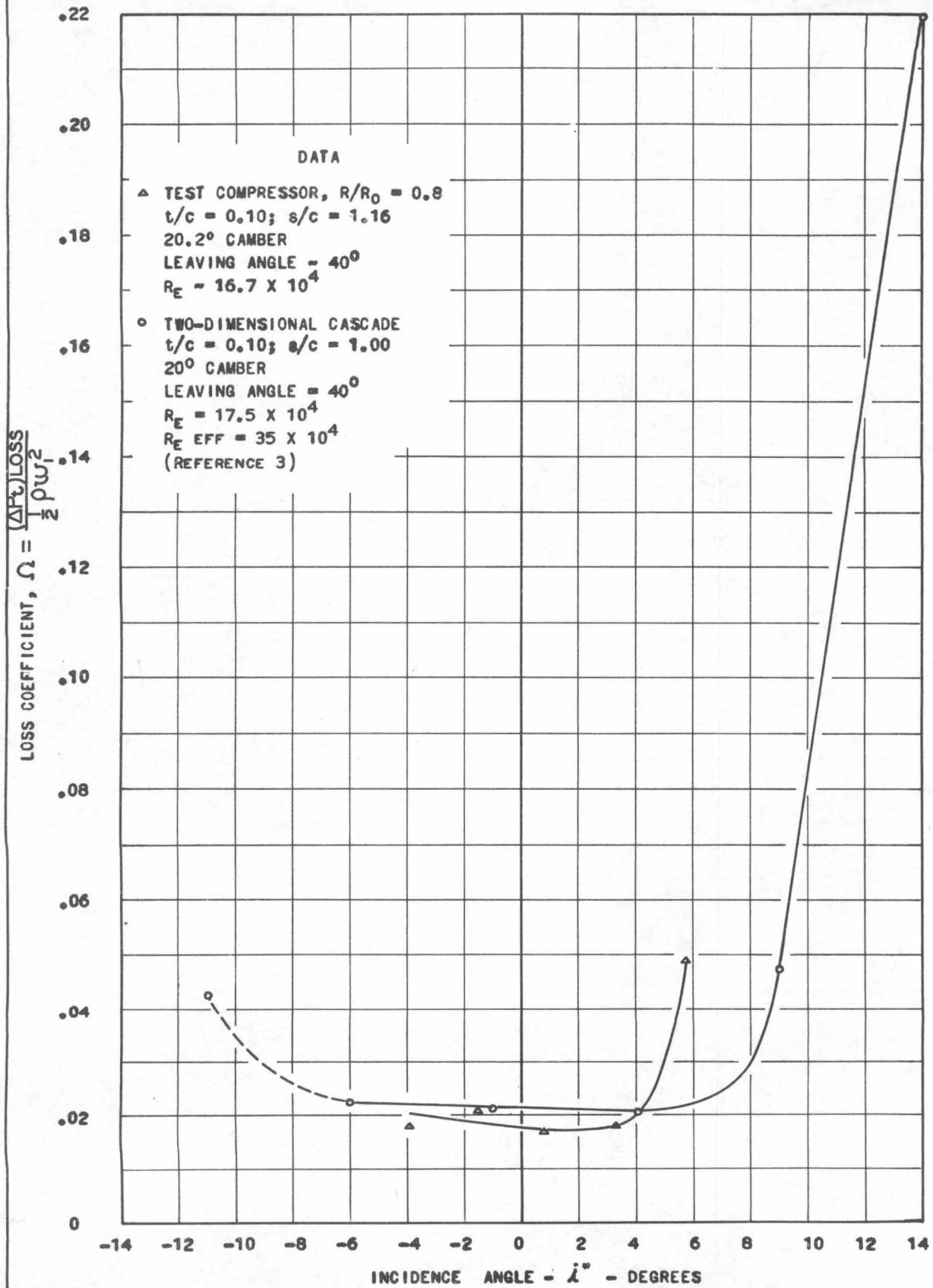


FIGURE 26

FIGURE 27

FREE VORTEX BLADING - ROTOR

ROTOR LOSS, $\bar{\Phi}_0 = 0.370$

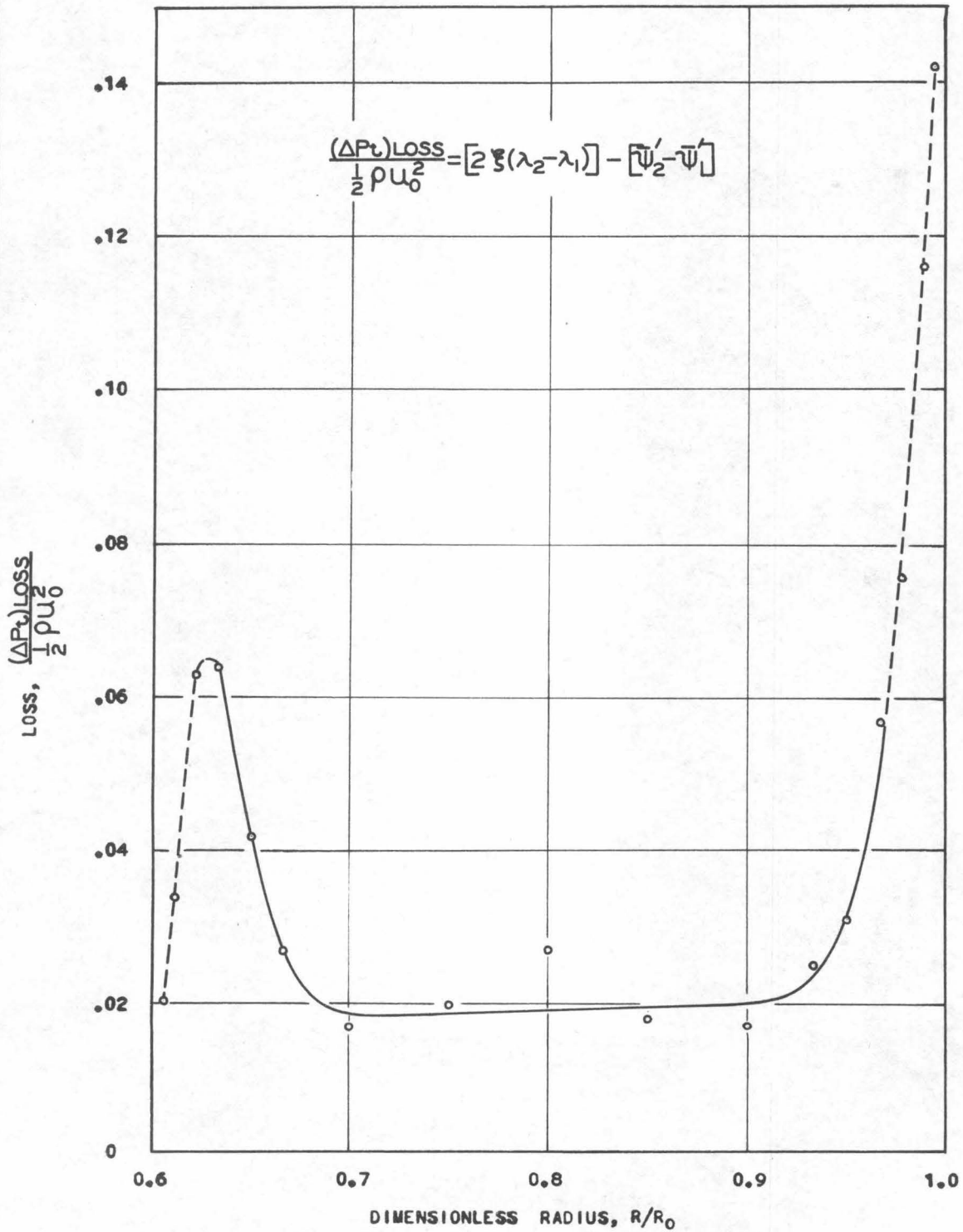


FIGURE 28

FREE VORTEX BLADING - ROTOR

ROTOR LOSS, $\bar{\phi}_0 = 0.400$

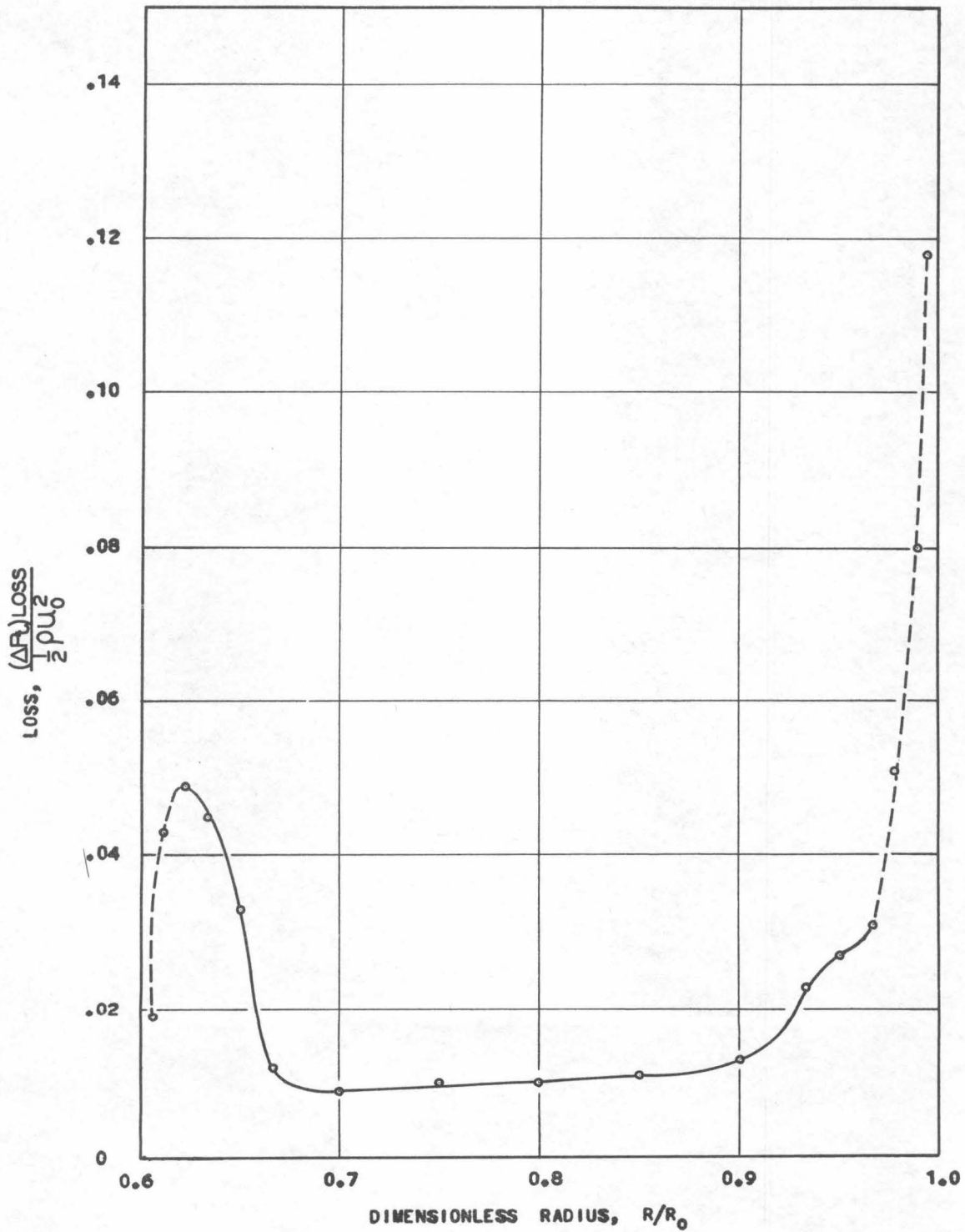


FIGURE 29
FREE VORTEX BLADING - ROTOR
ROTOR LOSS, $\bar{\Phi}_0 = 0.430$

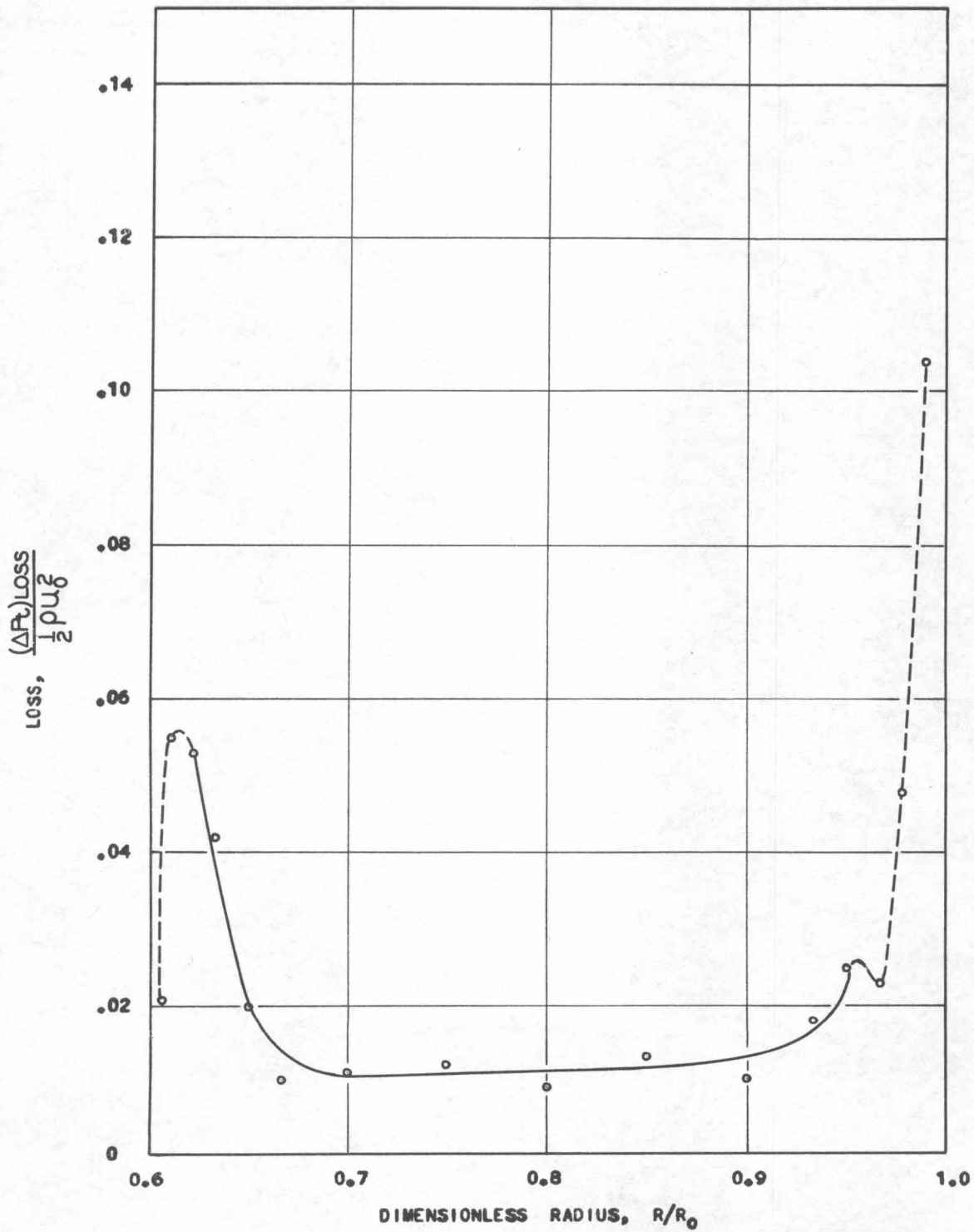


FIGURE 30

FREE VORTEX BLADING - ROTOR

ROTOR LOSS, $\bar{\Phi}_0 = 0.460$

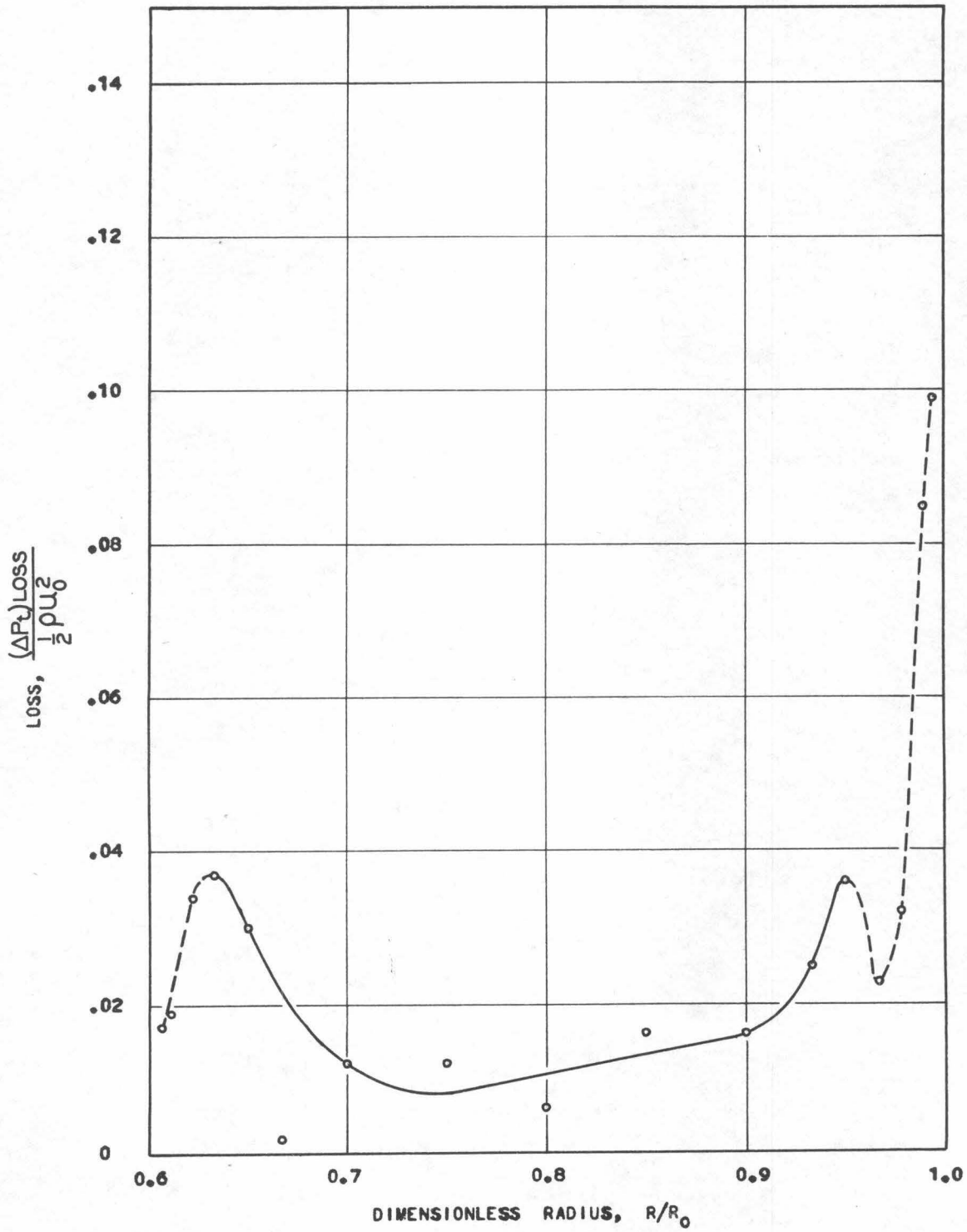
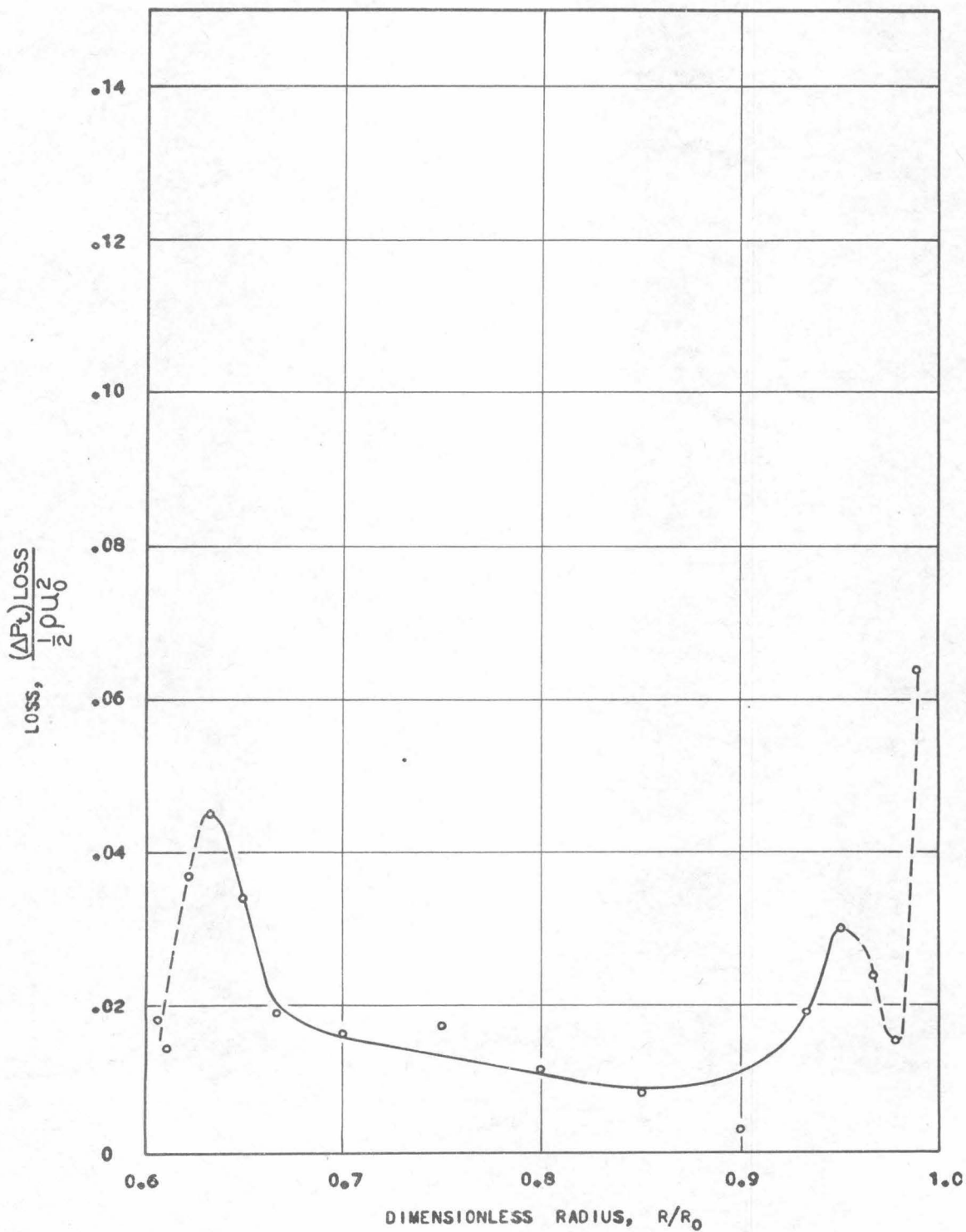


FIGURE 31

FREE VORTEX BLADING - ROTOR

ROTOR LOSS, $\Phi_0 = 0.490$



FREE VORTEX BLADING - ROTOR
BOUNDARY LAYER DATA BEHIND THE ROTOR

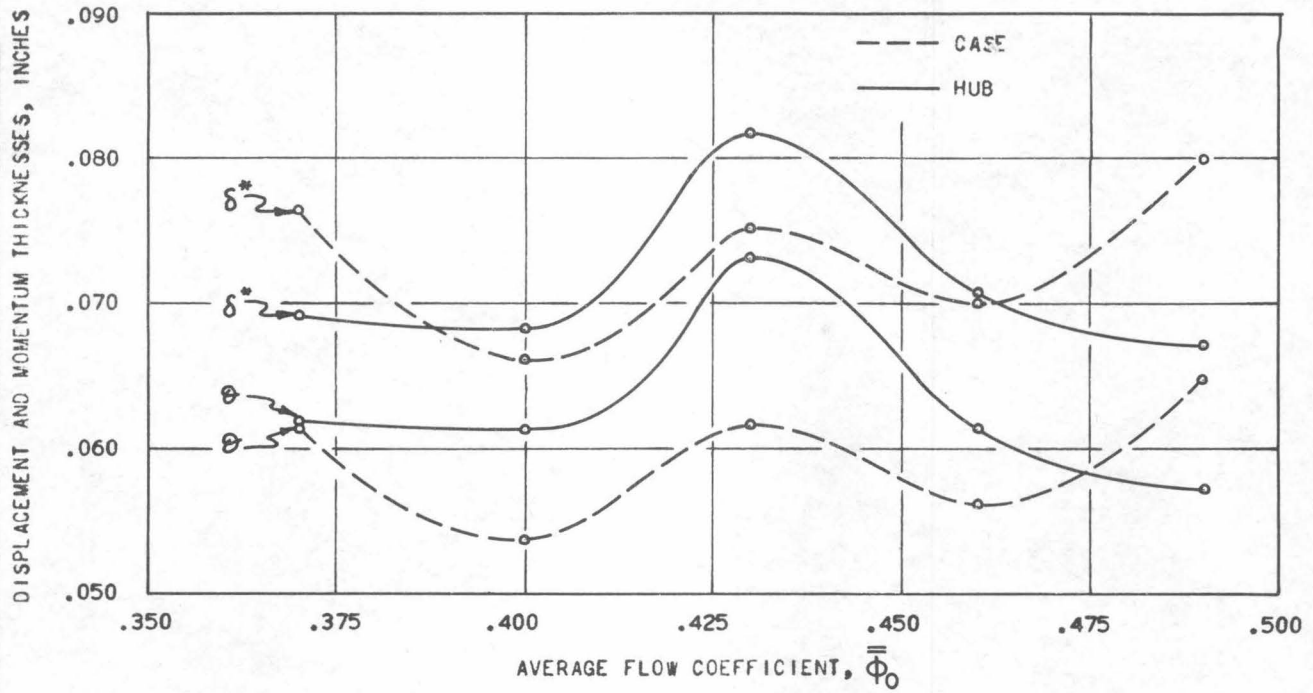


FIGURE 32A

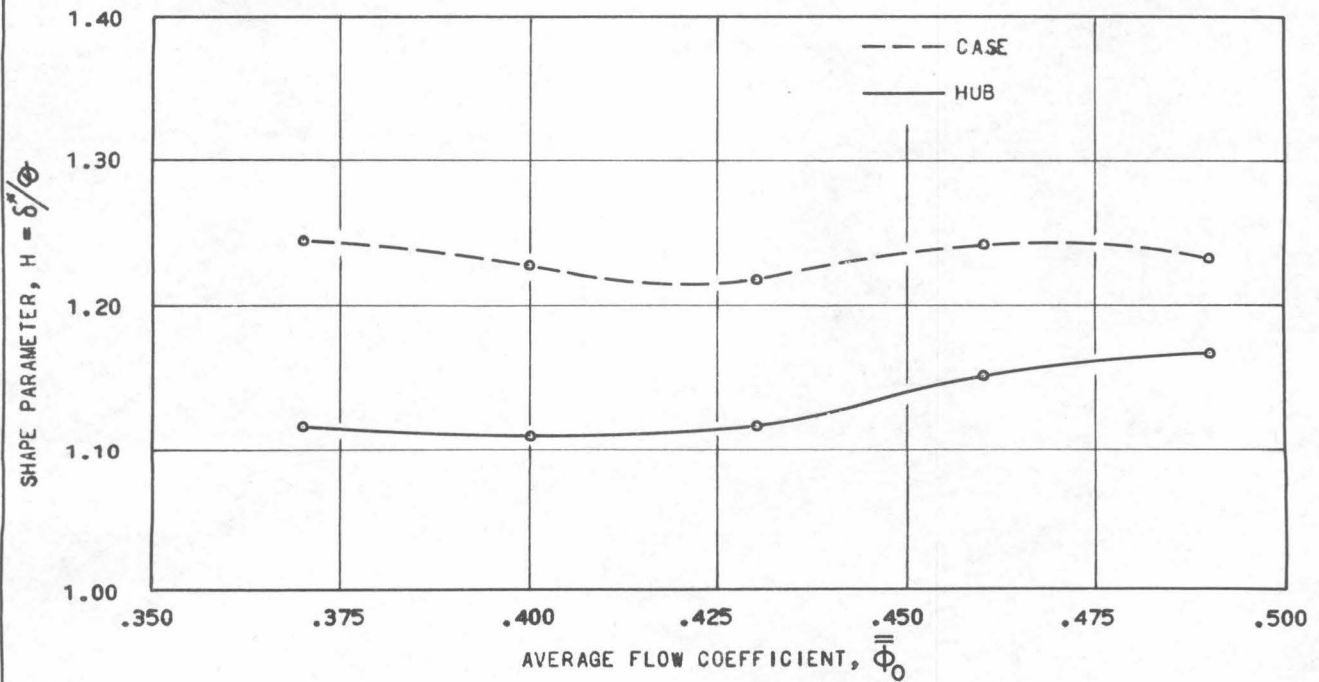


FIGURE 32B

FREE VORTEX BLADING - STATOR
BOUNDARY LAYER DATA BEHIND THE STATOR

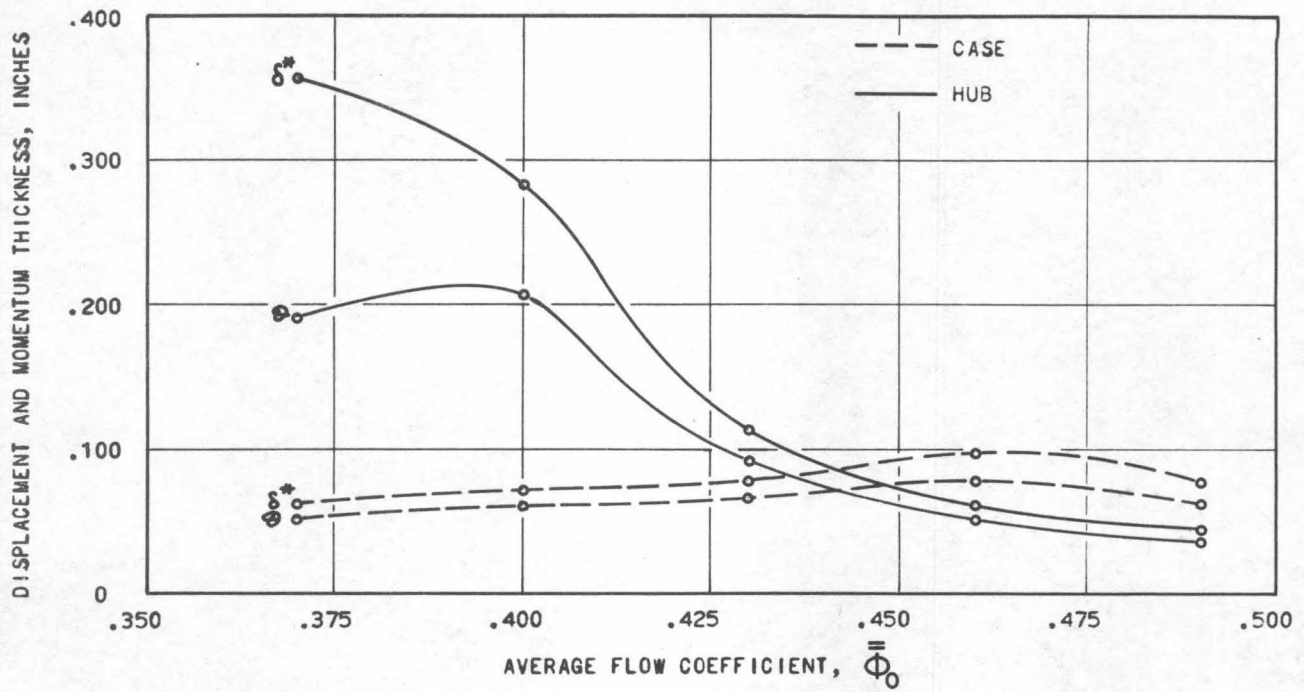


FIGURE 33a

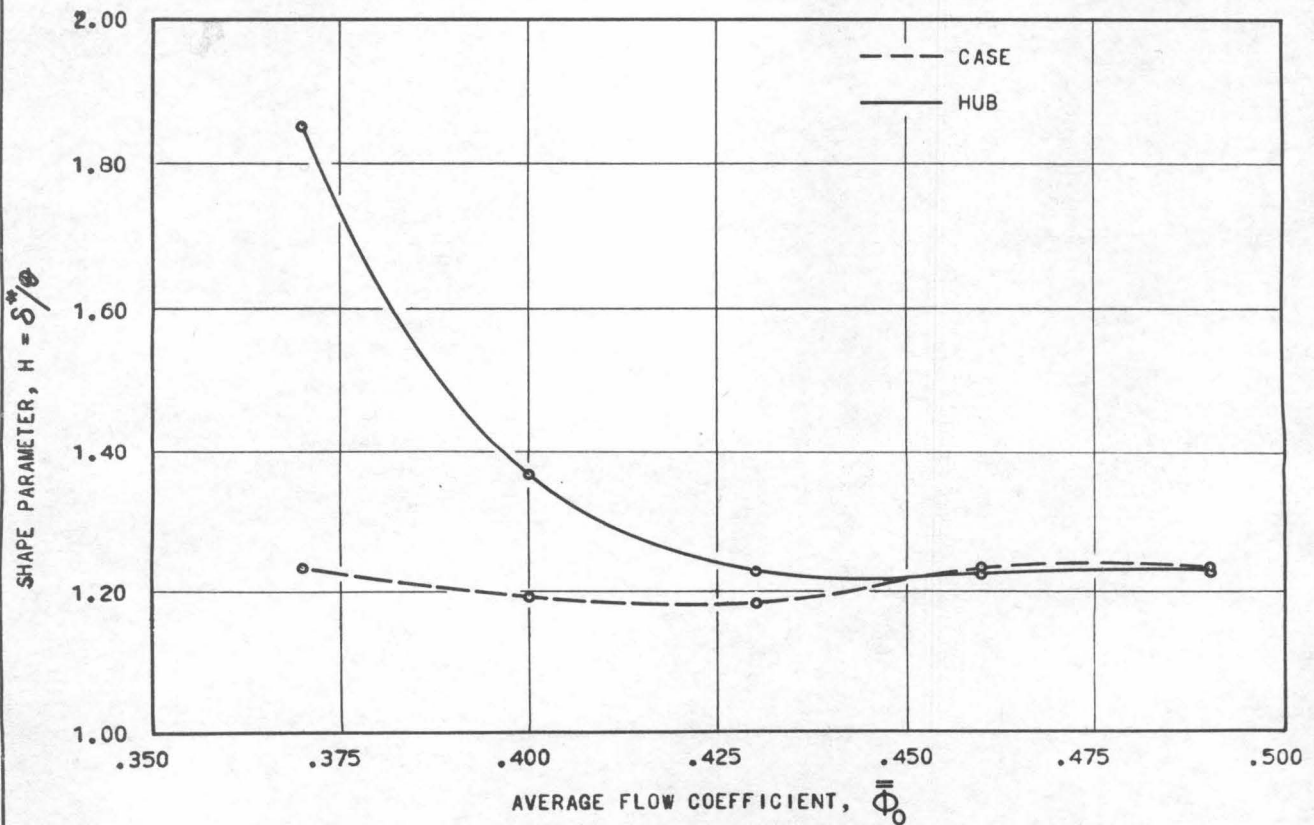


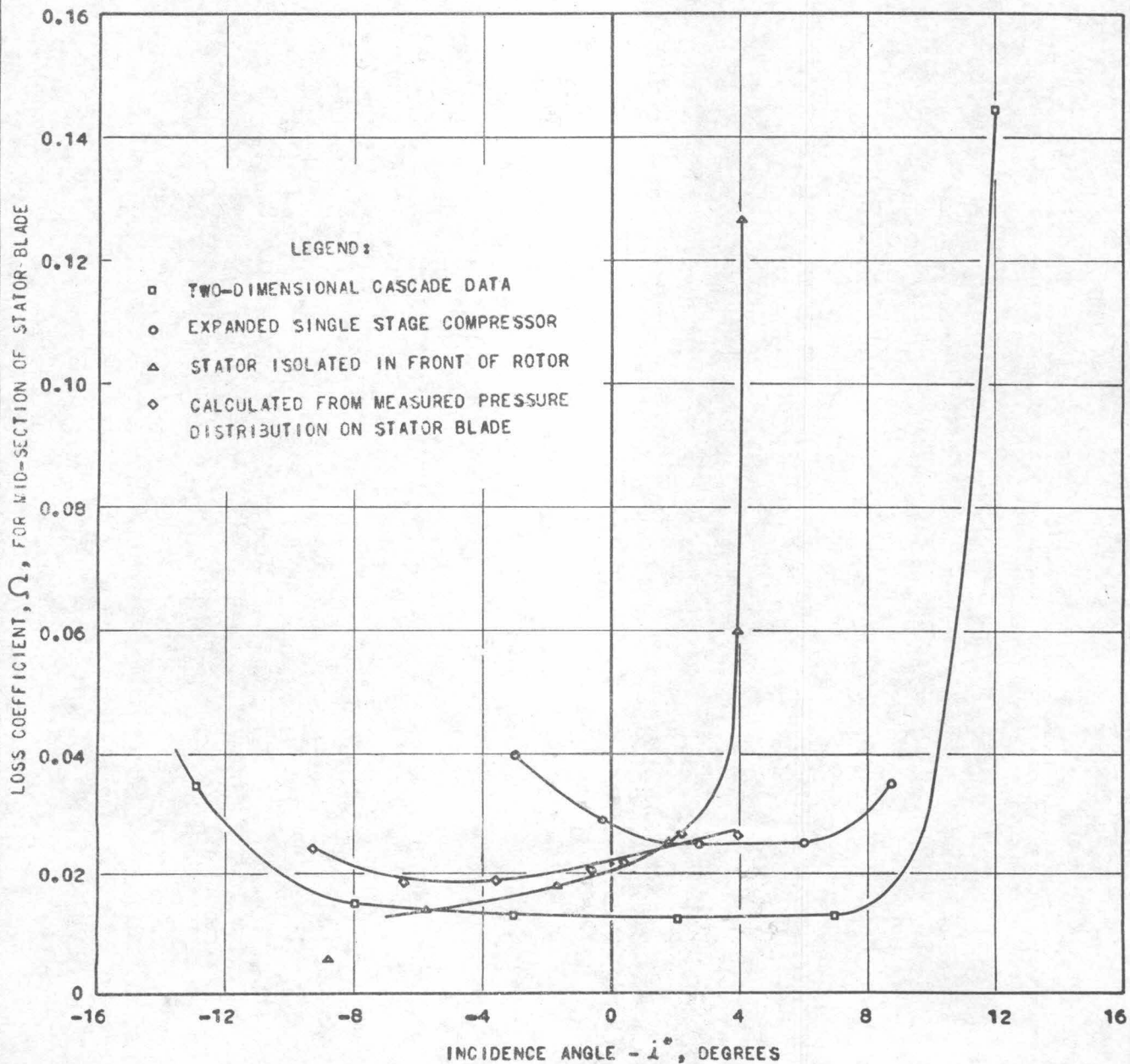
FIGURE 33b

FIGURE 34

COMPARISON OF STATOR LOSS AT MID-SECTION WITH TWO-DIMENSIONAL CASCADE
FREE VORTEX BLADING

TWO-DIMENSIONAL CASCADE:
 $t/c = 0.075$; $s/c = 1.0$
 CAMBER = 30°
 LEAVING ANGLE = 20°
 $R_E = 17.5 \times 10^4$
 (REFERENCE 3)

TEST COMPRESSOR, $R/R_0 = 0.8$:
 $t/c = 0.1$; $s/c = 1.088$
 CAMBER = 30°
 LEAVING ANGLE = 23°
 $12.6 \times 10^4 < R_E < 13.9 \times 10^4$



FREE VORTEX BLADING - STATOR

STATOR LOSS COEFFICIENT

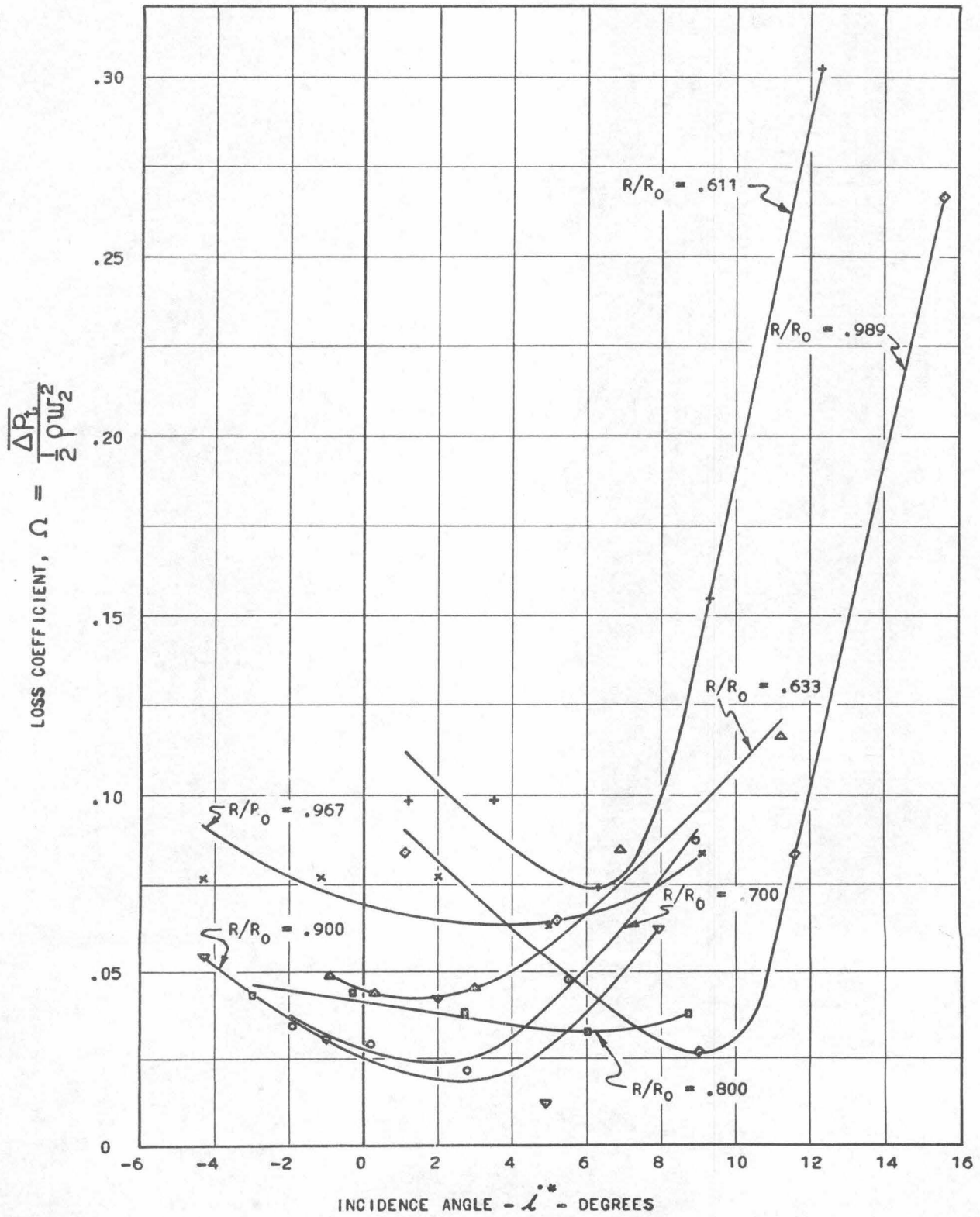


FIGURE 35

FREE VORTEX BLADING - STATOR
 TOTAL PRESSURE LOSS COEFFICIENT

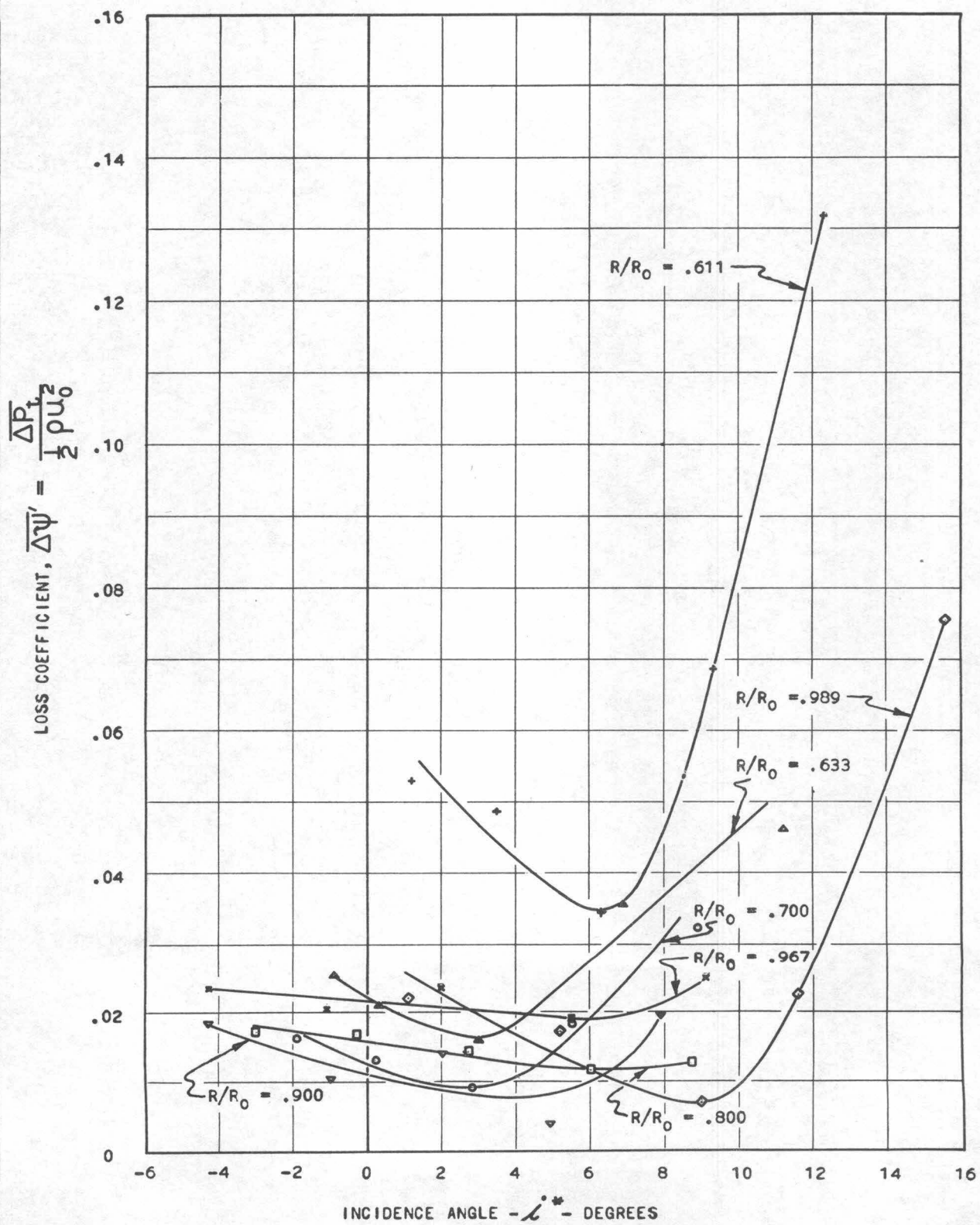


FIGURE 36

FIGURE 37

FREE VORTEX BLADING - STATOR
STATOR LOSS

$\bar{\Phi}_0 = .370$

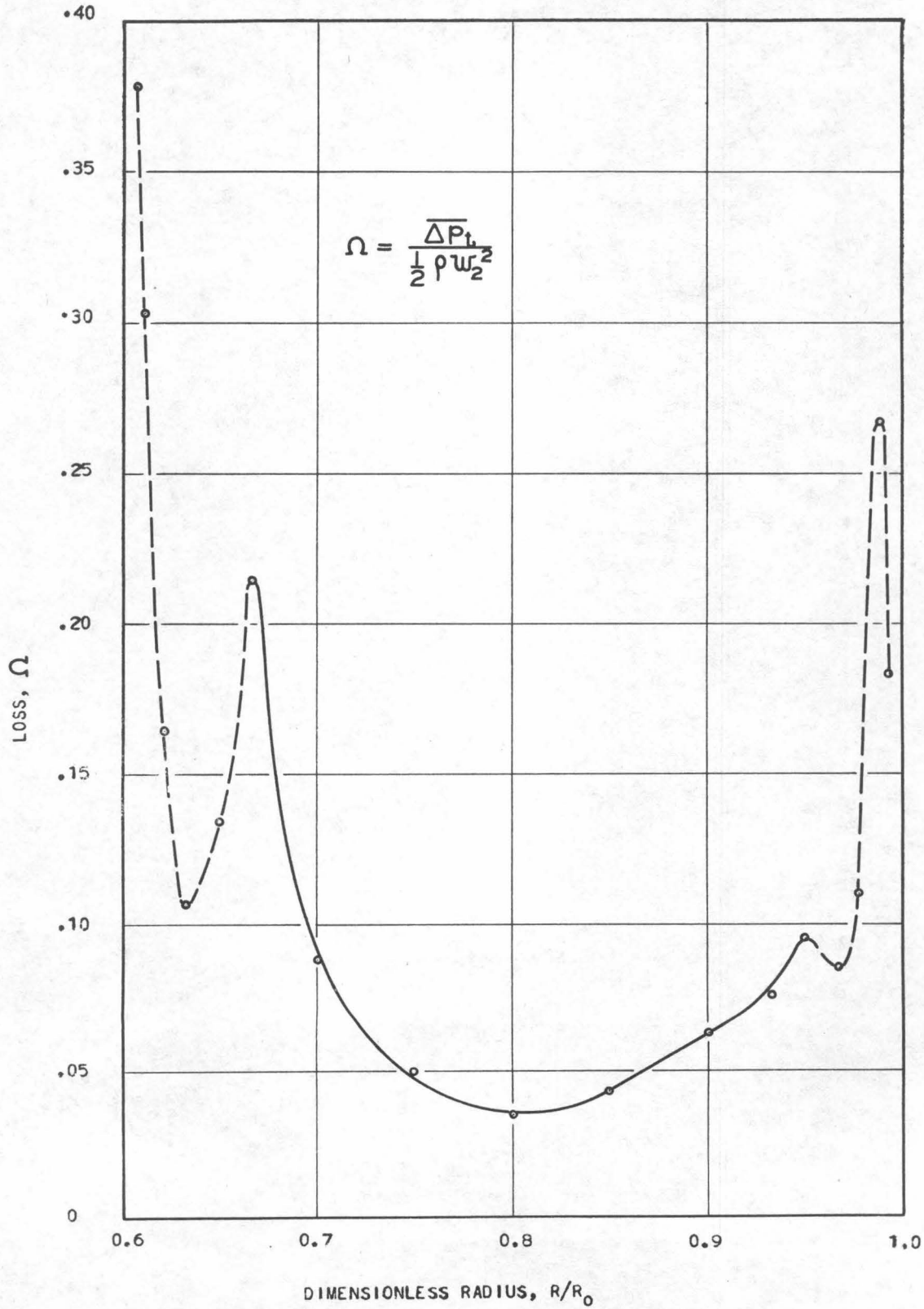


FIGURE 38
FREE VORTEX BLADING - STATOR
STATOR LOSS

$\bar{\Phi}_0 = .400$

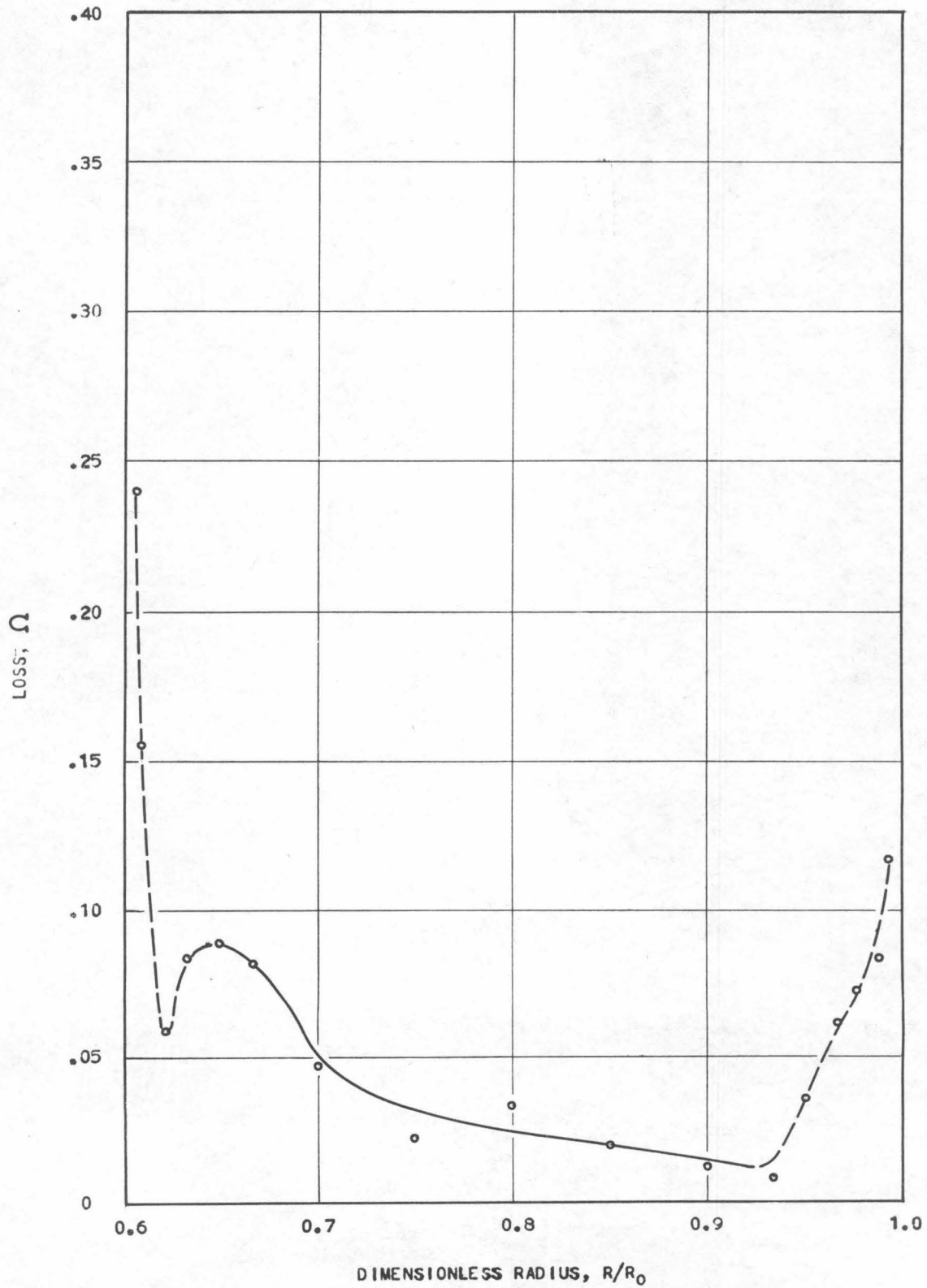


FIGURE 39

FREE VORTEX BLADING - STATOR

STATOR LOSS

$\bar{\Phi}_0 = .430$

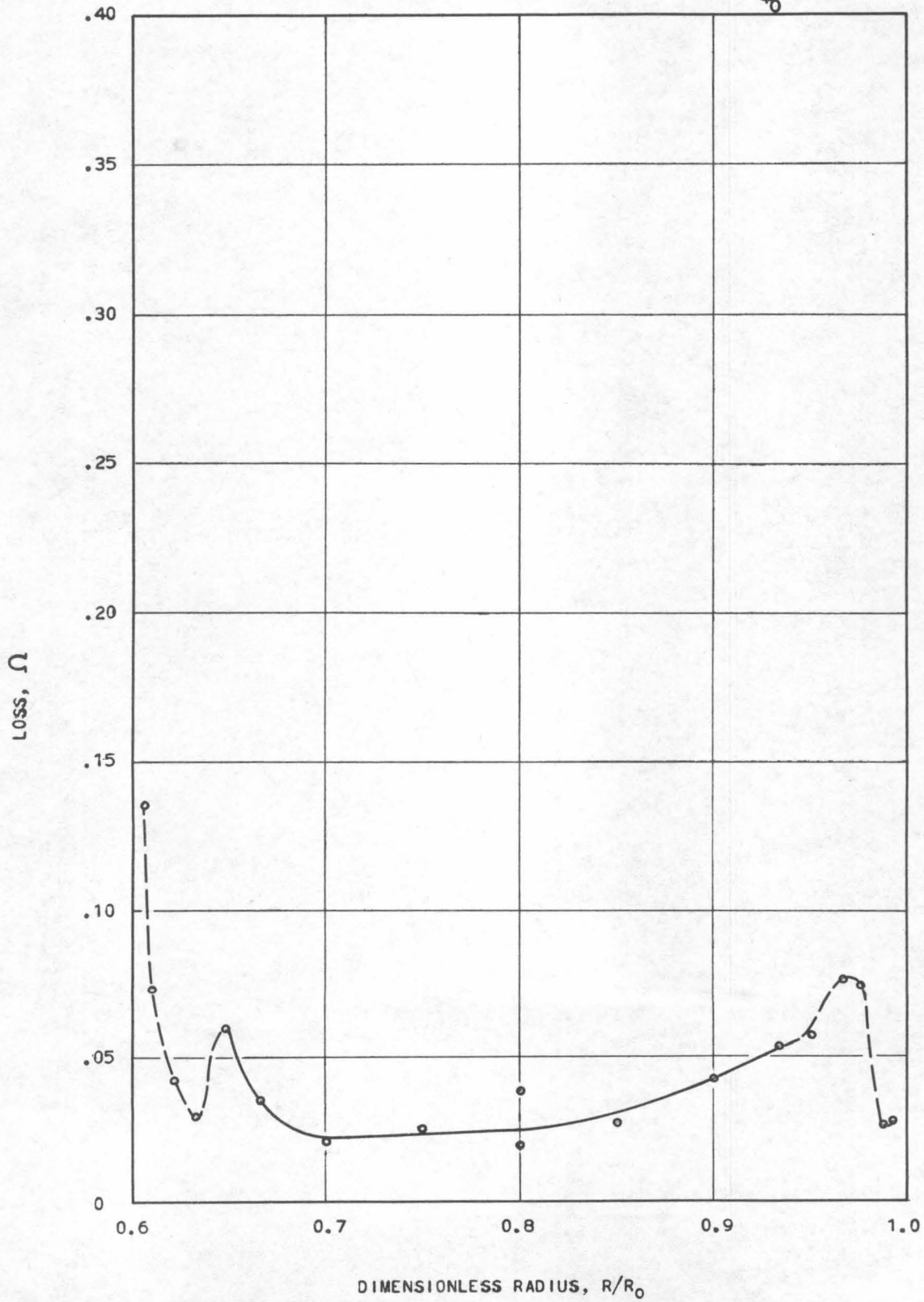


FIGURE 40

FREE VORTEX BLADING - STATOR

STATOR LOSS

$$\bar{\Phi}_0 = .460$$

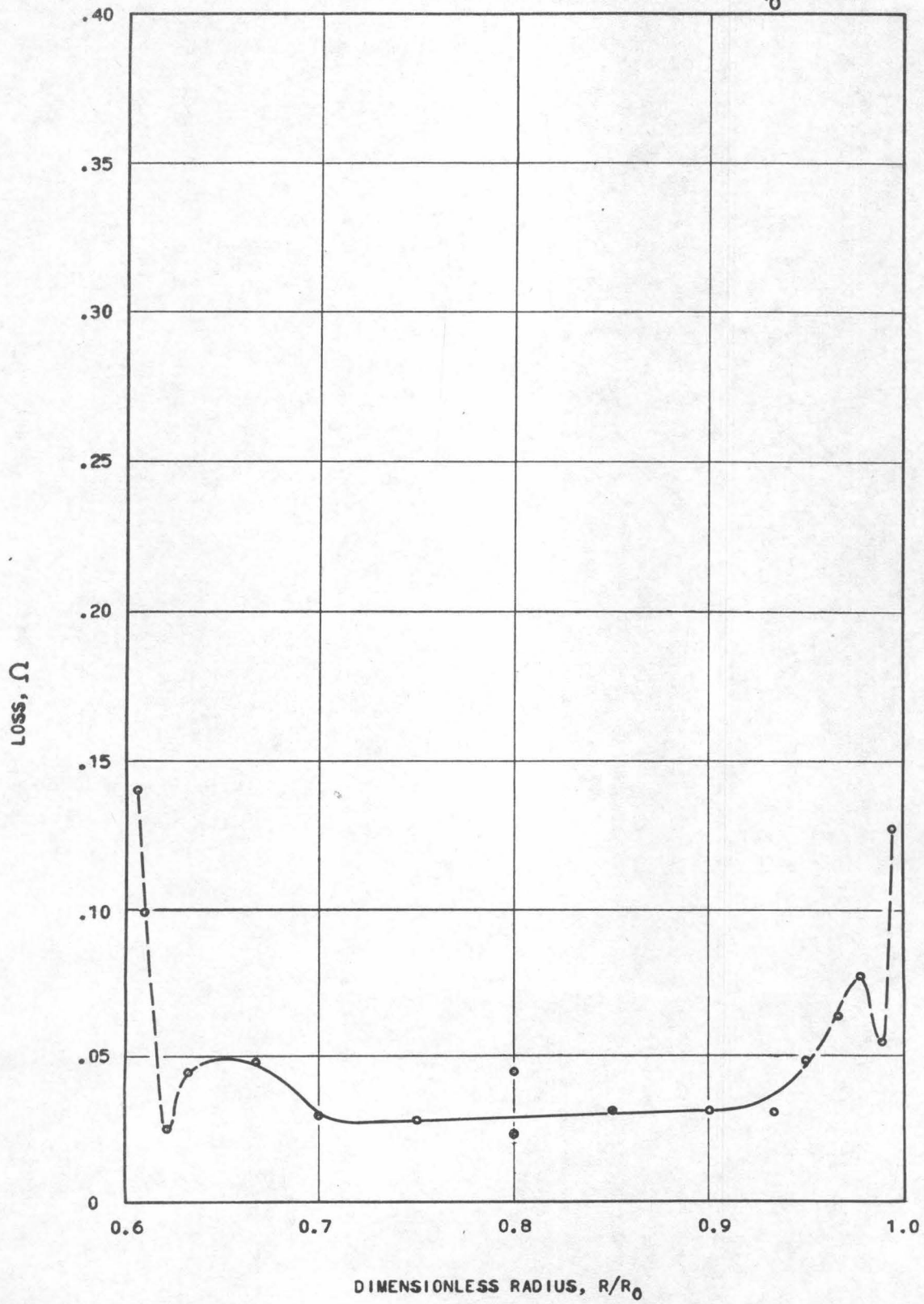


FIGURE 41

FREE VORTEX BLADING - STATOR

STATOR LOSS

$\bar{\Phi}_0 = .490$

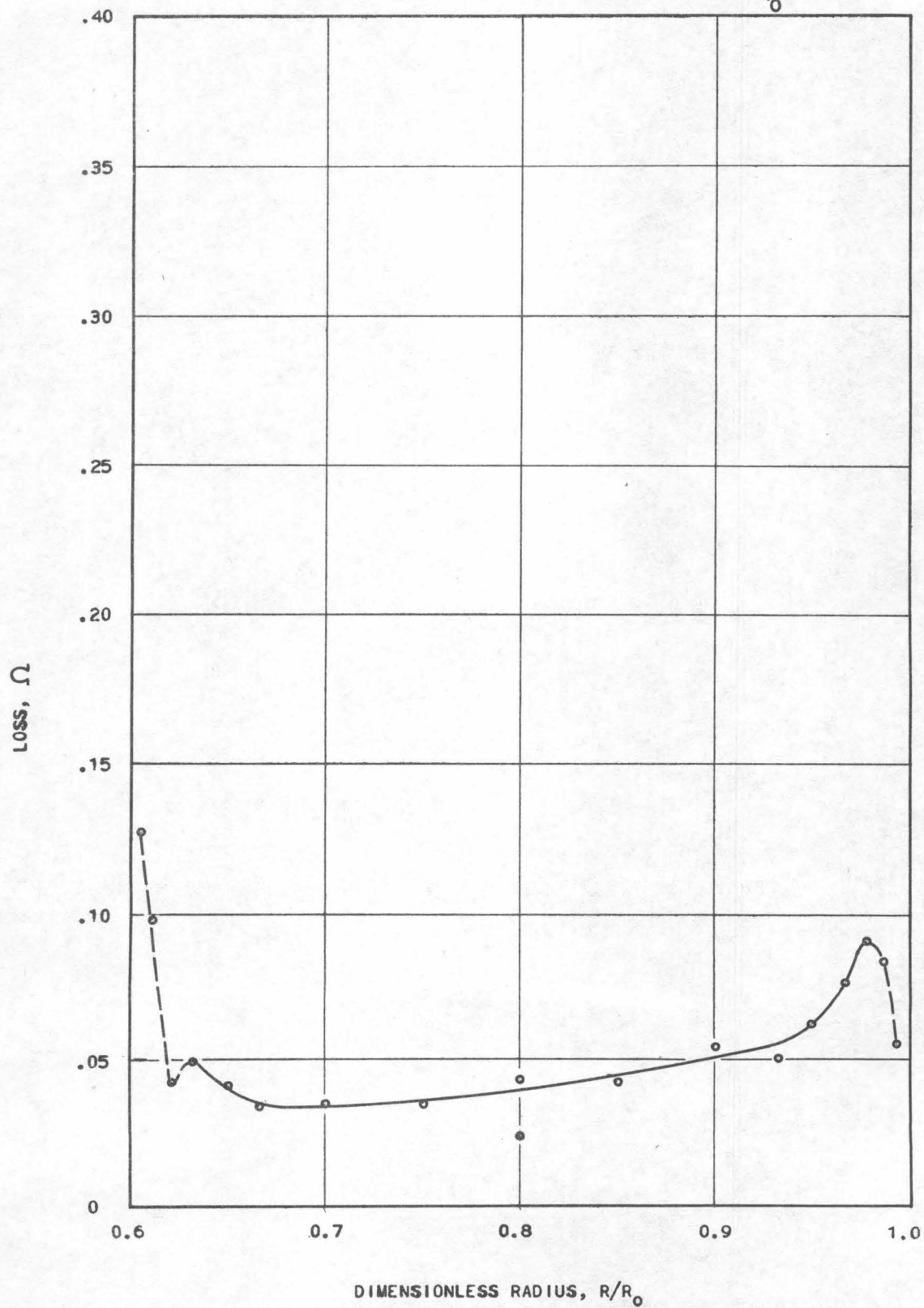


FIGURE 42
FREE VORTEX BLADING - STATOR
INCIDENCE ANGLES

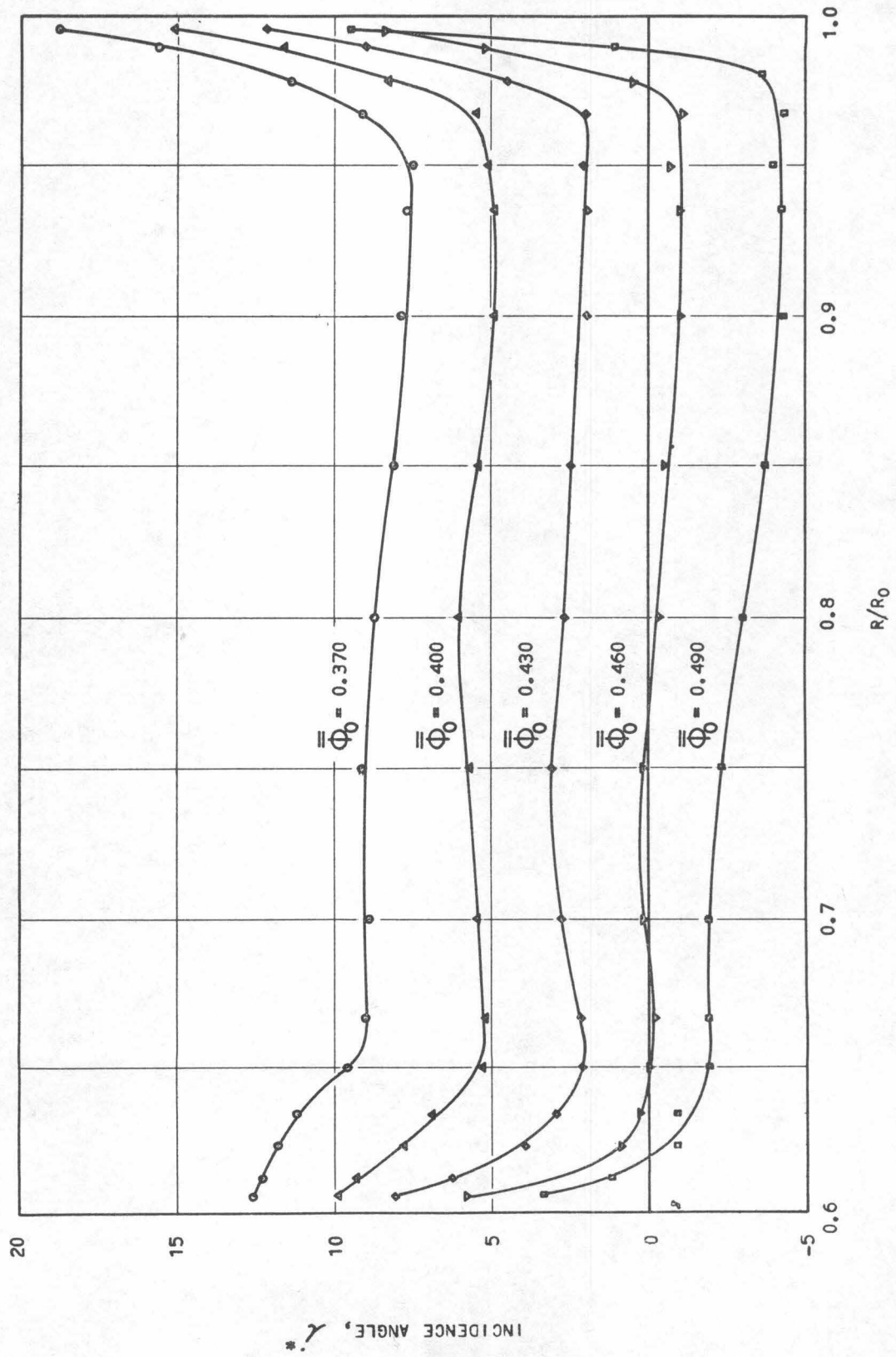
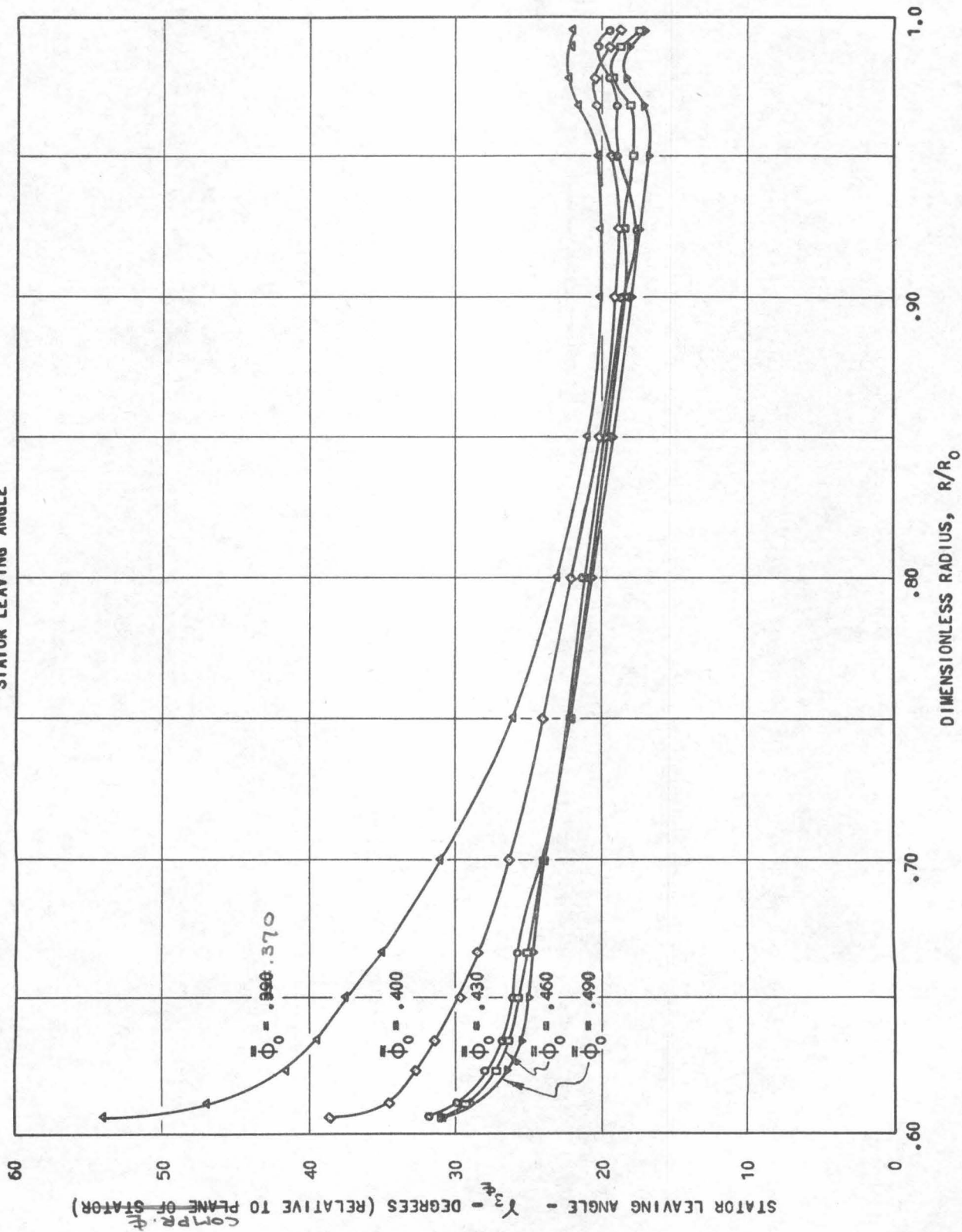


FIGURE 43
 FLOW CHARACTERISTICS BEHIND STATOR, FREE VORTEX BLADING
 STATOR LEAVING ANGLE



FLOW CHARACTERISTICS BEHIND STATOR, FREE VORTEX BLADING

STATOR LEAVING ANGLE

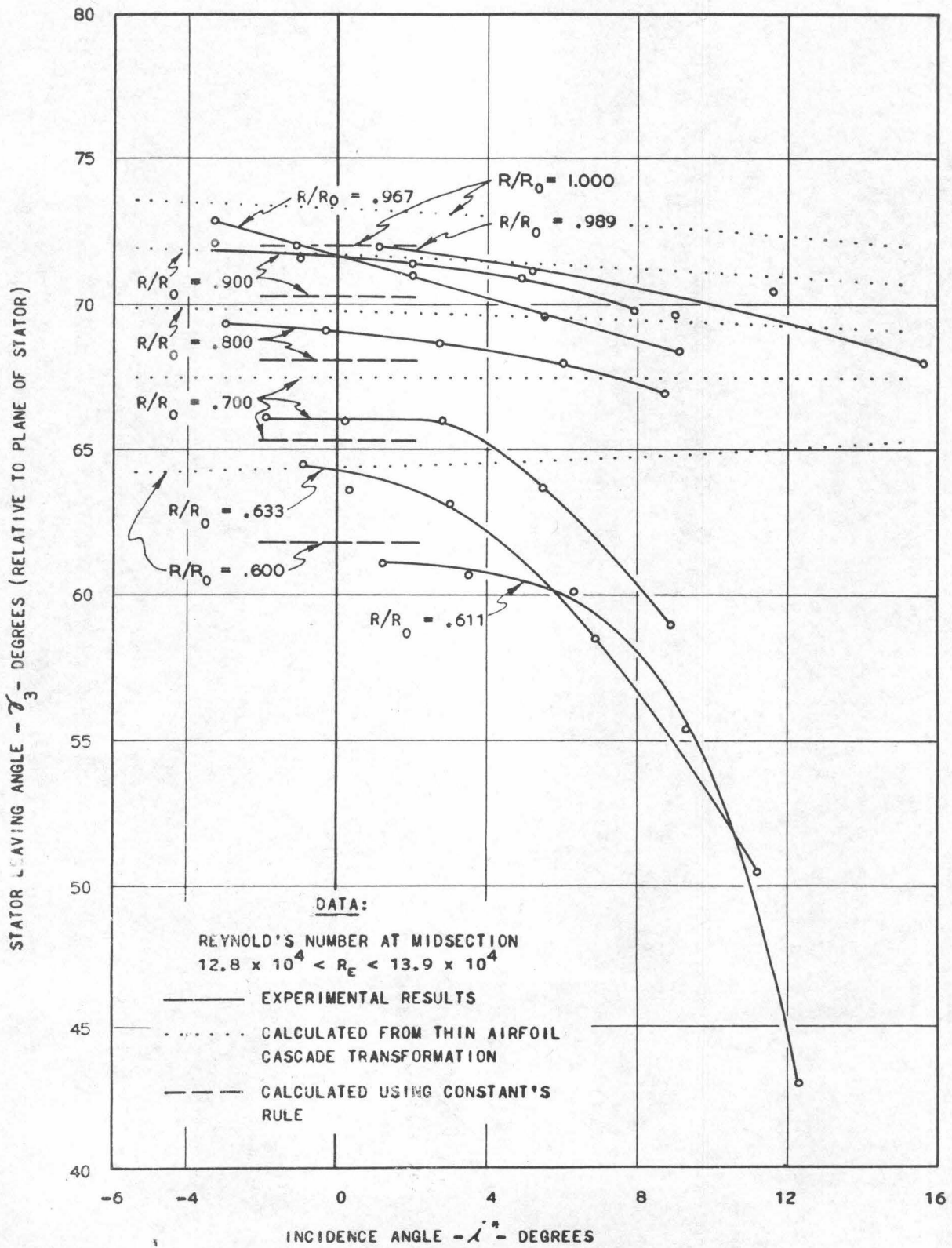


FIGURE 44

FIGURE 45

FREE VORTEX BLADING - STATOR
AIR TURNING ANGLE THRU STATOR

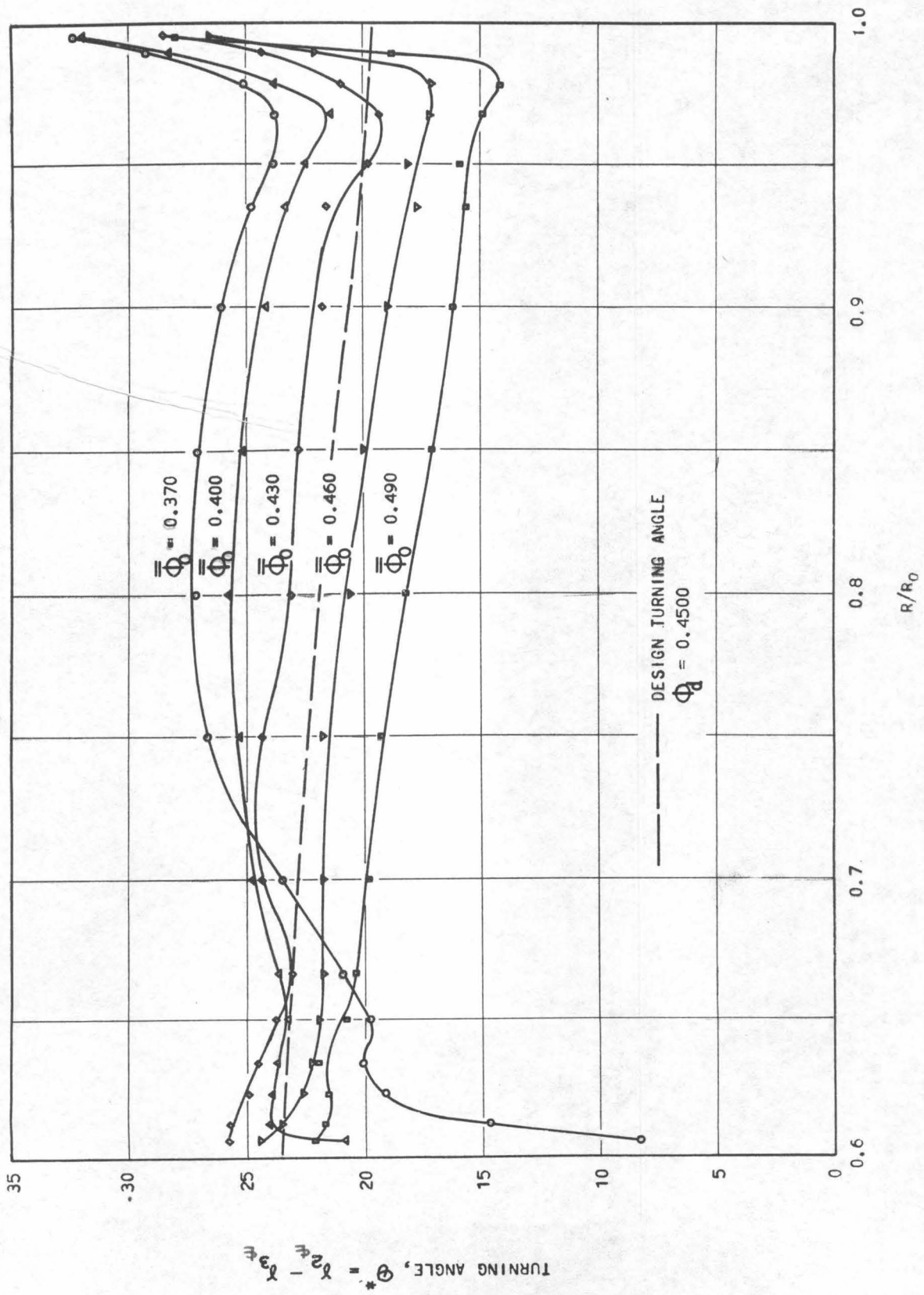


FIGURE 46

FLOW CHARACTERISTICS BEHIND STATOR, FREE VORTEX BLADING
 DIMENSIONLESS AXIAL VELOCITY BEHIND STATOR

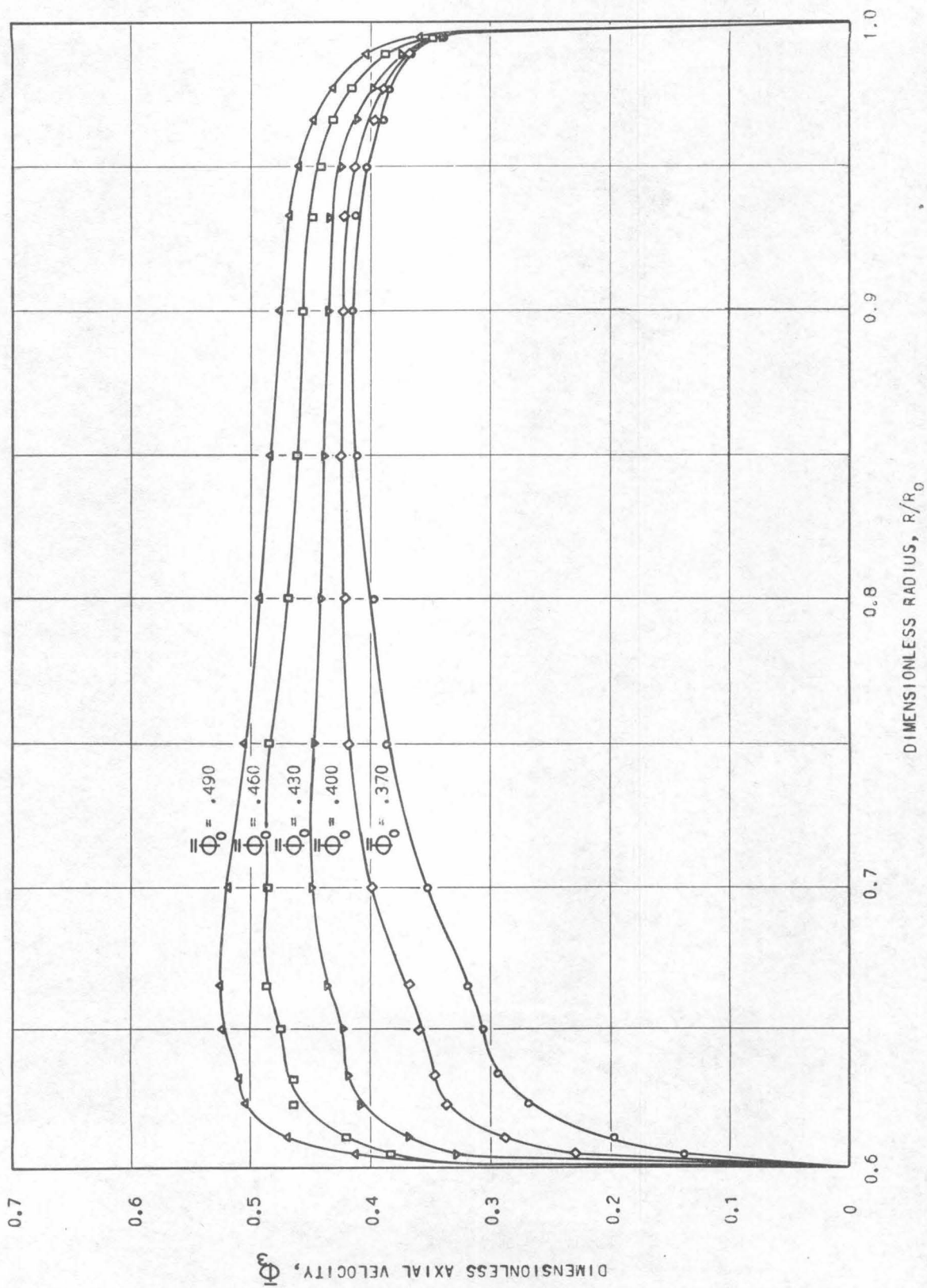


FIGURE 47
 FLOW CHARACTERISTICS BEHIND STATOR, FREE VORTEX BLADING
 COMPARISON OF MEASURED AND CALCULATED AXIAL VELOCITY BEHIND STATOR

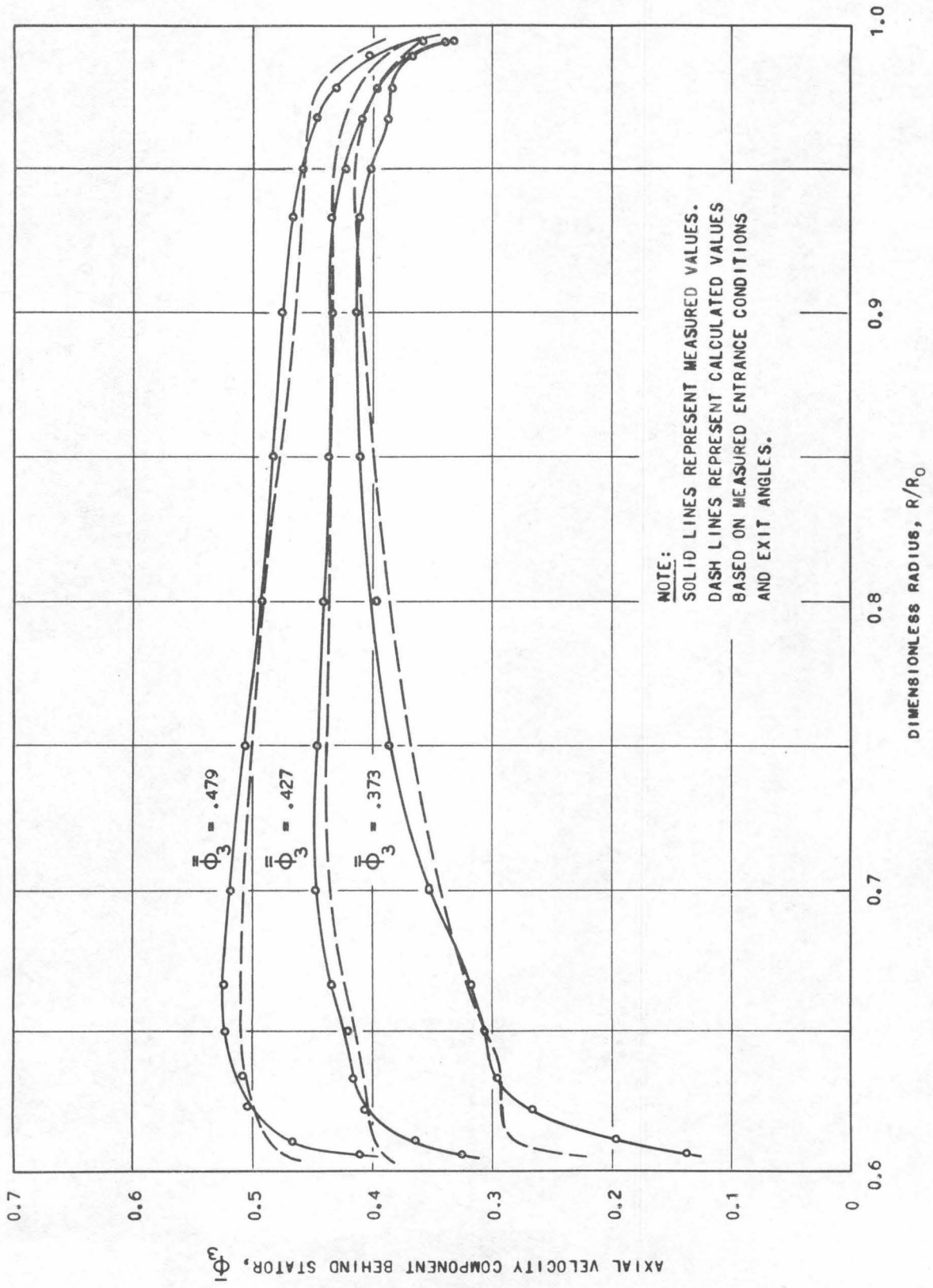


FIGURE 48

FLOW CHARACTERISTICS BEHIND STATOR, FREE VORTEX BLADING

AVERAGE TOTAL PRESSURE BEHIND STATOR

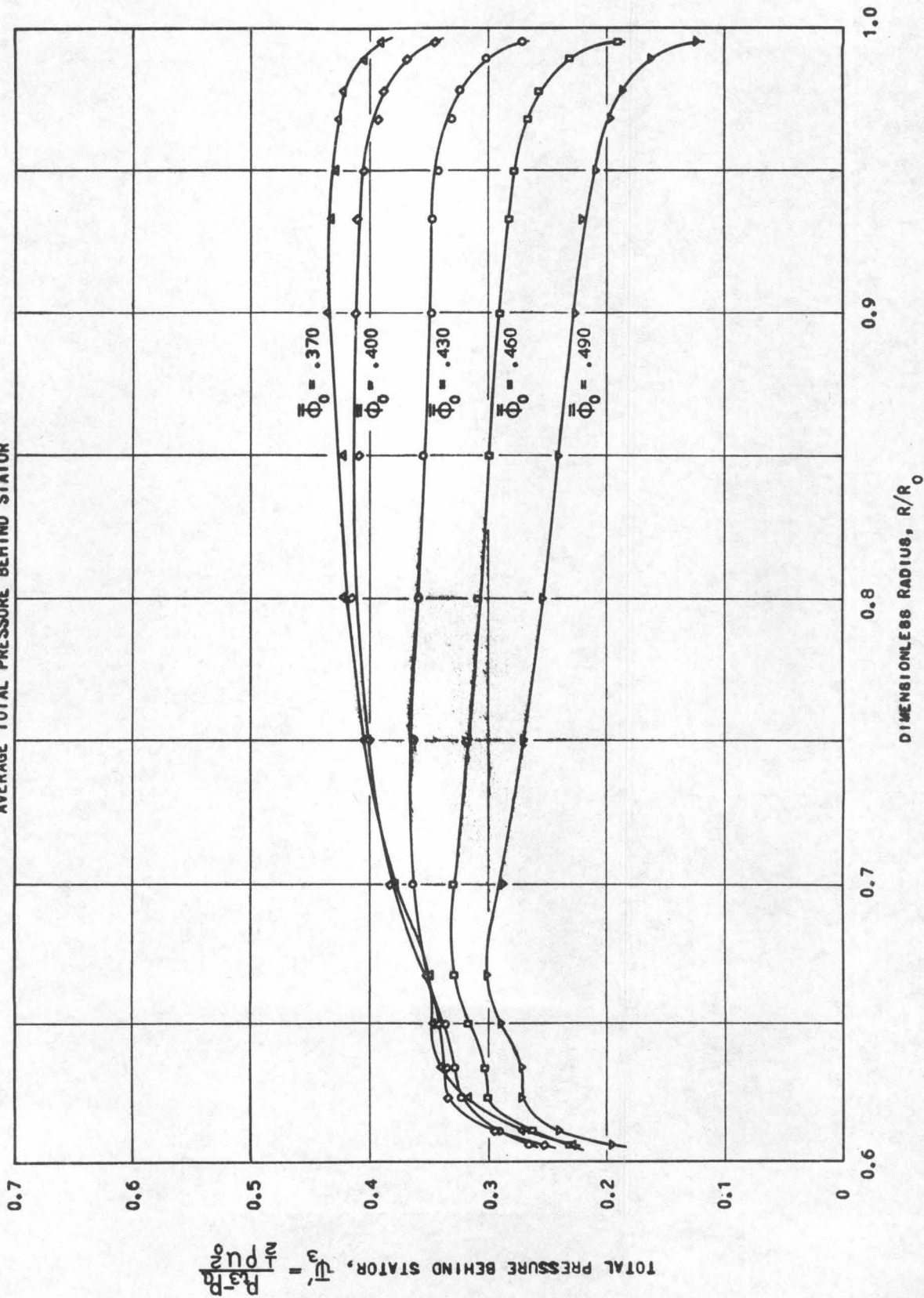


FIGURE 49

OVERALL PERFORMANCE CURVES, FREE VORTEX BLADING
EXPANDED SINGLE STAGE 1100 RPM

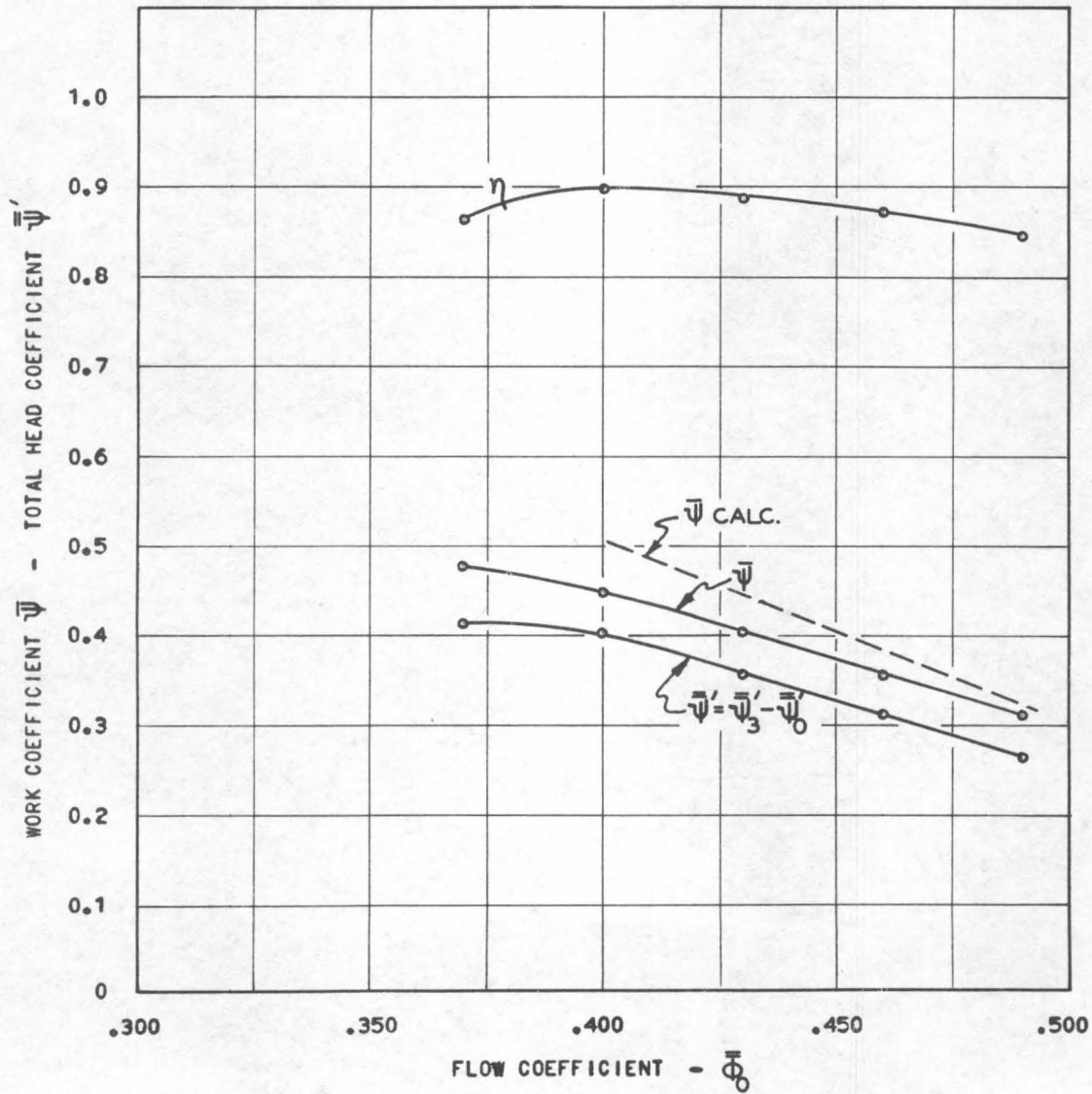


FIGURE 50
 EXPANDED SINGLE STAGE, FREE VORTEX BLADING 1100 RPM
 AVERAGE TOTAL PRESSURE

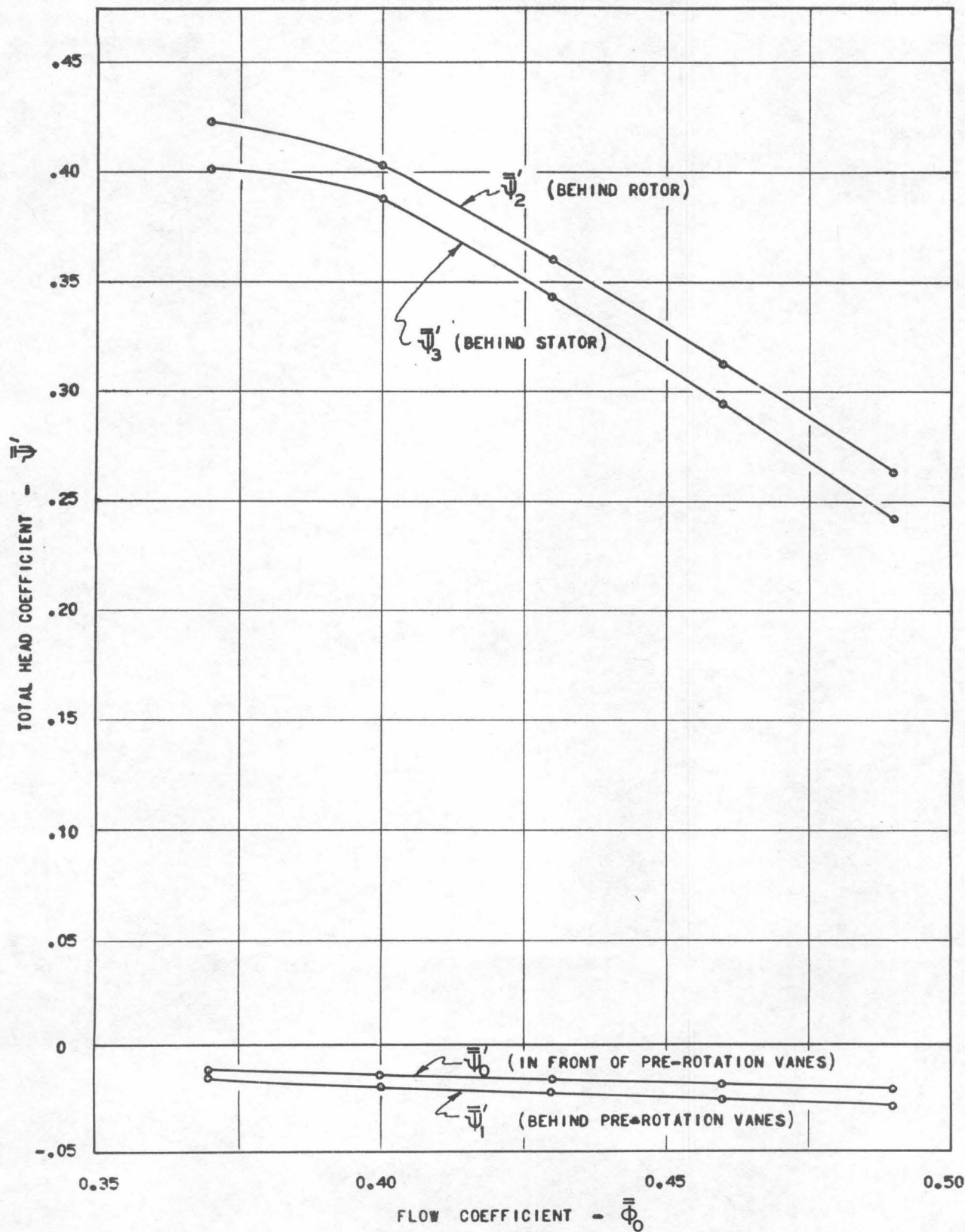
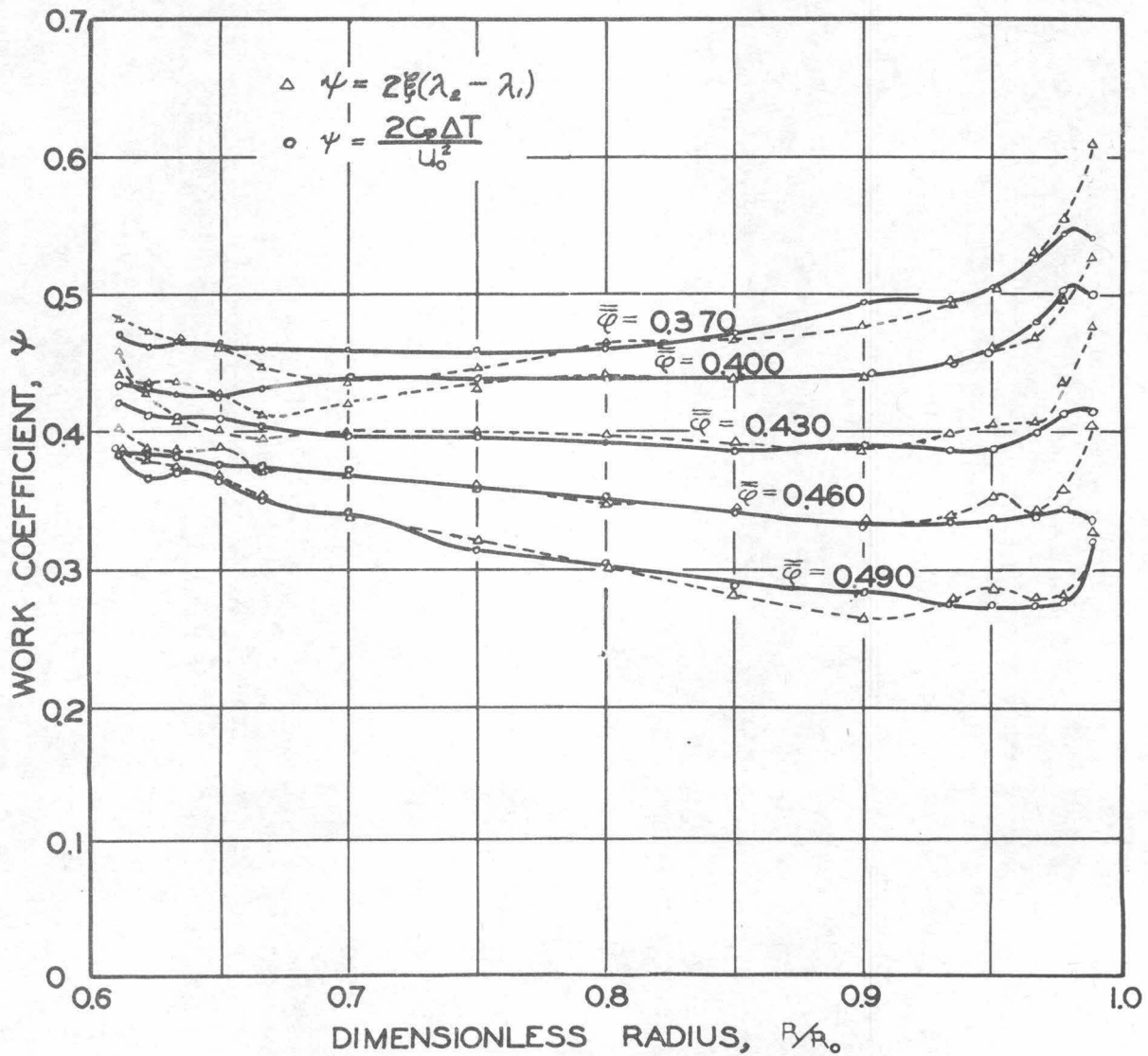
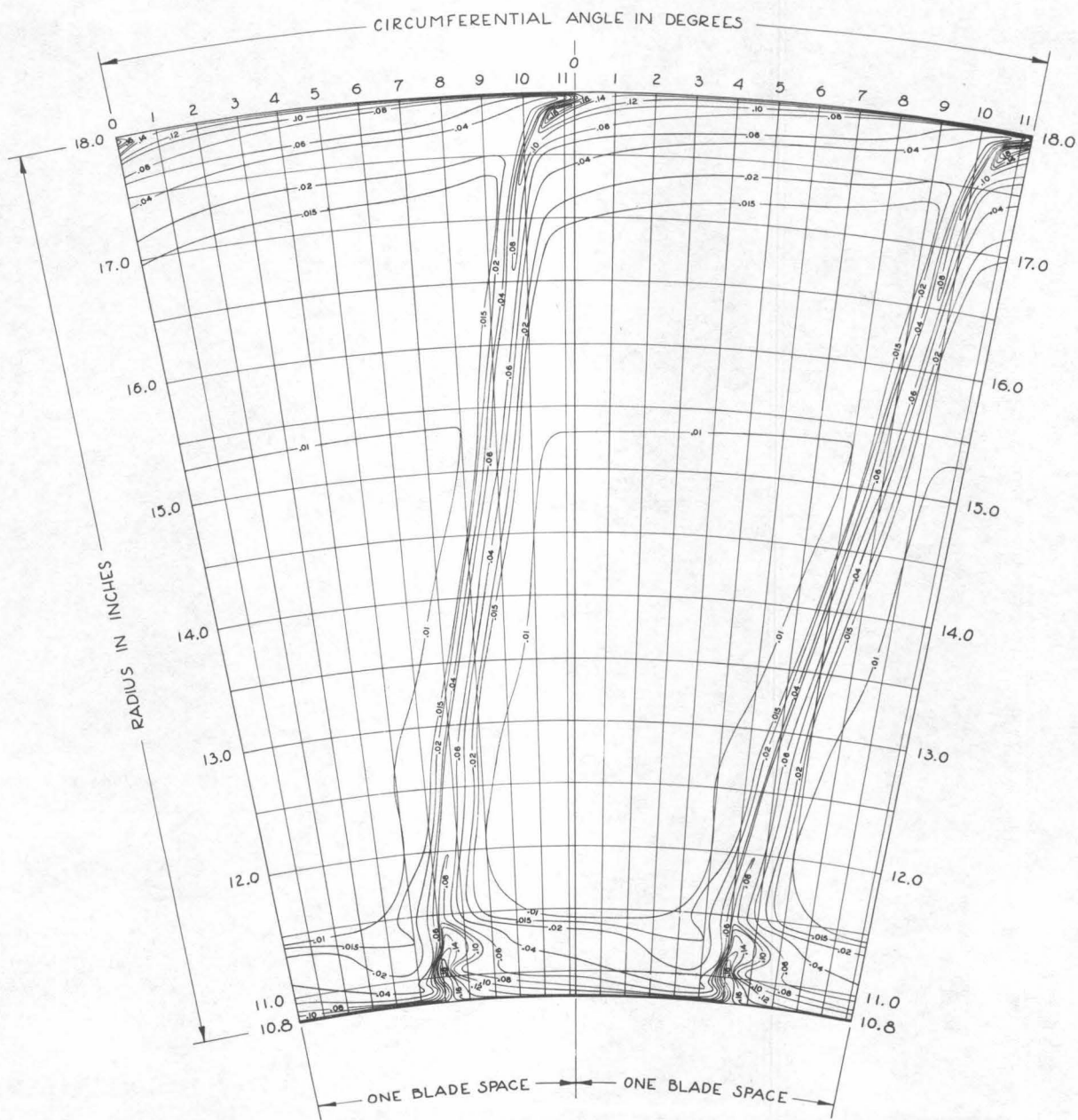


FIG. 52

FREE VORTEX BLADING

COMPARISON OF TWO METHODS FOR
DETERMINING RATE OF WORK INPUT
TO ROTOR

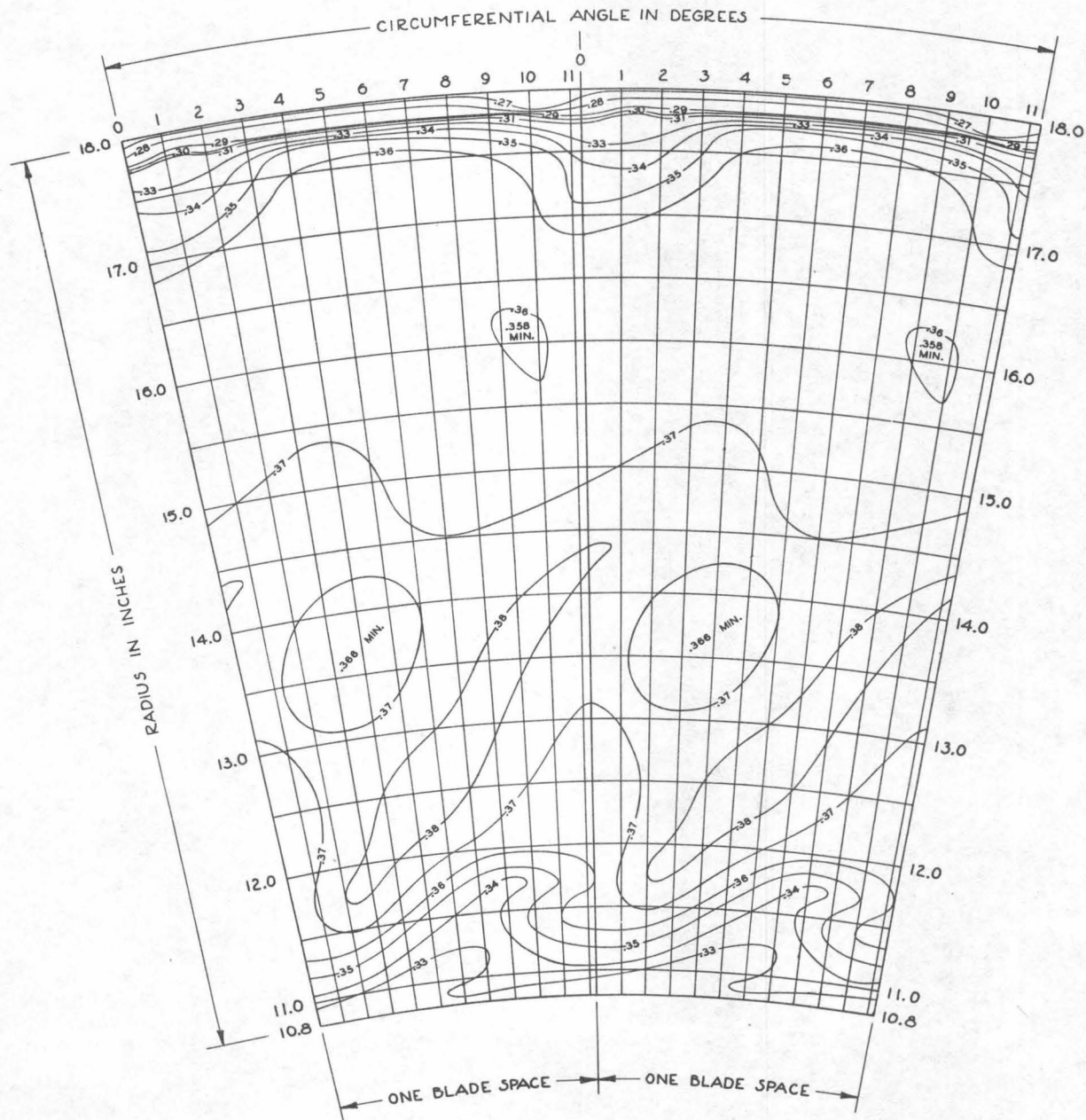




NOTES:

- A) CONTOURS ARE LINES OF $\psi' = \text{CONSTANT}$ WHERE $\psi' = \frac{R - R_0}{\frac{1}{2} \rho U_0^2}$
- B) THE ANGLE $11\frac{1}{4}^\circ$ IS EQUIVALENT TO ONE STATOR BLADE PITCH (32 BLADES). PATTERNS REPEAT AROUND COMPLETE ANNULUS.
- C) FLOW RATE: $\dot{\Phi} = 0.430$

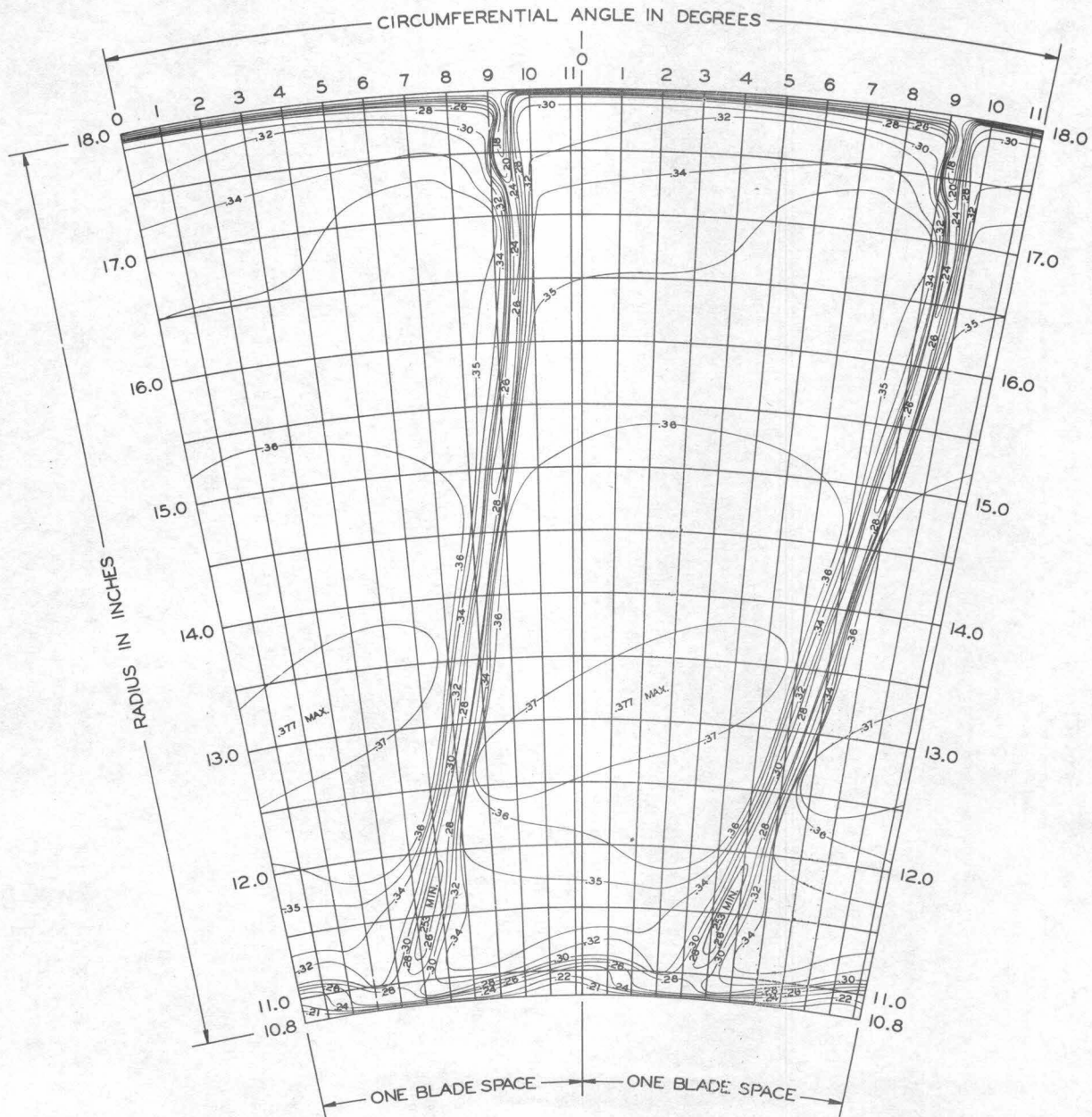
FIG. 53 TOTAL PRESSURE CONTOURS DOWNSTREAM OF ENTRANCE VANES



NOTES:

- A) CONTOURS ARE LINES OF $\psi' = \text{CONSTANT}$ WHERE $\psi' = \frac{P_1 - P_2}{\frac{1}{2} \rho U_1^2}$
- B) THE ANGLE $11\frac{1}{2}^\circ$ IS EQUIVALENT TO ONE STATOR BLADE PITCH (32 BLADES). PATTERNS REPEAT AROUND COMPLETE ANNULUS.
- C) FLOW RATE: $\frac{\dot{Q}}{Q_0} = 0.430$

FIG. 54 TOTAL PRESSURE CONTOURS DOWNSTREAM OF ROTOR



NOTES:

- A) CONTOURS ARE LINES OF $\psi' = \text{CONSTANT}$ WHERE $\psi' = \frac{P_1 - P_2}{\frac{1}{2} \rho u_1^2}$
- B) THE ANGLE 11.4° IS EQUIVALENT TO ONE STATOR BLADE PITCH (32 BLADES). PATTERNS REPEAT AROUND COMPLETE ANNULUS.
- C) FLOW RATE: $\dot{Q}_0 = 0.430$

FIG. 55 TOTAL PRESSURE CONTOURS DOWNSTREAM OF STATOR

APPENDIX I
REPORT NOTATION

<u>SYMBOL</u>	<u>DEFINITION</u>
c	Absolute velocity (in a fixed coordinate system)
c_a	Absolute axial velocity component
c_u	Absolute tangential velocity component
w	Velocity relative to a rotating coordinate system
u_o	Tip velocity
ω	Angular velocity
ϕ	Dimensionless axial velocity = c_a/u_o
$\bar{\phi}$	Dimensionless axial velocity (averaged over a particular radius)
$\bar{\bar{\phi}}$	Dimensionless axial velocity (averaged over the entire annular section)
$\bar{\psi}$	Power Coefficient (or Work Coefficient)
ψ'	Local total pressure coefficient = $\frac{P - P_o}{\frac{1}{2}\rho u_o^2}$
p	Static pressure
Δ	Change of quantity
P_t	Total (stagnation) pressure
λ	Dimensionless tangential velocity = c_u/u_o
μ	Fluid absolute viscosity
ν	Fluid kinematic viscosity
ρ	Fluid density
R,r	Radius from center of rotation
R_o	Tip radius
f	Dimensionless radius = r/R_o
β	Direction of relative velocity from plane of rotation
γ	Direction of absolute velocity from plane of rotation

ζ	Total head defect or Loss coefficient
α	Angle of attack to chord line
i^*	Air incidence angle
δ^*	Boundary layer displacement thickness
Θ	Boundary layer momentum thickness
H	Boundary layer shape parameter
T	Absolute temperature
k	Recovery factor
c_p	Specific heat
T_t	Total temperature
Re	Reynold's number
c	Airfoil chord length
s	Cascade pitch

REFERENCES

1. Bowen, J. T., Sabersky, R. H., and Rannie, W. D., Theoretical and Experimental Investigations of Axial Flow Compressors, Report on Research Conducted under Contract with the Office of Naval Research, California Institute of Technology, Pasadena (January, 1949).
2. Bowen, J. T., Sabersky, R. H., and Rannie, W. D., Theoretical and Experimental Investigations of Axial Flow Compressors, Report on Research Conducted under Contract with the Office of Naval Research, California Institute of Technology, Pasadena (July, 1949).
3. Bailey, W., and Jefferson, J. L., Compressibility Effects on Cascades of Low Cambered Compressor Blades, R. A. E. Report No. E 3972, Royal Aircraft Establishment, Farnborough (May, 1943).
4. Moffatt, M., Markowski, S. J., and Dunnells, N. A., Report on Cylindrical Temperature Probes, Pratt and Whitney Aircraft, East Hartford, Connecticut (May, 1945).
5. Strong, J., Procedures in Experimental Physics, Prentice-Hall, Inc., New York, 1948.
6. Carter, A. D. S., Three-Dimensional-Flow Theories for Axial Compressors and Turbines, Internal Combustion Turbines, War Emergency Issue No. 41 of the Institution of Mechanical Engineers, Reprint by the ASME, April 1949.
7. Eckert, B., A Temperature Measuring Device for the Exact Determination of the Internal Adiabatic Efficiency of a Compressor, Vol. 2, Buships 338, May 1946, Navy Department, Washington 25, D. C.